Production Cavity and Central Optics for a Light Shining through a Wall Experiment

Dissertation

zur Erlangung des Doktorgrades
des Department Physik
der Universität Hamburg

vorgelegt von

Reza Hodajerdi

aus Teheran

Hamburg
2014

Gutachter der Dissertation: Prof. Dr. Dieter Horns
Apl. Prof. Dr. Benno Willke

Gutachter der Disputation: Prof. Dr. Dieter Horns
Dr. Axel Lindner

Datum der Disputation: 26. Januar 2015

Vorsitzender des Prüfungsausschusses: Dr. Georg Steinbrück

Vorsitzender des Promotionsausschusses: Prof. Dr. Jan Louis

Leiter des Departments Physik: Prof. Dr. Peter Hauschildt

Dekan der Fakultät für Mathematik,
Informatik und Naturwissenschaften: Prof. Dr. Heinrich Graener

Abstract

The unexplained nature of dark matter and dark energy is a prominent reason for investigating physics beyond the standard model of particle physics (SM). Some extensions of the SM propose weakly interacting slim particles (WISPs). In an attempt to prove the existence of these particles, Light shining through the wall (LSW) experiments explore a very weak coupling between WISPs and photons (and vice versa). LSW experiments employ high-power lasers that provide a well defined flux of photons for the WISP-Photon conversion.

The ALPS-I experiment at DESY in Hamburg was the first successful experiment with a high finesse optical resonator to enhance the laser power in a strong magnetic field in order to increase the photon to WISP conversion probability. The ALPS-II experimental concept adds a second optical cavity to also increase the reconversion probability. Both cavities are separated by a wall, amplify light at 1064 nm and share a common optical axis. Operating these two cavities inside 20 straightened HERA superconducting dipole magnets and using a transition edge sensor (TES) as a single photon detector will make the ALPS-II experiment almost three orders of magnitude more sensitive than its predecessor.

Since photons, originating from reconverted WISPs in the regeneration cavity (RC) have 1064 nm wavelengths, the RC has to be locked to the production cavity (PC) with light of a different wavelength. Therefore frequency doubled PCs light will be used to lock the RC. This 532 nm light shall not arrive at the TES to prevent background noise. To achieve this, an optical attenuation system for wavelengths different from 1064 nm is required.

In my thesis, the required attenuation was estimated and an optical setup was proposed and constructed and tested. It attenuates green photons by a factor of of 10^{-18} and transmits 85% of the infrared photons. Furthermore the high finesse production cavity of ALPS-IIa was set up and characterized during this thesis. The PC reached a finesse of $\mathcal{F} \approx 1600$, which is approximately a factor of five lower than the design value due to additional unknown losses. Nevertheless it was robustly locked for more than two hours. The stabilized cavity was used to gain important knowledge about the limiting factors and the environmental conditions in the new laboratories regarding vibrational noises.

These achievements are two cornerstones of the ALPS-IIa phase. Once all stages are combined it will proof that the general concept of ALPS-II works properly. A successful ALPS-II experiment yields new insights into the composition of the universe and is able to discover particles beyond the standard model of particle physics.

Zusammenfassung

Die nicht erklärte Natur dunkler Materie und dunkler Energie ist ein Hauptgrund für die Suche nach physikalischen Effekten jenseits des Standardmodells der Teilchenphysik (SM). Einige Erweiterungen des SM postulieren schwach wechselwirkende, leichte Teilchen (WISPs). Licht durch die Wand (LSW) Experimente nutzen die sehr schwache Kopplung zwischen WISPs und Photonen (und umgekehrt) um nach WISPs zu suchen. LSW Experimenten, nutzen leistungsstarke Laser welche einen genau definierten Strahl von Photonen als Quelle für die WISP-Photon Konversion benutzen.

Das ALPS-I Experiment am DESY in Hamburg war das erste erfolgreiche Experiment, das die Kombination aus einem optischen Resonator hoher finesse, um die Laserleistung zu erhöhen und einem starken Magnetfeld nutzte, um die Konversionswahrscheinlichkeit von Photonen zu WISPs zu erhöhen. ALPS-II benutzt einen zweiten Resonator, um auch die Wahrscheinlichkeit der Rückkonversions zu erhöhen. Beide Resonatoren sind durch eine Wand getrennt, verstärken Licht mit 1064 nm Wellenlänge und besitzen eine gemeinsame optische Achse. Der Einsatz dieser beiden Resonatoren innerhalb 20 gerade gebogener HERA Magneten und der Einsatz eines supraleitenden Übergangs-Mikrokalorimeters (TES) als Einzel-Photon-Detektor machen ALPS-II drei Größenordnungen sensitiver als dessen Vorgänger.

Da die aus WISPs rückkonvertierten Photonen, welche im Regenartionsresonator (RC) entstanden sind, eine Wellenlänge von 1064 nm haben, ist es wichtig, das der RC mit einer anderen Wellenlänge auf den Produktionsresonator (PC) stabilisiert wird. Deshalb wird das frequenzverdoppelte Licht aus dem PC zur Stabilisierung des RCs verwendet. Dieses 532 nm Licht soll daran gehindert werden den TES zu erreichen um ein Untergrundrauschen zu verhindern. Um dies zu erreichen wird ein Abschwächungsaufbau für Wellenlängen, die nicht 1064 nm betragen, benötigt.

Im Rahmen meiner Arbeit wurde die notwendige Abschwächung berechnet. Ein optischer Aufbau wurde vorgeschlagen und konstruiert und getestet. Dieser Aufbau kann den grünen Strahl um einen Faktor 10^{-18} abschwächen während 85% der infraroten Photonen transmittiert werden. Weiterhin wurde der ALPS-IIa PC ebenfalls in Rahmen dieser Arbeit realisiert. Dieser Resonator hat eine finesse von $\mathcal{F} \approx 1600$ was aufgrund zusätzliche unbekannte Verluste um den Faktor fünf niedriger is als der Designwert. Nicht desto trotz konnte der Resonator länger als zwei Stunden stabil betrieben werden. Der stabilisierte Resonator konnte wichtige Daten bezüglich der Rahmenbedingungen in den neuen Laboren, besonders im Hinblick auf Vibrationsrauschen, sammeln.

Diese Errungenschaften sind zwei Eckpfeiler der ALPS-IIa Phase. Die erfolgreiche Kombination dieser Schritte wird das Konzept von ALPS-II bestätigen. Ein erfolgreiches ALPS-II Experiment ermöglicht neue Einblicke über die Zusammenstellung des Universums und ist fähig Teilchen jenseits des Standardmodells der Teilchenphysik zu entdecken.

CONTENTS

CHAPTER 1

Introduction

During the last century, several observations and theories revolutionized our understanding of the world we are living in. The standard model of particle physics and the theory of general relativity are two cornerstones of our view of the universe. Albert Einstein's theory of general relativity from 1916 changed our understanding of space and time. Inspired by his theory and based on the observed cosmological redshift, Georges Lemaître proposed the expansion of the universe in 1927. Two years later Edwin Hubble measured an empirical law connecting the distance of a galaxy and the measured redshift from this galaxy with the expansion rate of the universe. Later, this relation was named after him. The standard model of cosmology is based on these observations. The discovery of cosmic rays by Victor Hess in 1925 allowed for deeper insights into the cohesions of our world and led to the development of the standard model (SM) of particle physics. Although the validity of all these models is confirmed by observations, detailed experiments were and are still necessary to research the implications of these theories.

The SM is currently the most successful description of the composition of the known matter in universe and their interactions (excluding gravity). It predicts a number of particles, which first had to be discovered experimentally to confirm the theory. The theory of general relativity was confirmed, amongst others things, by indirectly observing gravitational waves, which represent a spacetime disturbance. However, direct detection of gravitational waves is still a matter of ongoing research.

The invention of the laser in 1960 can be seen as a milestone of modern experimental physics. The source of coherent photons opens the door for a broad field of physical experiments. It allows for a number of measurements with unprecedented accuracy. In the near future this allows to measure relative length changes on the order of 10^{-22} caused by gravitational waves passing the earth. For measurements with such a precession, ultra stable cavities and high power laser systems are required.

The technical progress in the field of experimental particle physics is also remarkable. Modern particle accelerators achieve energies in the TeV regime and allowed for the discovery of all particles that the SM predicts, culminating in the discovery of a Higgs particle at the Large Hadron Collider (LHC). These impressive confirmations of the SM cannot outshine its shortcomings. It was never designed to explain gravity and therefore can not be the ultimate description of the universe. Unfortunately it also cannot explain the existence of dark matter and dark energy which are essential components of the standard model of cosmology.

There are extensions to the SM proposed, that include these missing components. The extensions arise for example from string theories or theories of supersymmetry. Some of these extensions predict a number of very light particles which are very weakly interacting with other SM particles, called weakly interacting slim particle (WISP)s. There are several astrophysical phenomena that are currently not fully understood and could be explained by the existence of WISPs. The search for WISPs uses the assumption that a very small coupling of these hypothetical particles to the particles of the SM, like photons, exists. This assumption is incorporated into the concept of light-shining-through a wall (LSW) experiments which search for WISPs, that are converted from a photon, which can penetrate a wall that is opaque for photons and then reconverts behind the wall to a photon which can be detected. However, the production probability of a WISP from the photon is very small due to its weak coupling constant to the SM particle. Therefore high intensity sources are required to produce a large amount of photons, which can convert to WISPs. Optical resonators can be utilized to buildup and store the incoupled light internally. The LSW experiment ALPS-I used such a resonator for a first search of WISPs at Deutsches Elektronen Synchrotron (DESY). The realization of this cavity was achieved by using the experience gained by the development of large scale gravitational wave detectors like GEO600 and LIGO.

Decades after proposing both gravitational waves and the SM, it was possible to use the know-how gained by the search for the former, to aid research of the latter.

Based on the successful run of ALPS-I, the ALPS-II experiment is currently prepared. ALPS-II will use a high power laser beam in a high finesse cavity, combined with a high magnetic field as the production source for WISPs. A second cavity behind the wall, combined with another high magnetic field, will increase the probability of the regeneration of WISPs to photons. Combining these two high finesse cavities in a very long and strong magnetic field with a sensitive single photon detector incorporating a low dark-count rate, allows ALPS-II to reach unprecedented sensitivities. In the scope of this thesis the production cavity of the ALPS-II experiment was developed. In addition an optical setup was proposed, realized and successfully tested which is needed to protect the single photon detector from disturbing light, which would otherwise impair its sensitivity. The successful implementation of these components helps paving the way for an LSW experiment which is three orders of magnitude more sensitive than its predecessor. The ALPS-II experiment will be one of the most promising approaches for studying low energy physics beyond the SM.The structure of this thesis is as follows:

- Chapter 2 gives a brief overview about the shortcomings of the SM. The most important observations and phenomena which can be explained by the existence of WISPs will be introduced. It will discuss different possibilities for the experimental searches for WISPs. Then all stages of the LSW experiment ALPS-II will be introduced. At last, the sensitivity of the new experiment will be discussed.

- Chapter 3 deals with the theoretical description of Fabry-Perot resonators. After a brief overview of geometrical optics and Gaussian beams, it will discuss several types of optical resonators and their stability. In addition to that, resonator properties and different types of resonator-couplings are described. The last part describes the realization of a Pound-Drever-Hall lock as an active method of stabilizing a cavity.

- Chapter 4 gives a detailed description of the first part the ALPS-II experiment from an optical point of view. The geometrical design of the experiment will be specified. Then the goals of ALPS-II according to the optical parameters are discussed and the optical concept will be elucidated. In the second part, the ALPS-IIa experiment, as the first stage of the project, will be treated. The production cavity, set up in the course of this thesis, will be examined. The properties of this cavity and its performance will be discussed. It follows the characterization of the cavity and measurements regarding the vibrational noise of the environment. A conclusion about the gained knowledge and suggestions for the next steps in ALPS-IIa ends this chapter.

- Chapter 5 describes the second experimental part of this thesis: It motivates the necessity to build an attenuation system for ensuring that the background count rate of the detection system is sufficiently reduced. First it will give a short overview of different sources for disturbing light. An estimation of the needed attenuation will follow. After this, several test setups are introduced and a measurement setup including the results, regarding the attenuation levels is described. This chapter closes with a conclusion about the achieved attenuation and suggestions for the next steps regarding the ALPS-IIa experiment.

- Chapter 6 summarizes the achievements of this thesis, related to the conclusions of the previous chapters. It specifies the challenges of the experiment and makes suggestions to ensure a prosper future for the ALPS-IIa experiment.

Chapter 2

ALPS-II search for fundamental particles

After the successful completion of the ALPS-I experiment [1, 2] as the worlds most sensitive laboratory experiment at its time aiming at finding WISP and the successful implementation of an optical resonator for this search [3], the ALPS-II experiment is the next logical step on the path to increase the sensitivity of experiments in this field of particle physics.

In this chapter we give an overview of the physical considerations which make experiments like ours interesting. We will describe the hypothetical particles that ALPS-II is searching for. Thereafter we will introduce possible experimental setups for finding WISPs including LSW experiments, an experiment category to which both ALPS-I and ALPS-II belong. As last item we will describe the sensitivity of the ALPS-II experiment and give an overview over the several stages of the new experiment. We will also compare the sensitivity of ALPS-II with its successful predecessor.

2.1 The Standard Model and its extension through WISPs

There are four fundamental forces which are so far accountable for all observed physical processes in nature. These four forces are:

- The electromagnetic force accounts for phenomena like the existence of light, magnetism, chemical bonds of molecules and the formation of atoms. It is an infinitely ranged force.
- The gravitational force is the weakest of the four also with an infinite range like the electromagnetic force. This force accounts for the attraction between two masses and is the only force which only acts attractive.
- Weak interaction with which e.g. some form of the radioactive decay of matter can be explained.
- Strong interaction which is very short ranged and accounts for the stability of nucleons.

The SM of particle physics which is reviewed e.g. in [4] is a theory that incorporates three of these interactions. It describes the weak and the strong nuclear forces as well as the electromagnetic force as an exchange of bosonic particles and thereby the interactions of all known types of particles in the universe. The predictions of the SM have proven to be successful with numerous experiments. The latest and most prominent proof was the discovery of a Higgs-boson which was announced last year by two collaborations of the LHC at the Conseil Européen pour la Recherche Nulcléaire (CERN) [5, 6].

Nevertheless there are astronomical and cosmological phenomena for which the SM in its current state does not give an explanation. Within the SM, the so called strong CP problem exists and is so far an unsolved one. In the following section we will describe this drawback of the SM and also describe the astronomical phenomena that demand for extensions of the SM. One part of these necessary extensions of the SM could be the introduction of a new family of particles which have not been experimentally found yet but which could solve and explain the observed phenomena. This particle-family is called weakly interacting slim particles or WISPs.

2.1.1 Strong CP problem

The CP-symmetry implies that a physical process is invariant under the simultaneous conversion of a particle into its antiparticle (C̲harge conjugation) and inversion of the spatial coordinates (P̲arity inversion). In the framework of the SM, the strong and weak interactions are allowed to violate this symmetry.

A CP-violation has been observed for the weak interaction [7, 8]. However, there is no experimental evidence for the strong nuclear interaction also violating this symmetry, although quantum chromo dynamics (QCD), the theory of the strong nuclear interaction, includes a term $\bar{\theta}$ that allows for a CP-violation. This term is the sum of a vacuum angle θ and the quark mass matrix. These contributions are unrelated to each other and not necessarily small. Recent very precise measurements shown a limit of $|\bar{\theta}| \leq 10^{-10}$. It is somehow challenging to theoretically explain why this parameter has to be of such a precise value in order for the theory to agree with observations. This fine tuning of the vacuum angle $\bar{\theta}$ is known as the strong CP problem.

To solve this dilemma, Robert Peccei and Helen Quinn proposed an additional symmetry to extend the SM. The Peccei-Quinn (PQ) symmetry [9] is broken spontaneously at low energies [10]. The PQ symmetry postulates that the angle θ is not a fixed number but a dynamic value. The consequences of breaking this symmetry is a so called pseudo-Nambu-Goldstone boson. This very light particle can "clean" the strong nuclear force off the CP-problem. Hence Frank Wilczek named it after a detergent, the axion [11], or the QCD axion because its existence is motivated by the theory of strong nuclear interactions.

QCD axion

Due to the interaction between the QCD axion and gluons[1], the axion experiences an effective potential and thus possesses an effective non-zero mass [12]

$$m_a \approx \frac{m_\pi f_\pi}{f_a} \approx \mathrm{me\,V} \times \left(\frac{10^{10}\mathrm{GeV}}{f_a} \right) \qquad , \tag{2.1}$$

where m_π and f_π are the mass respectively the decay constant of a pion and f_a is the axion decay constant. The decay constant f_a sets the energy scale at which the PQ symmetry is broken. The effective coupling of axion to another particle of the SM (quarks and for us most important, photons) is inversely proportional to its decay constant [13]. The coupling strength between axion and photon scales as

$$g_{a\gamma} \propto \frac{1}{f_a} \propto m_a \qquad . \tag{2.2}$$

The QCD axion is the oldest and most prominent example of WISPs. The coupling between an axion and a photon results in the Primakoff effect, which is shown in figure 2.1: A photon converts into an axion by interacting with an external electric or magnetic field and vice versa.

---

[1] The Lagrangian which explains this phenomenon is being described e.g in [12].

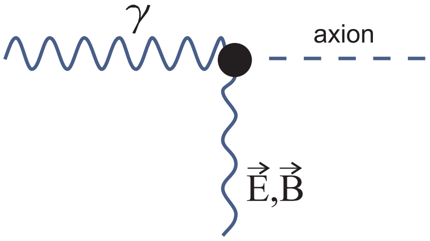

Figure 2.1: The photon-axion conversion in an external field. This so called Primakoff effect forms the basis of our experiment.

This effect leads to a photon-axion oscillation in presence of an external magnetic field and is the basic idea to tackle the production of axion-like particle (ALP)s experimentally. ALPs are hypothetical particles which couple to the electromagnetic field in the same way as axions. However, they don't obey the same relationship between mass and coupling constant. If the propagation direction of the photons and the external magnetic field are perpendicular to each other, the probability of the conversion between these two is given by [14]

$$\mathcal{P}_{\gamma\to a} = \frac{\omega}{4k_a}\left(g_{a\gamma}BL\right)^2 |F|^2 = \mathcal{P}_{a\to\gamma} \qquad \text{with} \qquad k_a^2 = \omega^2 - m_a^2 \qquad . \tag{2.3}$$

Employing natural units ($\hbar = c = 1$), ω is the photon energy, B the magnetic field strength, L the distance that the photons are traveling through this field, k_a the wave number of the axion-like particle and F a form factor with

$$|F| = \frac{2}{qL}\sin\left(\frac{qL}{2}\right) \leq 1 \qquad \text{with} \qquad q = n\omega - \sqrt{\omega^2 - m_a^2} \qquad ,$$

where q is the momentum transfer to the magnetic field and n the refractive index of the medium in which the photons are propagating.

As mentioned before, this conversion mechanism between the QCD axion and photons can be generalized for any another ALP. However, the QCD axion is constrained by its mass-coupling described by equation (2.2). ALPs are not limited by this and can be assumed to exist in a wider parameter space than the QCD axion.

2.1.2 Other WISP candidates

Beyond the proposal of axions, there are theories discussing other possible WISPs. Hidden photons are one of these candidates. Hidden photons arise e.g. from the extensions of the standard model which are motivated by string theory [15]. A hidden photon is the massive partner of the photon with spin 1 and thus can be produced from ordinary photons without the need for an external magnetic field. The process of oscillation between ordinary photons and hidden photons is like the oscillation between photons and ALPs (except for the magnetic field) and is called kinetic mixing [16]. As will be shown in the next section, the plan for the first two steps of ALPS-II do not include a magnetic field, therefore it is only possible to search for hidden photons.

There are also theories for other WISP candidates like mini-charged particles (MCP) [17] and chameleons [18] which are not in the focus of ALPS-II, the former is better probed in other LSW configurations [19]. Phenomena in cosmology and astrophysics are the main motivation for ALPs as WISP candidates. These phenomena also set constrains for different ALP types. In the following section, prominent examples are named. For a detailed overview we refer to [20] and [21].

2.1.3 Dark matter and dark energy

A good possibility to gain information about the structure of the universe and its composition is a measurement of the cosmic microwave background (CMB) of the universe. The CMB can be understood as the remaining light from the big bang [22]. Because of the expansion of the universe and the stretching of the space time, the wavelength of the CMB photons is also stretched and thus there is a corresponding red shift of the light. This spectrum has a perfect black body shape [23] which is nearly fully isotropic. Measurements of the spatial anisotropy of the CMB [24] revealed that $\approx$5% of the universe is consisting of ordinary matter. Around 27% of the universe is made out of the so called ”dark matter” which is a type of matter with still not understood properties. The remaining and also biggest part of the universe consists of the so called ”dark energy” [25]. The experimental evidence of dark matter comes from astrophysical and cosmological observations which have shown two properties of dark matter: First, it interacts with the environment gravitationally and second there is no sizable interacting between dark matter and the environment through electromagnetic or strong forces. The former explains that dark matter is not made up of atoms and the latter explains the observed transparency of dark matter [12]. The most important indication for dark energy is the accelerated expansion of the universe [26]. There are two types of dark matter assumed:

- Hot dark matter consists of particles traveling at nearly the speed of light. Because of its high velocities, they form very hot gases [27].
- Cold dark matter moves much slower than hot dark matter and forms much colder gases [28].

ALPs or hidden photons could have been produced in the early universe and survived until today as cold dark matter. A part of the large parameter space defined by the photon coupling and the mass, both ALPs and hidden photons are candidates for a component of cold dark mater [21].

2.1.4 Astrophysical observations

There are also astrophysical observations that motivate physics beyond the standard model. From the observed energy loss of stellar objects, one can search for additional cooling possibilities beyond the interactions explainable within the SM. WISPs could be involved in such cooling processes. As they are very weakly interacting with the SM matter, they could be produced in the core of stars and pass towards the outer stellar region without interacting with matter [29]. The observed phenomena can be used to set constrains for the mass and coupling of ALPs. For example, the non-observation of γ-rays during the supernova 1987A [30] sets a constrain on the parameter space of the ALPs (for details see Figure 2.2) [31]. The lifetime of horizontal branch stars also sets a bound on ALP masses which is shown in Figure 2.2 [32]. WISPs with defined coupling factor $g_{a\gamma}$ as additional cooling channel could explain a deviation of the expected ratio between horizontal branch stars and red giant stars in globular clusters [33]. Another popular motivation is the discrepancy between the luminosity of white dwarfs and the models describing them [34]. An additional cooling channel via ALPs could explain this discrepancy. Another motivation for the existence of ALPs is the large number of observed γ-rays from extragalactic sources, which should be attenuated due to interaction with the extragalactic background light. The γ-rays could be able to avoid this interaction by oscillating to a weakly interacting ALP and reconvert back to a photon in the earth or milky ways magnetic field [35]. Figure 2.2 gives an overview of the suspected parameter space of several WISPs and theirs coupling to photons based on astrophysical observations. The parameter space of the QCD axion is also marked. The sensitivity of the ALPS-II experiment is explained in section 2.3.

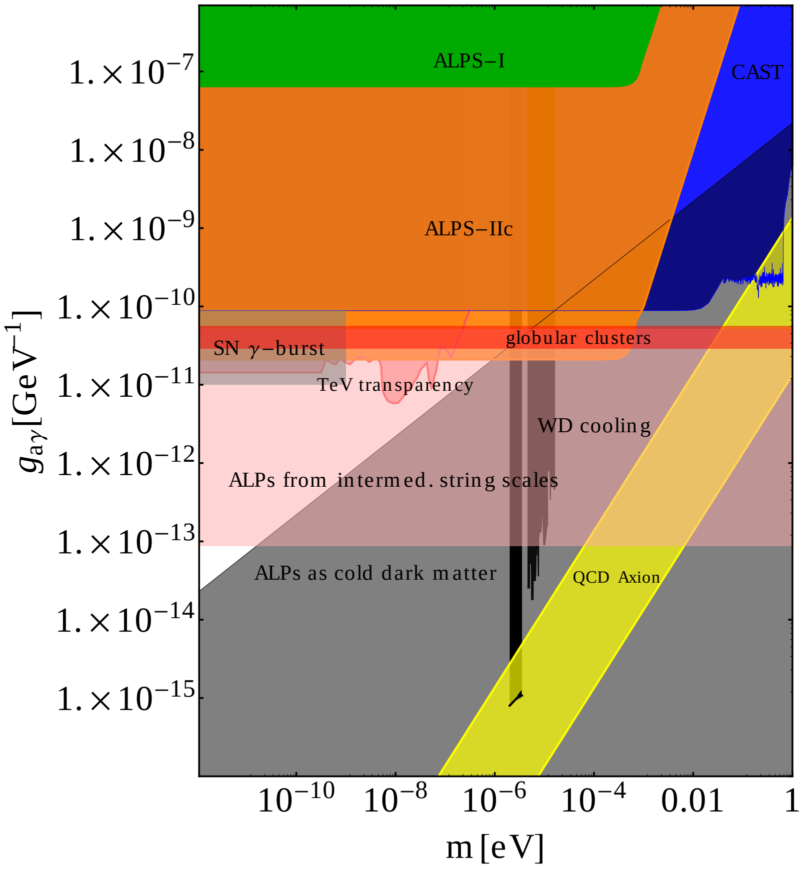

Figure 2.2: The sensitivity range of ALPS-IIc (orange) compared to the experimental constrains of its predecessor ALPS-I (green), the Helioscope experiment CAST (Blue) and several Haloscope experiments (Black). The constrains from the astrophysical observations and experimental hints are marked and explained below. Picture provided by [36].

2.2 Experimental searches for WISPs

The experimental search for WISPs through their coupling with photons based on [37] can be divided in three categories which will be shortly mentioned here.

Helioscopes

Helioscopes are telescopes used for direct observations of the sun. Combining closed helioscopes with strong magnets can be used for the WISP search. The magnetic field is aligned perpendicular to the direction of the telescope. WISPs, possibly produced in the sun, can surpass the enclosure of the telescope which can reconvert to a photon in the magnetic field inside the telescope and be detected. These WISPs could be an additional cooling channel for the sun. The CERN Axion Solar Telescope (CAST) [38] is such a helioscope. With the International Axion Observatory (IAXO) [39] the next generation of Helioscopes is under development.

Haloscopes

Haloscopes are microwave cavities surrounded by a strong static magnetic field [37]. They search for cold dark matter axions from the dark matter halo. If there are axions included in the Milky Way halo, they could reconvert to photons inside the microwave cavity[2] and subsequently be detected by a microwave receiver. Due to tuning requirements of the microwave frequency and axion energy the search with haloscopes is limited to a small mass-range of axions m_a therefore, for a small coupling constant range. A prominent haloscope experiment is the Axion Dark Matter Experiment (ADMX) at the University of Washington, Seattle [40].

Light-shining-through-a-wall (LSW)

The main difference between LSW experiments and the two types of experiments mentioned before is the source of the photons. While Helioscopes use the sun as the WISP source and haloscopes search for reconverted ALPs, the LSW experiments provide their own photon source. This has the huge benefit that the source is accurately defined and that the photon numbers provided by the source are known. This full control of all experimental parameters simplifies the interpretation of the results of the experiment. An LSW experiment can be divided into two areas that are separated by a ”wall”, which is opaque for photons.Both areas are situated within a strong magnetic field. In front of the wall, ordinary photons are propagating which are provided by a laser source. These photons convert to a WISP due to the interaction with the magnetic field. The WISP can then pass through the wall since it only interacts very weakly with SM particles. To be detected, the WISP has to reconvert to a photon after traversing the wall. This is possible by interacting with the magnetic field behind the wall. This process is illustrated in Figure 2.3. Due to the two necessary conversions the detected photon rate is given by

$$\dot{N}_{det} = \eta \cdot \mathcal{P}_{\gamma \to a} \cdot \mathcal{P}_{a \to \gamma} \cdot \dot{N}_{Pr} \qquad , \tag{2.4}$$

---

[2] If the resonance frequency of the cavity equals the axion energy

where η is the efficiency of the experiment, $\mathcal{P}_i$s are the probabilities of photon to ALP and ALP to photon conversions and $\dot{N}_{Pr}$ is the rate of photons being produced by the laser.

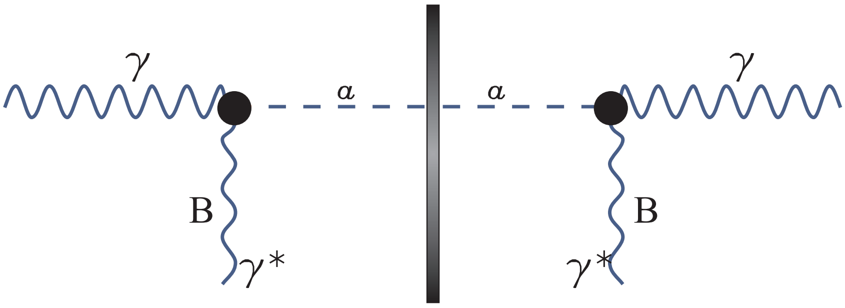

Figure 2.3: The working principle of an LSW experiment. A twofold occurrence of Primakoff effects, in front and behind of the opaque wall, causes that only WISPs converted from the photon field pass through the wall. Behind the wall these WISPs can reconvert to detectable photons due to the interaction with the magnetic field. The reconverted photons have the same properties as the photons in front of the wall.

Detecting a photon behind the wall, provided that the wall is really opaque and there is no other possibility for the photon to traverse the wall, is an important evidence for the existence of WISPs There are different LSW experiments realized today [41, 42]. The predecessor of our experiment, the ALPS-I experiment [1, 2], reached the highest sensitivity of all LSW experiments at its time. ALPS-II will increase this sensitivity by three orders of magnitude [43]. In the next section we will describe the ALPS-II experiment in detail.

2.3 General description of the ALPS-II experiment

ALPS-II is the second LSW experiment at the DESY and is the successor of ALPS-I. To increase the sensitivity of ALPS-II compared to its predecessor it is planned to improve basically all three important factors contributing to an LSW experiment: The photon number, the interaction length of photons and magnetic field and the efficiency of the detector. The sensitivity of a LSW experiment is given by the probability of the conversion and reconversion of a photon to a WISP which depends on the coupling factor $g_{a\gamma}$ and the sensitivity of the photon detector. To estimate the sensitivity we combine these two factors by using Equations (2.4) and (2.3) and arrive at the sensitivity factor S [44, 45]

$$S(g_{a\gamma}) \propto \frac{1}{BL}\left(\frac{DC}{T}\right)^{1/8} \cdot \left(\frac{1}{\eta \dot{N}_{Pr}\, PB_{PC}\, PB_{RC}}\right)^{1/4} \quad , \tag{2.5}$$

where $g_{a\gamma}$ is the coupling strength between the axion and the photon, B magnetic field, L the interaction length, DC the dark count rate of the detector and η its efficiency, T the duration of the measurement, $\dot{N}_{Pr}$ rate of photons generated by the laser source and PB_{PC} is the power buildup factor of the production cavity and PB_{RC} is the power buildup factor for the regeneration cavity that will be explained below. The goal of all improvements is to increase the sensitivity by lowering the value of $S(g_{a\gamma})$. As it can be seen from Equation (2.5), increasing the magnetic field or the interaction length of the magnetic field increases the sensitivity linearly. All other factors scale only with the fourth root, which leads to the conclusion that raising the magnetic field strength and interaction length is of the utmost importance. It is planed to use the superconducting dipole magnets of the decommissioned Hadron-Electron Ring Accelerator (HERA) to reach these goals, like it was done in ALPS-I, but with more magnets than before. A longer measurement time also increases the sensitivity but it scales with the eighth root. The planned improvements of ALPS-II are:

- **Optical system:** The Production Cavity (PC) which was also an important part of ALPS-I [2] is meant to enhance the photon numbers from the laser source. In contrast to the ALPS-I cavity with a circulating power of 1 kW the ALPS-II PC will be a high finesse cavity with a circulating power of 150 kW. The construction of this cavity was part of this thesis and will be discussed in chapter 4. Additionally, a second resonator is planned in the regeneration area. This regeneration cavity (RC) enhances the reconversion probability of WISPs to photons. The operating wavelength of the experiment changes from 532 nm in ALPS-I to 1064 nm in ALPS-II. The reason for this change is the higher damage threshold of the mirror coatings for infrared photons (E_{1064}=1,16 eV). The cavity mirrors of the ALPS-I experiment could stand the high power circulating of 532 nm photons ($E_{532} = 2,33\,\text{eV}$) only for about a few ten hours.

- **Magnetic interaction length:** The sensitivity factor scales with the magnetic field B and its interaction length L, and therefore provides the most efficient improvement of the sensitivity. We plan to use twenty straightened superconducting HERA dipole magnets, ten for the production area and ten for the regeneration area which gives 100 m of magnetic length for each cavity. The straightening of these dipole magnets is necessary since they were formerly used in a ring accelerator and ten of them in a row don't offer 100 m of straight tube for a laser beam to pass through and building of a cavity with the envisaged power enhancement due to clipping. The needed minimum of free aperture will be discussed in section 4.1.1. Also the straightening of these magnets is not trivial. However it was possible to straighten one of these with a field strength of >5 T, measured after straightening. At the moment, a second magnet is in the process of being straightened [46].

- **Detector system:** For the detection of regenerated photons from a possible WISP field, we need a low dark count rate and also a high quantum efficiency of the detector for the infrared photons. In chapter 5 we will discuss the requirements imposed on the detection system in more detail. The ALPS-I experiment used a Si-CCD camera as detector with a quantum efficiency (QE) of ≈95% and a dark count rate of $1 \cdot 10^{-3} \frac{\mathrm{ph}}{\mathrm{s}}$. However, this detector can not be used for ALPS-II because of its very low QE for infrared photons of (≈ 1.2%) [47]. For ALPS-II it is planned to use a transition edge sensor (TES) as detector [3]. The TES has an intrinsic dark count rate of $1 \cdot 10^{-4} \frac{\mathrm{ph}}{\mathrm{s}}$ and a measured detection efficiency (DE) of ≈ 23% for infrared photons [29].

These improvements enhance the sensitivity of ALPS-IIc[4] in searching for ALPs by more than three orders of magnitude compared to ALPS-I. In table 2.1 the above mentioned changes between the two experiments are shown. Also the scaling factor of every change and its contribution to the overall sensitivity gain is listed. However, the calculated total improvements are different compared to [43] because of the current results of the QE and dark count rate of the TES detector. One could think that the improvements due to the new detector are marginal. Fortunately, this is not true: A high QE of over 90% of the CCD detector is only achieved for visible light which damages the mirrors at high power. Because of the new TES detector we are now able to use infrared wavelength, which is not nearly as destructive to the mirrors as the green light, and build a high power production cavity. The highest improvement arises from the use of twenty HERA magnets and the use of the RC. As mentioned in section 2.1.2, the hidden photon conversion is not depending on the factor BL. Thus the sensitivity gain for these particles increases by a factor of 60. However, due to the longer production and regeneration areas ALPS-II will be able to search also in a range of smaller masses of the hidden photons.

---

[3] This detector is explained in detail in [29]

[4] The several stages of ALPS-II are explained in the next section.

Parameter	Scaling	ALPS-I	ALPS-IIc	Sens. gain
Circulating input power P_{cir}	$g_{a\gamma} \propto P_{in}^{-1/4}$	$1\,\mathrm{kW}$	$150\,\mathrm{kW}$	3.5
Rel. photon number flux n_γ	$g_{a\gamma} \propto n_\gamma^{-1/4}$	1 (532 nm)	2 (1064 nm)	1.2
Power built up in RC PB_{RC}	$g_{a\gamma} \propto P_{reg}^{-1/4}$	1	40000	14
Detector efficiency DE	$g_{a\gamma} \propto QE^{-1/4}$	0.9	0.23	0.72
Detector noise DC	$g_{a\gamma} \propto DC^{-1/8}$	$1.8 \cdot 10^{-3}\,\frac{\mathrm{ph}}{\mathrm{s}}$	$1 \cdot 10^{-4}\,\frac{\mathrm{ph}}{\mathrm{s}}$	1.44
BL (PC and RC)	$g_{a\gamma} \propto (BL)^{-1}$	$22\,\mathrm{Tm}$	$468\,\mathrm{Tm}$	21
combined improvements				1280

Table 2.1: The improvements of ALPS-IIc compared to ALPS-I. Shown are the improvements of individual components of the experiment and their scaling for the photon axion coupling constant $g_{a\gamma}$. The table is taken from [43] with updated values for QE and DC which are taken from [29].

2.3.1 ALPS-II experimental steps

To reach the described sensitivity, there are three stages planned. The main reason for that is to minimize unforeseen risks for the experimental setup. These steps are:

- **ALPS-IIa** This step is the proof of principles and is divided into three parts. These parts are the design and test of a small model of ALPS-IIc at Albert-Einstein-Institute (AEI) in Hanover with one meter long PC and RC to test the optical design of ALPS-II. This design will be discussed in chapter 4. At the same time the production cavity of ALPS-IIa, with the length of almost 10 m, is realized in the new laboratories of the ALPS experiment at DESY and a setup for determining possible down conversion effects in the optical components used in experiment is realized. These parts are subject of this thesis and will be discussed below in more detail. The construction and first measurements with the TES is the third part of ALPS-IIa. Furthermore mechanical issues like the light-tightness of the "wall" between the production and the regeneration areas, vibration isolation of the optics from the mechanical noise of the vacuum system have to be tested in this phase. After combining all of these parts, a science run with 10 m RC and PC is planned to test the whole setup in a technical point of view. The ALPS-IIa final experiment including both cavities and the TES is from an optical point of view very similar to ALPS-IIc. Although ALPS-IIa is probably easier to align because of the shorter length of the cavities and the bigger aperture of the connection pipes between the cavity mirrors due to the missing magnets. When ALPS-IIa is completed a search for hidden photons is possible.

- **ALPS-IIb** This step is important to investigate the environment in the HERA tunnel regarding vibrations of the ground floor, available free space for optical tables and the necessary clean rooms etc.. The cavity lengths in ALPS-IIb are identical to ALPS-IIc only the magnets are not included. Thus the aperture restrictions are relaxed. However, it could be possible that we skip this step by conducting a precise risk analysis based on the results from ALPS-IIa and environmental measurements of the tunnel conditions.

- **ALPS-IIc** is the final step of the experiment where we desire to reach the full sensitivity as shown in table 2.1 with the use of the straightened magnets. In this step we have to make more efforts to align both cavities because of the small free aperture inside the magnets. The efforts are also needed because of the longer cavity lengths that leads to a smaller FWHM for the cavities (see section 3.3.4 and equation (3.33).

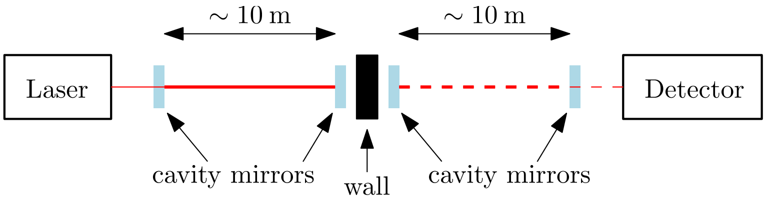

(a) ALPS-IIa

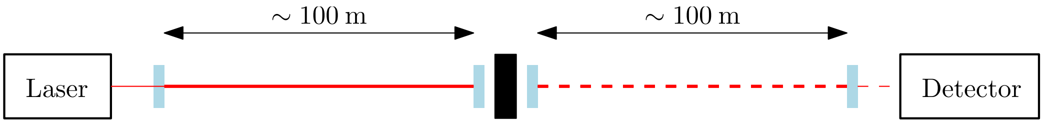

(b) ALPS-IIb

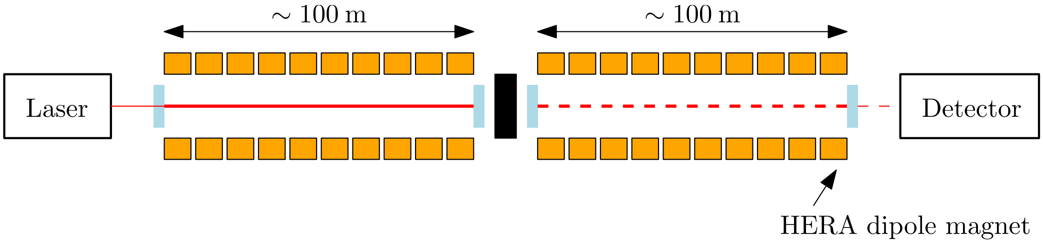

(c) ALPS-IIc

Figure 2.4: The three different phases of the ALPS-II experiment. The first two are primarily intended to demonstrate all technical requirements and a search run for hidden photons is also possible. An ALP search in the new expanded parameter space becomes possible with ALPS-IIc because of the installed HERA superconducting dipole magnets. All pictures are taken from [43].

These steps are illustrated in Figure 2.4 chronologically. The important components like both cavities, the wall, the detector and the laser are shown. The difference between ALPS-IIb and ALPS-IIc consists only of the addition of the HERA dipole magnets. The detector is shown at the end of the RC. This is only for a better illustration of the basic idea of ALPS-II. There are actually good reasons for locating the detector in the middle area of the experiment which will be explained in chapter 4. The discussed improvements and the new sensitivity of ALPS-IIc give us the possibility to search in an until now completely not investigated parameter space with a laboratory experiment. The parameters of possible ALPs and the sensitivity range of ALPS-IIc is shown in Figure 2.2.

As can be seen in Figure 2.2 it is not possible to search for the QCD axion with the ALPS-II experiment. However, this experiment will surpass the CAST experiment in the lower mass region and can ”look” for the first time in the new region for the ALPs which are cold dark matter candidates (grey area). Furthermore astrophysical observations like white dwarf cooling and the TeV transparency could be clarified with ALPS-IIc. A new favored region on the axion- photon coupling is set from the recent analyses of galactic globular clusters [33] (red area) . The two other experiments are for higher mass regions (CAST) and for a rather narrow mass region but a small coupling constant (ADMX) more sensitive than ALPS-IIc. However, one should note that these two are searching for WISPs from natural sources. In contrast, the source of ALPS-II (the laser system and the production cavity) is under our control and much more precise defined. In the next chapter we will discuss the basics of Gaussian optics and the resonator physics which are necessary to provide the ”WISP production source” for ALPS-II.

CHAPTER 3

Gaussian beams and Fabry-Perot resonators

This chapter will describe the theoretical basics which are necessary to understand this thesis. It will discus geometrical optics, Gaussian beams, the theory of the optical resonators and the frequency stabilization of a laser with the Pound-Drever-Hall method.

3.1 Geometrical optic

The concept of geometrical optics is an approximation for the theory of light propagation in which the wavelength of light goes towards zero. In geometrical optics a light source sends rays of light in every spatial direction. In homogeneous substances the beam propagates lineally. If the light beam crosses between two homogeneous substances of different refractive index, it will be, depending on the refraction indexes of both substances, refracted comply with Snell's law or according to the law of reflexion reflected on the boundary surface. If two light beams cross each others paths, they will not interact with each other. This view model of optics is called geometrical optics because it is possible to predict the beam paths without consideration of the spatial distribution of the beams. One of these methods is the ray transfer matrix analysis which will be described in following section.

3.1.1 Ray transfer matrix analysis

With the ray transfer matrix analysis it is possible to calculate the beam path in an optical system very easily. Consider an arbitrary optical system: A beam starts in point A and propagates under the angle α to the optical axis in direction of an arbitrary optical component. This beam hits the optical component in the distance x from the optical axis. The beam is now defined by these two values and can be described by the vector $\vec{p} = \begin{pmatrix} x \\ \alpha \end{pmatrix}$. The optical component is defined by n 2×2 matrix with real numbers.

$$M = \begin{pmatrix} A & B \\ C & D \end{pmatrix} \qquad .$$

The resulting ray path behind the optical component can now be calculated with:

$$\vec{p'} = M \cdot \vec{p} \qquad \text{or} \qquad \begin{pmatrix} x' \\ \alpha' \end{pmatrix} = \begin{pmatrix} A & B \\ C & D \end{pmatrix} \cdot \begin{pmatrix} x \\ \alpha \end{pmatrix} \qquad . \tag{3.1}$$

One can describe the most important optical components like lenses, mirrors, etc. with this kind of matrices. For a propagation distance S in free space the transfer matrix of a thin lens with the focal length f is given by:

$$M_S = \begin{pmatrix} 1 & S \\ 0 & 1 \end{pmatrix} \qquad \text{or} \qquad M_f = \begin{pmatrix} 1 & 0 \\ -\frac{1}{f} & 1 \end{pmatrix} \qquad .$$

It should be noted that one optical system not necessarily has only one optical component. Consider a lens system with two thin lenses. In this case is the ray transfer matrix is the result of a multiplication of five different transfer matrices: The propagation from the starting point to the first lens, the refraction by the lens, the propagation from the first lens to the second lens, the refraction by the second lens and at last the propagation to the endpoint:

$$M_g = M_{s3} M_{f2} M_{s2} M_{f1} M_{s1} \qquad . \tag{3.2}$$

The trace of the beam can be now calculated with equation (3.1).

The benefits of this analysis are on the one hand the possibility to trace a ray propagation with a limited number of multiplications and on the another hand the possibility to reduce a complicated optical system to one single matrix.

3.2 Gaussian optics

Consider the light as electromagnetic radiation so its electric and magnetic components must fulfill the Helmholtz equation to be a solution of the Maxwell equations. For electromagnetic waves of which the normal vector of the wavefront is nearly parallel to the optical axis, the paraxial approximation of the Helmholtz equation is a valid approximation. Many phenomena in optical sciences cannot be explained by the concept of geometrical optics. It is for example not possible to explain the diffraction or interference of light only with the geometrical optics. These phenomena can be explained very well by the concept of Gaussian optics, which includes also the spatial properties of light.

3.2.1 Gaussian beam

First, consider a monochromatic electromagnetic wave which can be described with a harmonic time depended wave function [48]

$$\psi(\vec{r},t) = a(\vec{r})cos[\omega t + \varphi(\vec{r})] \qquad \text{with} \qquad \omega = 2\pi\nu \qquad , \tag{3.3}$$

where ω is the angular frequency, $a(\vec{r})$ is the amplitude and $\varphi(\vec{r})$ is the phase of the electromagnetic field.

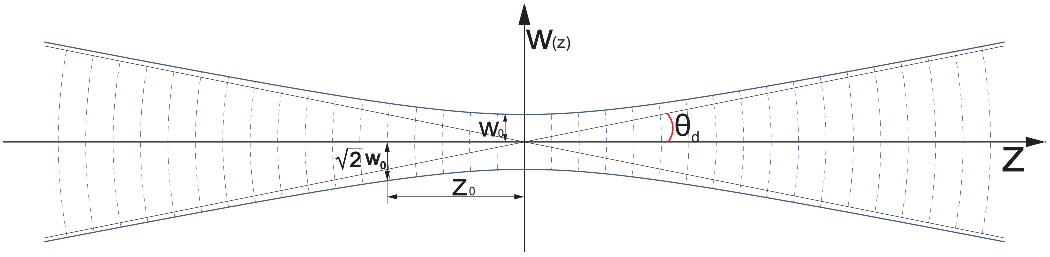

Figure 3.1: The propagation of a Gaussian beam with the beam waist w_0. Shown are also the Rayleigh length z_0 and the beam divergence Θ_d are also shown

It is easy to show that the equation (3.3) is the real part of the complex wave function

$$U(\vec{r},t) = a(\vec{r})\exp[i\varphi(\vec{r})]\exp(i\omega t) \qquad . \tag{3.4}$$

The complex wave function (3.4) can be divided into a time-dependent and a time-independent factor. The time-independent factor is:

$$U(\vec{r}) = a(\vec{r}) \exp[i\varphi(\vec{r})] \qquad .$$

This factor is called the complex amplitude [49]. The wave function $\psi(\vec{r})$ is related to the complex amplitude by

$$\psi(\vec{r}, t) = \mathrm{Re}\{U(\vec{r}) \exp(i\omega t)\} \qquad .$$

For a beam propagating in z-direction, the complex amplitude of a Gaussian beam is defined by [50]

$$\begin{gathered} U_0(\vec{r}, z) = \tfrac{w_0}{w(z)} \exp[i\zeta(z)] \cdot \exp[-ik(z + \tfrac{r^2}{2R(z)})] \cdot \exp\left(\tfrac{r^2}{w(z)^2}\right) \\ \text{with} \\ r^2 = x^2 + y^2 \qquad , \end{gathered} \tag{3.5}$$

where k is the wave number [51] and $\zeta(z)$ the Gouy phase [52, 53] of the beam, with

$$k = \frac{2\pi}{\lambda} = \frac{2\pi\nu}{c} \qquad \text{and} \qquad \zeta(z) = tan^{-1}\left(\frac{\lambda z}{\pi w_0^2}\right) \qquad .$$

Furthermore $R(z)$ is the radius of curvature of the wave front and $w(z)$ is the beam size at the position z [52], with

$$R(z) = z\left[1 + \left(\frac{z_0}{z}\right)^2\right] \qquad \text{and} \qquad w(z)^2 = w_0^2 \cdot \left(1 + \left(\frac{z}{z_0}\right)^2\right) \qquad , \tag{3.6}$$

w_0 is called beam waist and is the minimum value of $w(z)$ with

$$w_0 = \sqrt{\frac{\lambda z_0}{\pi}} \qquad . \tag{3.7}$$

Whereby z_0 is the Rayleigh range [54] which describes the distance from the waist in which the beam diameter is increased by the factor $\sqrt{2}$. Figure 3.1 shows the divergence of a Gaussian beam and the described parameter. From equation (3.6) one can see that for $z \to \infty$, w increases linearly with z so that:

$$w \approx w_0 \frac{z}{z_0} = \lambda \frac{z}{\pi w_0} \qquad , \tag{3.8}$$

Therefore in large distances ($z \gg z_0$) one can define an angle Θ_d which describes the beam divergence. In the so called far field the propagation of a Gaussian beam is again similar to a spherical wave and can be described by geometrical optics. From 3.8 one can get

$$\Theta_d = \lim_{z\to\infty} \frac{w(z)}{z} = \frac{\lambda}{\pi w_0} \qquad ,$$

A Gaussian beam is described completely by the position of its beam waist (w_0), the wavelength λ and it's Rayleigh range.

3.2.2 Intensity Distribution and Power

Intensity

We consider the optical intensity distribution $I(\vec{r})$ in x-y plane for a beam propagating in z direction. The intensity described by the equation (3.5)

$$I(r,z) = I_0 \cdot \left[\frac{w_0}{w}\right]^2 \cdot \exp\left[-\frac{2r^2}{w^2}\right] \qquad \text{with} \qquad I(r,z) = |U(\vec{r},z)|^2 \qquad , \tag{3.9}$$

where r and z are the radial and axial distance and I_0 is the intensity maximum at the beam waist w_0 [48]. The position-dependent width of the Gaussian beam is defined by the width w of the beam at the position z. On the z axis with r=0 the intensity is given by:

$$I(0,z) = I_0 \left(\frac{w_0}{w}\right)^2 \qquad ,$$

with the equation (3.8), it follows that

$$I(0,z) = \frac{I_0}{1 + (z/z_0)^2} \qquad . \tag{3.10}$$

One can see that the intensity on the beam axis with $r = 0$ has its maximum at $z = 0$ and decreases with increasing z. Equation (3.10) shows also that the intensity reaches half of its maximum at $z = \pm z_0$. At $|z| \gg z_0$ the intensity goes to

$$I(0,z) \approx I_0 \cdot \frac{z_0^2}{z^2} \qquad .$$

This means that at large distances the intensity decrease inversely proportional to the square of the distance z.

Power

The optical power of a beam propagating in z direction is the integral of its optical intensity over a transverse plane. It is independent of the propagating direction.

$$P = \int_0^\infty I(r,z) \cdot 2\pi r \, dr = \frac{I_0}{2}\left(\pi w_0^2\right) \qquad . \tag{3.11}$$

To describe a beam by its power one can re-write equation (3.9) to

$$I(r,z) = \frac{2P}{\pi w^2} \cdot \exp\left[-\frac{2r^2}{w^2}\right] \qquad . \tag{3.12}$$

Approximately 86% of the total power is located within a circle with the radius $r_0 = w$ and about 99% of it is located within a circle of radius $r_0 = \frac{\pi}{2} \cdot w$ [51].

3.2.3 Higher Order Modes

Hermitian Gaussian modes

Assume that the examined beam is not completely symmetric, but rather has a difference between the horizontal and vertical waist size. In the case of Cartesian coordinates the Hermitian Gaussian (HG) modes are a solution of the paraxial Helmholtz equation [51]:

$$\psi_{l,m}(x,y,z) = \frac{w}{w_0} \cdot H_l\left(\frac{\sqrt{2}x}{w}\right) \cdot H_m\left(\frac{\sqrt{2}y}{w}\right) \cdot U(\vec{r},z) \cdot \exp\left[i(l+m)\zeta(z)\right] \qquad . \tag{3.13}$$

H_l and H_m are the Hermite polynomials of order l and m $(l,m = 0,1,..)$ [55]. The lowest order mode by equation (3.13) is if $l = m = 0$. The Hermite polynomial zeroth order are constant and equation (3.13) is being transformed into the Gaussian beam described in equation (3.5) This solution is called $TEM_{0,0}$. TEM stands for Transverse Electric and Magnetic (TEM).

The overall radial intensity of a Gaussian mode in TEM$_{00}$, in z-direction is then given by

$$I_{00}(\vec{r}) \propto |U_{00}(r)|^2 \propto \exp\left[-2\rho^2/w(z)^2\right] \qquad .$$

It only depends on the radial coordinate r. Thus it is comprehensible that the TEM$_{00}$ corresponds to a circular spot.

Laguerre Gaussian mode

As the Hermitian Gaussian modes are the practical solutions for Cartesian coordinates, there are also other sets of solutions in different coordinate systems. The Laguerre Gaussian (LG) modes [50] for example are the convenient solutions for a cylindrical geometry. These are results from the modulation of the Gaussian beam with the Laguerre polynomials L_p^l $p, l = 0, 1, 2, ..$ [55]. The complex amplitude of the LG modes is

$$\psi_{p,l}(\vec{r}, \phi, z) = \frac{w}{w_0} \cdot L_p^l\left(\frac{2r^2}{w^2}\right) \cdot \left(\frac{\sqrt{2}r}{w}\right)^l \cdot U(\vec{r}, z) \cdot \exp\left[i(2p+l)\zeta(z)\right] \qquad . \tag{3.14}$$

Also the lowest order mode of the LG modes corresponds to a Gaussian beam described by equation (3.5).

3.2.4 Variation of the Gaussian beam

With the mentioned tools it is feasible to describe possible changes of the propagation of a Gaussian beam in its initial basis. Changes of the position of the beam waist z_0 or its size are cylindrical symmetric and thus usually expressed with LG beams. Modifications like shifting with respect to the to the optical axis or a tilting refers to axial symmetric properties and therefore can be developed with HG modes [56]:

Modifications of the beam waist

A beam with a by a factor of δw_0 bigger waist (with $\delta w_0 \ll w_0$) can be expanded by LG beams with

$$U_0(w_0 + \delta w_0) \approx U_0(w_0) + \frac{\delta w_0}{w_0} \cdot \psi_{1,0}(w_0) \qquad .$$

The translation δz of the beam waist in the direction of the optical axis can be expanded by LG modes with

$$U_0(z + \delta z) \approx U_0(z) + \frac{i\delta z}{2z_0} \cdot \psi_{1,0}(z) \qquad .$$

Modifications of the optical axis

If the optical axis of the beam is shifted by δx along the x axis and if δx is much smaller then the beam waist ($\delta x \ll w_0$) then the new trace can be expanded by the HG beams with

$$U_0(x - \delta x) \approx U_0(x) + \frac{\delta x}{w_0} \cdot \psi_{l,m}(x) \qquad . \tag{3.15}$$

A shift in x direction is therefore the first approximation expanded with a $\mathrm{TEM}_{1,0}$ mode and a shift in y direction with a $\mathrm{TEM}_{0,1}$ mode.

If the optical axis is tilted by $\delta\alpha$ with respect to the x axis and if this tilt is small compared with the divergence angle of the beam Θ_D ($\delta\alpha \ll \Theta_D$) then it can be expanded by HG beams with

$$U_0 \approx U_0(x,z) + i\frac{i\delta\alpha}{\Theta_D} \cdot \psi_{l,m}(x,z) \qquad . \tag{3.16}$$

3.3 Optical resonators

An optical resonator is an optical element in which light with a defined wavelength circulates for a certain time along a specified, closed path and therefore interferes with itself. This property can be used to precisely measure lengths or frequencies [57] and also for filtering and stabilizing the frequency of the transmitted light [58]. This is important for experiments in the field of gravitational wave detection [59], optical clocks [60, 61] and generation of ultra stable microwaves [62]. The easiest configuration of an optical resonator is one with two mirrors which are placed parallel to each other and a distance l between them. The light can then be reflected back and forth between them. This arrangement is called Fabry-Perot resonator. In the following section some different types of resonators are described. Thereafter the most important parameters of resonators will be explained.

The described resonator parameters are important and helpful to, on one hand characterize the resonator and the other hand design the desired resonator. There are for example cavity designs in which the linewidth or frequency resolution are important or there are cavities like the PC and RC of ALPS-II in which the circulating power is the important factor.

3.3.1 Types of resonators and this stability

There are many different configuration of mirrors possible to build a resonator. In the following section we will discuss a few different types of these configurations. Resonators containing only mirrors with their center on the optical axis and identical Radius of curvature (ROC) R_i are called symmetrical resonators and those with mirrors of different ROC are known as asymmetrical resonators. The ROCs of the mirrors and the resonator length l are the important factors for the stability of the resonator. In the following section the stability criteria for resonators are developed.

In the limits of paraxial approximation the focus of a curved mirror is given by $f = {}^{R}\!/_{2}$ [54]. Every two-mirror resonator with ROCs of R_i $(i = 1, 2)$ and the resonator length l can be described by a repeating pattern of lenses with focal lengths f_i with the same distance l between them [50]. One single roundtrip of the light between the mirrors can be described with equation (3.2)

$$M_g = \begin{pmatrix} 1 & l \\ 0 & 1 \end{pmatrix} \begin{pmatrix} 1 & 0 \\ -\dfrac{2}{R_1} & 1 \end{pmatrix} \begin{pmatrix} 1 & l \\ 0 & 1 \end{pmatrix} \begin{pmatrix} 1 & 0 \\ -\dfrac{2}{R_2} & 1 \end{pmatrix} \qquad .$$

Multiplying the matrices leads to

$$M_g = \begin{pmatrix} 1 - \frac{2l}{R_2} - \frac{4l}{R_1} + \frac{4l^2}{R_1 R_2} & 2l - \frac{2l^2}{R_2} \\ -2\left(\frac{1}{R_1} + \frac{1}{R_2}\right) + \frac{4l}{R_1 R_2} & 1 - \frac{2l}{R_2} \end{pmatrix} \qquad . \tag{3.17}$$

The light in the cavity can be reflected back and forth several times. If the light is reflected N times between the mirrors, it is equivalent to passing through the pair of the lenses for N times. In this case the matrix in equation (3.17) has to be multiplied N times with itself. The result is the new matrix M_g^N. To check the stability of the resonator described by M_g we look for its eigenvalues χ_i. Since both mirrors can be used as an input mirror of the resonator it does not matter from which direction the beam enters. A transfer matrix of such a symmetric system is invertible and therefore fulfills $\det M_g = 1$. For a diagonal 2x2 matrix this leads to $\chi_1 = \chi_2^{-1}$. The resulting diagonal matrix is

$$M_g = \begin{pmatrix} \chi_1 & 0 \\ 0 & \chi_2 \end{pmatrix} \qquad .$$

If the light is circulating N times in the resonator we also have to apply this matrix to the ray in the cavity N times. Suppose the eigenvalues are real and non-equal and $\chi_1 > 1$. Following the relations described in equation (3.1) this leads to a beam that increases the distance from the optical axis every time it gets reflected which ultimately leads to the ray exiting the cavity. The same argument is valid for $\chi_2 > 1$ and increasing angle. Both cases imply an unstable resonator because the rays are exiting the cavity after a certain number of round-trips [48]. The only stable configuration is therefore obtained with eigenvalues of an absolute value of 1. These are usually complex numbers of the form

$$\chi_1 = e^{i\alpha} \qquad \text{and} \qquad \chi_2 = e^{-i\alpha} \qquad \text{with} \qquad \|\chi_i\| = 1 \qquad , \tag{3.18}$$

with α real. These solutions oscillate between increasing and decreasing distance from the optical axis and angle to it respectively. Following the equation (3.17) and [54] the characteristic polynomial is given by

$$\chi^2 - \left[4\left(1-\frac{l}{R_1}\right)\left(1-\frac{l}{R_2}\right) - 2\right]\chi + 1 = 0 \qquad . \tag{3.19}$$

Combining equations (3.18) and (3.19) leads to

$$-1 \leq 2\cdot\left(1-\frac{l}{R_1}\right)\left(1-\frac{l}{R_2}\right) - 1 \leq 1 \qquad ,$$

which is the Fabry-Perot interferometer (FPI) case. This is equivalent to

$$0 \leq \underbrace{\left(1-\frac{L}{R_1}\right)}_{g_1}\underbrace{\left(1-\frac{L}{R_2}\right)}_{g_2} \leq 1 \qquad . \tag{3.20}$$

g_1 and g_2 are called stability parameters. Any cavity with two spherical or plane ($L/R_i = 0$) mirrors that obeys equation (3.20) is in a stable condition. Figure (3.2) is the graphical representation of different resonator configurations. With this diagram and equation 3.20 it can be decided which mirror configurations lead to a stable resonator:

- The plan-parallel resonator with g-parameters of $g_i = 1$ is only marginal stable case and thus very easy to destabilize.
- The symmetrical confocal resonator consisting of two mirrors with ROCs equal to the resonator length $R_i = l$ is very robust. In an optimal case both g-parameters are zero and we are at the origin of the diagram. If l is bigger than R_i, the stability moves along the angle bisector of the diagram in the upper quadrant of the stability region. If l is going to be smaller than R_i, the stability moves along the red line into the lower quadrant of the

stability region. This configuration becomes unstable only if a length change of $\Delta l > 2 \cdot R_i$ occurs.

- If a length of $l = 2 \cdot R_i$ is reached, the cavity is called spherical concentric. This symmetrical configuration contains the focuses of both mirrors in the center of the resonator.

- The fourth configuration which we describe here is hemispherical configuration which consists of a planar mirror with $R_1 = \infty$ and thus $g_1 = 1$ and a concave mirror with $R_2 \gg l$. The beam waist of this configuration is placed on the surface of the flat mirror.

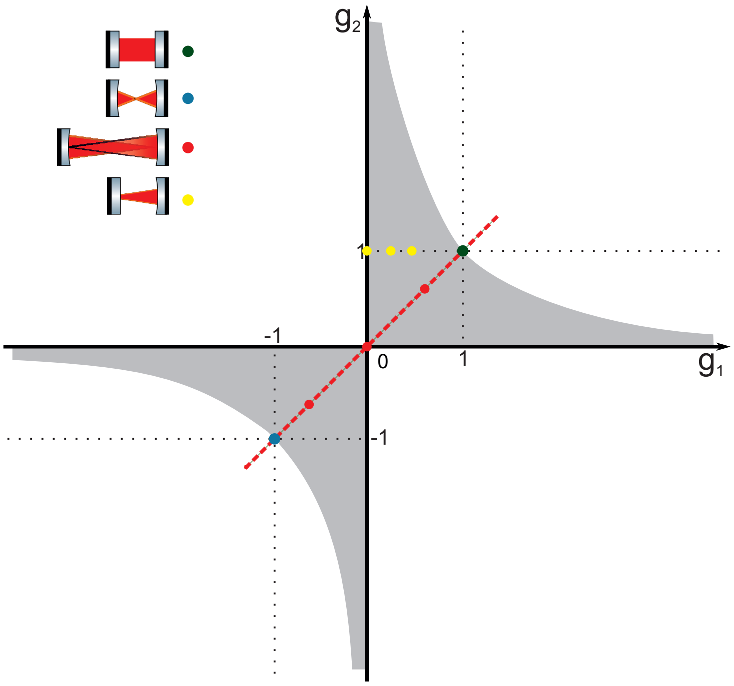

Figure 3.2: The stability diagram of resonators with two mirrors depending on the stability parameters g_1 and g_2. The stable regions are highlighted in Grey. The symmetrical confocal resonator (red dot) is the most stable configuration, it's stability changes with variations of the cavity length along the red line. The planar parallel and the spherical concentric cavities are it's borderline cases (blue dots). The yellow dots describe cavities with one planar and one spherical mirror which is called hemispherical. A configuration like that is supposed to be used in ALPS-II

3.3.2 Free spectral range

We consider a Fabry-Perot resonator with length l. In such a resonator the light is only enhanced if it constructively interferes with itself after a full roundtrip of $2l$. If this is the case a stationary wave arises in the resonator with it's wave nodes at the mirror surfaces:

$$l = n\frac{\lambda_n}{2} \qquad \text{with} \qquad n \in \mathbb{N} \qquad ,$$

where λ_n describes the longitudinal modes of the resonator. Beams which fulfill this condition and constructively interfere at the incoupling mirror have a frequency of

$$\nu_n = n\frac{c}{2l} \qquad .$$

The distance between two longitudinal modes in frequency space is defined as the Free Spectral Range (FSR) ν_F and can be calculate with

$$\nu_F = \nu_n - \nu_{n-1} = \frac{c}{2l} \qquad . \tag{3.21}$$

The FSR of a resonator characterizes it independent from the wave length of light which is circulated in it.

3.3.3 Transmission spectrum

Resonators can also be characterized by their reflexion and transmission properties. We consider a resonator with length l which is consisting of two thin, ideal and identical mirrors M_{in} and M_{end}. This means that we can ignore effects like absorption and scattering on the mirror surfaces and edges. Although we use a non-symmetrical resonator in ALPS-II, this section develops the relevant theory for reasons of simplicity only for the symmetrical case. Relevant features like finesse, full width at half-maximum and free spectral range can be explained with this simple case and can be generalized for other cavities according to [49]. The mirrors have a transmission coefficient t and a reflexion coefficient r which determine the fractions of the field that are being transmitted or reflected respectively. Since we assume ideal, lossless mirrors, the incoming light can only be transmitted or reflected on the mirror.

If a light beam with a field amplitude U_0 passes through the input mirror M_{in} one fraction of it will be transmitted and the rest will be directly reflected. We are interested in the part of light which is transmitted and is now propagating inside the cavity. The light in the cavity is directed towards the end-mirror M_{end}. There, again, a fraction of the light will be transmitted and the rest will be reflected back into the cavity. The transmitted fraction has the field amplitude of U_{0T}. After a full roundtrip this happens again and the resulting fraction which is transmitted by M_{end} has the amplitude U_{1T}. Figure 3.3 shows this process.

Figure 3.3: Schematic transmission process of a cavity.

If this process is repeated N times we end up with the amplitude U_{NT}. We assume that the incoming wave is described by $U_{in} = U_0 \cdot e^{i\omega t}$ It's fraction transmitted by M_{end} can be described with

$$U_{0T} = U_0 t^2 \exp\left(i\omega t\right) \qquad .$$

The t^2 is a result of the light being transmitted twice (once by M_{in} and once by M_{end}). Suppose the phase of the beam that first enters the cavity is zero, than a beam that circulated once in the cavity has a phase difference

$$\begin{aligned} \delta &= k \cdot 2l \\ &= \frac{4\pi l}{\lambda} \qquad , \end{aligned} \tag{3.22}$$

imprinted that depends on the length of the resonator and the wavelength of the light. A beam that circulated N times accumulates a phase of $N\delta$. The fraction of the field that is transmitted by M_{end} after one circulation is therefore

$$U_{1T} = U_0 t^2 r^2 \exp\left[i(\omega t - \delta)\right] \qquad .$$

The filed of all beams transmitted by M_{end} adds up and can be now described with the following equations [63]:

$$\begin{aligned} U_{1T} &= U_0 t^2 r^2 \exp\left[i(\omega t - \delta)\right] \\ U_{2T} &= U_0 t^2 r^4 \exp\left[i(\omega t - 2\delta)\right] \\ &\cdot \\ &\cdot \\ U_{NT} &= U_0 t^2 r^{2N} \exp\left[i(\omega t - N\delta)\right] \qquad . \end{aligned}$$

The resulting field of all transmitted fractions U_{Ti} is the sum over all of them. For sufficiently large N the sum is a complex geometric series which yields [54]

$$\begin{aligned} U_T &= \sum_{i=0}^{N} U_{iT} \\ &= U_0 \exp\left(i\omega t\right) \left[\frac{t^2}{1 - r^2 e^{-i\delta}}\right] \qquad . \end{aligned} \tag{3.23}$$

Experimentally the parameter which is being measured is the transmitted intensity, given by $I = |U|^2$ since we can only measure Intensities, we also can only measure the fractions of the intensity that are being reflected or transmitted by the mirror. The coefficients used in this section so far are defining the fractions of the field and are related to the coefficients for the intensity as follows

$$r = \sqrt{R} \qquad \text{and} \qquad t = \sqrt{T} \qquad . \tag{3.24}$$

Squaring equation (3.23) and using Euler's formula and the relations in equation (3.24) yields the total intensity of the transmitted light I_T

$$I_T = \frac{I_0 T^2}{(1 + R^2) - 2R\cos\delta} \qquad .$$

We can calculate the relation of the transmitted intensity to the intensity of the incoming light field I_0

$$\frac{I_T}{I_0} = \frac{1}{1 + \sin^2\left(\frac{\delta}{2}\right) \cdot F} \qquad , \tag{3.25}$$

where F is the finesse factor of the cavity:

$$F = \frac{4R}{(1 - R)^2} \qquad . \tag{3.26}$$

This factor should not be confused with the cavity quality factor $\mathcal{F}$ which will be discussed in section 3.3.5. The equation (3.25) is called the Airy function and has maximums for all

$$\delta = 2m\pi \qquad \text{with} \qquad m \in \mathbb{N} \qquad . \tag{3.27}$$

Following the geometric arguments for constructive interference of the previous section and the resulting definition of the FSR in equation 3.21, it follows that

$$m = \frac{\nu}{\nu_F} \qquad . \tag{3.28}$$

This leads to the transmission function of the cavity which relates the incoming and transmitted intensities:

$$\frac{I_T}{I_0} = \frac{1}{1 + \sin^2\left(\frac{\pi\nu}{\nu_F}\right) \cdot F} \qquad .$$

On the basis of this Airy function the important properties of the cavity will be described in the next section.

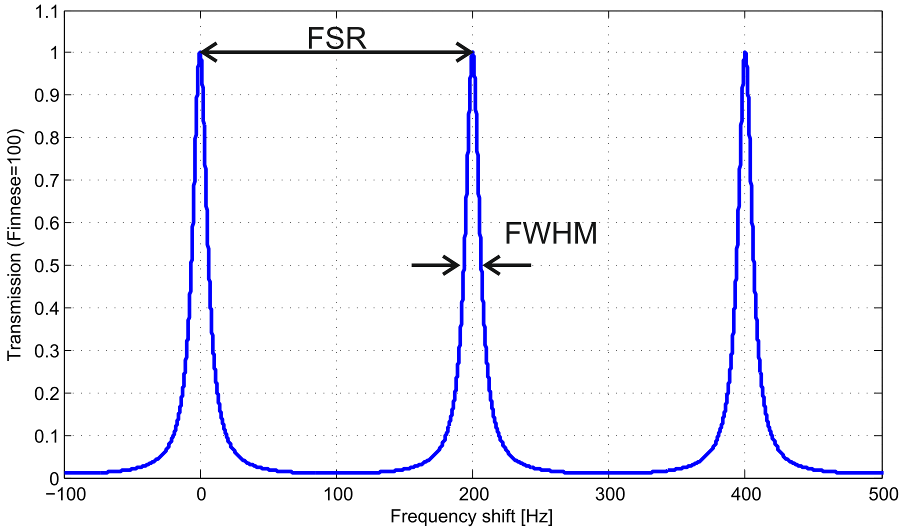

Figure 3.4: The Airy function from the description (3.25) for a lossless, impedance matched cavity with a finesse factor of 100 and a FSR of 200 Hz.

3.3.4 Full width at half maximum

The Full width half maximum (FWHM) describes the width of a (transmitted) spectral peak at the point at which the intensity is half of the maximum transmitted intensity of that peak.

$$\frac{I_T}{I_0} = \frac{1}{2} \qquad , \tag{3.29}$$

This condition combined with the Airy function from the equation (3.25) yields

$$1 + \sin^2\left(\frac{\delta_{FWHM}}{2}\right) \cdot F = 2 \qquad ,$$

where δ_{FWHM} is the phase of the Airy function when the condition (3.29) is fulfilled. Solving this for δ_{FWHM} and applying the fact that the sine is a periodic function together with equation (3.28) which defines m leads to

$$\delta_{FWHM} = 2 \arcsin\left(\sqrt{\frac{1}{F}}\right) + 2 \cdot (m2\pi) \qquad . \tag{3.30}$$

Choosing two neighboring m, both belonging to the same peak, also determines the two frequencies in the peak which both correspond to the half point intensity. Subtracting the two resulting equations gives the distance between the two points defined by the two m, this distance between the points is completely independent of the frequency and therefore the same for each transmission-peak of the cavity and given by

$$\begin{aligned} \Delta\delta_{FWHM} &= 4 \cdot \arcsin\left(\sqrt{\frac{1}{F}}\right) \\ &\approx \frac{4}{\sqrt{F}} \qquad , \end{aligned} \tag{3.31}$$

using the small angle approximation [64]. Equation (3.31) gives the distance between two adjacent phases $\delta_{FWHM}(m)$ and $\delta_{FWHM}(m+1)$ [65]. To observe the relation between the phase and the wavelength we combine equations (3.22) and (3.30) and solve for the frequency to

$$\nu_{FWHM} = \frac{c \cdot \arcsin\left(\sqrt{\frac{1}{F}}\right) + c \cdot (m \cdot 2\pi)}{2\pi l \cdot \cos\varphi(\vec{r})} \qquad . \tag{3.32}$$

The FWHM $\Delta\nu_{FWHM}$ is the result of the distance between two adjacent frequencies ν_{FWHM} of the same Airy peak (see equation (3.25)), that fulfill equation (3.32) (for example $m = 1$ and $m = 2$) and is given by

$$\Delta\nu_{FWHM} = \frac{c \cdot \arcsin\left(\sqrt{\frac{1}{F}}\right)}{\pi l \cdot \cos\varphi(\vec{r})} \qquad . \tag{3.33}$$

For large F and with the use of the small angle approximation, the FWHM frequency can be described as

$$\Delta\nu_{FWHM} = \frac{c}{\pi l \sqrt{F}} \qquad \text{for} \qquad F \gg 1 \qquad . \tag{3.34}$$

3.3.5 Finesse $\mathcal{F}$

The finesse $\mathcal{F}$ is defined as the ratio between properties of a resonator FWHM and FSR and should not be confused with the finesse factor introduced in equation (3.26) and is given by [66]

$$\mathcal{F} = \frac{\nu_F}{\nu_{FWHM}} \qquad . \tag{3.35}$$

To calculate the finesse we combine the equation describing the FSR (3.21) and the equation describing the FWHM (3.33)

$$\begin{aligned} \mathcal{F} &= \frac{\pi}{2\arcsin\left(\sqrt{\frac{1}{F}}\right)} \\ &\approx \frac{\pi\sqrt{F}}{2} \end{aligned} \qquad ,$$

with the finesse factor F as defined by equation (3.26) and the reflectivity of the cavity $R = r_1 \cdot r_2$. The finesse can be described for two unequal end mirrors of the cavity:

$$\mathcal{F} = \frac{\pi\sqrt{r_1 r_2}}{1 - r_1 r_2} \qquad . \tag{3.36}$$

By measuring the finesse of a cavity it is possible to make a statement about the losses of that cavity. A high finesse leads to a large power buildup in the cavity which is desirable for ALPS-II and described in the next section.

3.3.6 Power buildup

The power build-up (PB) is the amplification factor of an optical cavity. It is the ratio between the circulating power in geometrical cavity modes (see also section

3.2.3) P_{cir} and the fraction ηP_{in} of the input power P_{in} that is transmitted into that mode [3]. The PB can generally be calculated with

$$PB = \frac{P_{\mathrm{cir}}}{\eta P_{\mathrm{in}}} \qquad .$$

Since the probability of generating axion like particles increases with increasing laser power (see section 2.2), the PB is an important quantity to achieve the goals for ALPS-II. It is helpful to calculate the properties of the cavity by using the PB factor instead of the finesse because the power in the PC as well as in the RC are important factors for the success of ALPS-II. Contrary to the previous sections of this thesis we will discuss the power buildup of a resonator with non-ideal mirrors which includes losses.

We consider a linear resonator which contains two mirrors with the length l. The incoupling mirror IM has the power transmission coefficient T_{in}. The laser light transmitted through IM is circulating in the cavity. After one round trip the light has the accumulate the phase δ from equation (3.27) and its power is reduced due to the transmission coefficient T_{out} of the cavities end-mirror EM as well as scattering $A_{p,s}$ and absorption $A_{p,a}$ of both mirrors. All these factors of scattering and absorption are summed up to the fractional losses of the cavity mirrors A

$$A = A_{p,s} + A_{p,a} \qquad , \tag{3.37}$$

with the assumption that the transmission and loss factors are small compared to unity (T_{in}, T_{out} and $A \ll 1$) and that the remainder of the phase difference is small ($\delta \mod 2\pi \approx 0$), the power build-up can be calculated approximately to [51, 3]

$$\begin{aligned} PB &= \frac{T_{in}}{1 + (1 - T_{in})\,(1 - T_{out} - A) - 2\sqrt{(1 - T_{in})(1 - T_{out} - A)}\cos\delta} \\ &\approx \frac{4T_{in}}{(T_{in} + T_{out} + A)^2 + 4\delta^2} \qquad , \end{aligned} \tag{3.38}$$

with equations 3.38 and 3.37 we are able to design a cavity with a desired power buildup by calculating the following parameters

$$P_{trans} = \eta P_{in} PB\, T_{out} \tag{3.39}$$

$$P_{loss} = \eta P_{in} PB\, A \tag{3.40}$$

$$P_{refl} = P_{in} - P_{trans} - P_{loss} = P_{in} \cdot (1 - (A + T_{out}) PB \cdot \eta) \qquad , \tag{3.41}$$

where P_{trans} is the transmitted power, P_{refl} is the reflected power and P_{loss} is the power loss due to absorption and scattering at the mirrors inside the cavity.

To calculate the transmissivity of the incoupling mirror T_{in} for the maximum power buildup, we set the derivative of equation (3.38) with respect to T_{in} to zero. This condition is called the impedance matched case and is fulfilled at

$$T_{in} = A + T_{out} \qquad \Rightarrow \qquad PB_{max} = \frac{1}{T_{in}} \qquad , \tag{3.42}$$

this means the highest power buildup and with it also the highest circulating power in the cavity is obtained if the transmission coefficient of the IM is chosen as close as possible to the sum of the losses A and the transmission coefficient of the EM. At the impedance matched case the reflected power described by equation (3.41) is zero and the transmitted power (3.39) at its maximum. In this case the power buildup can be connected to the finesse of the cavity by the expression [67]

$$PB = \frac{\mathcal{F}}{\pi} \qquad . \tag{3.43}$$

By taking the derivative of equation (3.38) with respect to A we can see that there exists no maximum of PB with respect to the losses. Despite of this fact one can determine from equation (3.38) that for a maximum power buildup it is necessary to keep the losses as small as possible. However, even by using the best available optics and building the cavity under the cleanest ambient conditions possible, there are some losses A existing [3]. For a correct calculation of an optical resonator with a defined power buildup, one has to take care of the losses A. To design a cavity with a certain power buildup, which may or may not be impedance matched, equation (3.38) is very helpful. With the relation described by equation (3.43), one can calculate the cavity properties for the designed power buildup.

3.3.7 Over-coupled and under-coupled configurations

In the last section we spoke about the power buildup factor and described the impedance matched case with the equation (3.42). By looking at equation (3.38) one can see that there are many other possibilities to achieve a defined power build-up without having an impedance matched mirror combination. In the impedance matched case a cavity is fully transmitting the light. This means that the complete fraction of the input power that is actually entering the cavity ηP_{in} will be transmitted (leaving aside the part of the power which is lost due the losses described by equation (3.40)). However, there are situations in which an impedance matched cavity is not the best choice as it is briefly described in chapter 2.3. For example, in case of the production cavity of ALPS-II it is not desirable to have the whole input power of 30 W being transmitted in the direction of the regeneration cavity. Especially in the production cavity the circulating power is limited because of the damage thresholds of the cavity mirrors. Therefore it is not advisable to reach the maximum power buildup factor which is described by equation (3.42).

The infrared light transmitted by the PC is mostly needed to produce the green light via second harmonic generation (SHG). Too much infrared power would increase the chance of it leaking through the wall into the regeneration area and disturbing the measurement. For this reason we decided to configure the PC of ALPS-II as an ”over-coupled” cavity. The transmission coefficient of the incoupling mirror IM is bigger than the sum of the transmission of the end mirror EM and the losses of both mirrors. With these specifications we can chose the amount of power which we need for SHG and calculate an over-coupled cavity where the major part of the laser beam is transmitted back through the incoupling mirror.

One should note that in this case it is not valid to use formula (3.43) for the calculation of the finesse because it only applies for the impedance matched case. Instead we have to use equation (3.36). By using this equation we can see that there are different finesse factors existing for the same power buildup. With equation (3.35) it follows that an over- or under-coupled cavity would have a different linewidth than an impedance matched one , provided that power buildup is the same for all cases. Thus, depending on the linewidth, it would be easier or harder to stabilize it, as we will discus in section 3.4. Figure 3.5 shows a simulation of the transmitted and reflected power of the PC of ALPS-II. In all three cases the power buildup is ≈ 5000. Only the reflectivity of the mirrors IM and EM, r_{in} and r_{out} are varied, which means that the power loss is equal in all three cases. As can be seen, the hight of the reflection-peaks in the over- and under-coupled cases is relatively small compared to the impedance matched case. As we will discuss later these peaks are important for the stabilization of the cavity. This means that reflection-peaks with small height or small FWHM could be problematic for the stabilization. Especially stabilizing the cavity on a very narrow peak with a small FWHM is difficult compared to a broad peak. This is one reason why we use an over-coupled cavity.

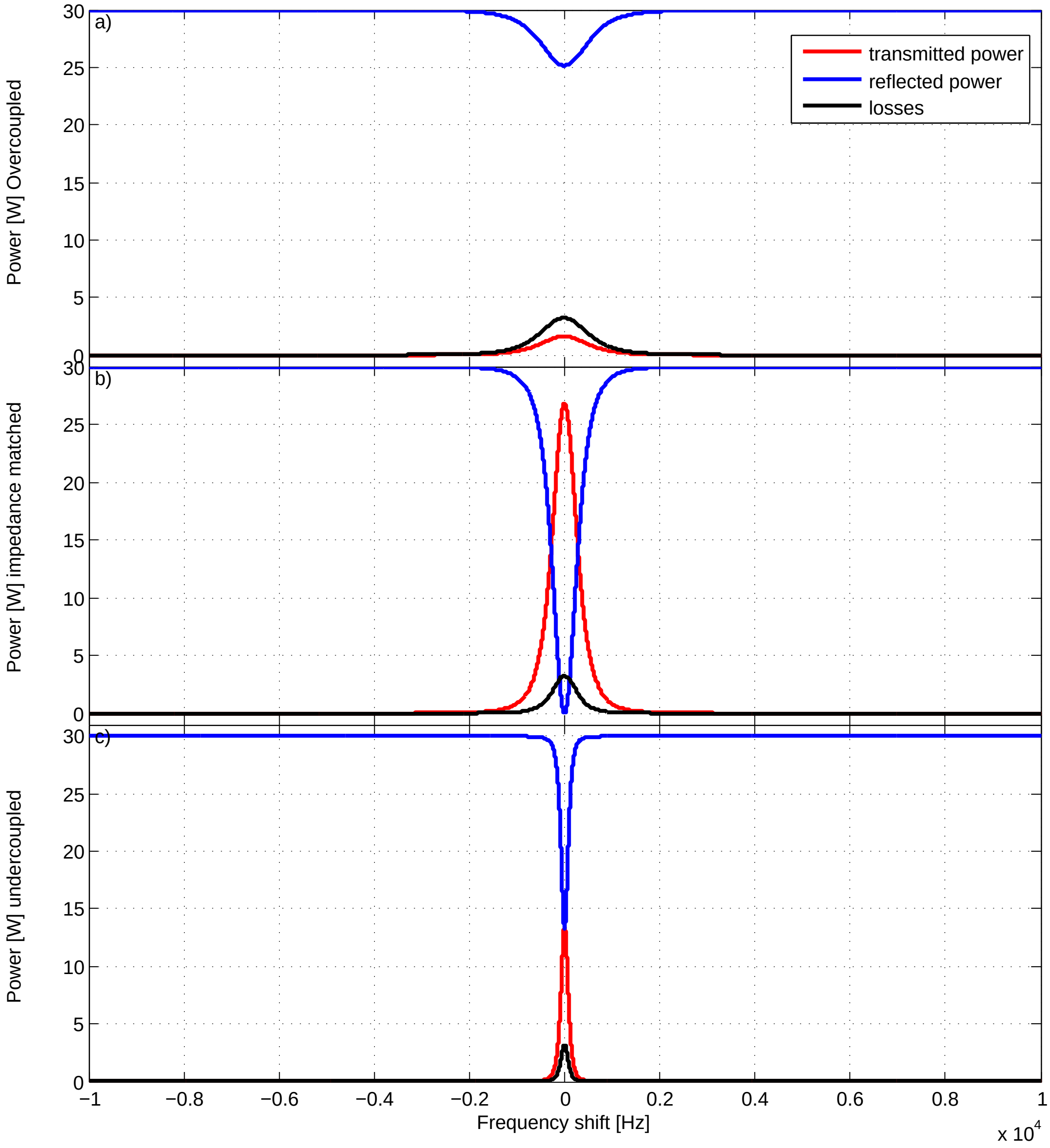

Figure 3.5: Simulation of the transmitted (red) and reflected (blue) power and the losses (black) of the production cavity of ALPS-II with a power buildup of ≈ 5000 at resonance, under the variation of the power transmission coefficients of the incoupling mirror IM and the outcoupling mirror EM, in over-coupled (a), impedance matched (b) and under-coupled (c) cases. From the gradual shrinking of the FWHM from (a) to (c) one can deduce with equation (3.35) that the finesse is gradually increasing.

3.3.8 Photon lifetime and the quality factor Q

The end mirrors of the cavity have a finite transmissivity. As a result of this and the fact that losses in the cavity exist, an injected light field has a finite lifetime in the cavity. Therefore a photon in the cavity also has a finite average lifetime τ inside the cavity. For an injected beam τ is the average time for each photon to be stored in cavity before the photon is lost due to absorption or scattering or simply leaking out at one of the mirrors. We define ε as the energy, stored in the cavity. Assume we feed the cavity with a laser for at least as long as it takes to reach an equilibrium, means that the maximum achievable energy is circulating in the cavity. Now suppose we switch the laser off. To calculate the energy-decay over time in the cavity we look at the derivative of ε with respect to the time [67]

$$\frac{d\varepsilon}{dt} = -\frac{\varepsilon}{\tau} \qquad . \tag{3.44}$$

Solving equation (3.44) leads to a time depended function $\varepsilon = \varepsilon_0 \exp\left(-\frac{t}{\tau}\right)$, where ε_0 is the stored light energy in the cavity at $t = 0$ (when the laser is switched off). After each round trip the intensity in the cavity decays by a factor γ. Therefore the energy loss per unit time can be described as $\frac{d\varepsilon}{dt} = -\frac{c\gamma}{2l}\varepsilon$. With equation (3.44) we can describe the relation between photon lifetime and the FSR from equation (3.21) as

$$\tau = \frac{1}{\nu_F \cdot \gamma} \qquad . \tag{3.45}$$

Consider a cavity with high reflectivity mirrors. The finesse from the equation (3.36) can be approximated to

$$\mathcal{F} \approx \frac{\pi}{1 - r_1 r_2} \qquad \text{for} \qquad r_1, r_2 \approx 1 \qquad .$$

We can use the same approximation for the round trip loss γ and describe $\mathcal{F}$ as function of γ [67]

$$\begin{aligned} \gamma &= 1 - r_1^2 r_2^2 \\ &\approx 2(1 - r_1 r_2) \Rightarrow \mathcal{F} = \frac{2\pi}{\gamma} \qquad , \end{aligned} \tag{3.46}$$

With equations (3.45) and (3.46) and the definition of finesse in equation 3.35

we can describe the relation between the FWHM and the lifetime τ as:

$$\nu_{FWHM} = \frac{1}{2\pi\tau} \qquad . \tag{3.47}$$

The energy loss in the cavity because of the photon lifetime τ determines the cavity quality factor Q. It describes the damping behavior of the system. This Q factor is conceptually the same as in many other damped oscillating systems. In Electrical engineering for example Q is the quality factor of an oscillating electrical circuit. A high Q factor means a lower rate of energy loss compared to the energy stored in the system [68]. This definition can also be used for a cavity to calculate an energy-loss rate of per circulating energy. The Q factor is defined as[69]

$$Q = \frac{2\pi \times \text{stored energy}}{\text{loss of energy per cycle}} \qquad .$$

We can now express the term which describes the loss per cycle in a loss rate and write the loss factor with the resonance frequency ω

$$\begin{aligned} Q &= \frac{\omega \times \text{stored energy}}{\text{energy loss rate}} \\ &= -\frac{\omega\varepsilon}{d\varepsilon/dt} \\ &= \omega\tau \qquad . \end{aligned}$$

With the use of equations (3.3) and (3.47) we can describe Q as a measurement of the frequency resolution

$$\begin{aligned} Q &= 2\pi\nu\tau \\ &= \frac{\nu}{\nu_{FWHM}} \qquad . \end{aligned} \tag{3.48}$$

Using the definition of finesse from equation (3.35) we can calculate the relation between the frequency resolution and the finesse to

$$Q = \frac{\nu\mathcal{F}}{\nu_F} = \frac{\nu\mathcal{F}2l}{c} = \frac{\mathcal{F}2l}{\lambda} \qquad . \tag{3.49}$$

Equation (3.49) states that the frequency resolution of a cavity is equal to its finesse times the number half-waves between the mirrors in a standing-wave cavity [67]. The Q factor can be important to control the frequency behavior of a cavity. In case of ALPS-II, the PC and the RC for are placed on different tables which could have frequency disagreements to each other, calculating Q could be useful.

3.4 Pound-Drever-Hall-Stabilization

Laser systems are subjects to various noise sources that influence properties like power, frequency and phase. Depending on the purpose of the laser it is necessary to suppress noise by stabilizing the desired laser parameter. For this purpose optical cavities can be use as frequency standards and therefore act as a sensor for a feedback control loop. For the stabilization a linear error signal is required for the frequency range in which we want to stabilize our system. To produce such an error signal we use the Pound-Drever-Hall (PDH) method [70, 71, 72]. In the following section a summary of the general laser stabilization, the theoretical background of PDH and the technical realization of it in our experiment is given. In chapter 4 we will discuss the stability of the experiment and therefore also how well the control loop works for the ALPS-IIa setup in Hamburg.

3.4.1 Theoretical description of the Pound-Drever-Hall procedure

For the PDH stabilization either the laser frequency is locked to a cavity resonance or the cavity length is actuated and it follows frequency of the laser. We decided to implement the PDH scheme sensing the reflected light and to stabilize the laser frequency to a resonance of the cavity [73] as depicted in Figure 3.8.

To generate an error signal for the feedback control loop, we measure the beat signal between the laser light, reflected at the cavity and the light transmitted through the incoupling mirror. The intensity of this signal gives us the required information about the resonance frequency ν_0 of the cavity with respect to the laser frequency. However, the change in power of the reflected signal is symmetric about the resonance ν_0 (See Figure 3.6a) and thus it is not possible to tell if the frequency is shifted to higher or lower frequencies than the resonance. But this information can be extracted considering the phase of the reflected signal which is shown in picture 3.6b. The idea behind PDH is to get the needed phase informations by modulating the phase of the laser light before it enters the cavity with a periodic signal. It follows that for a frequency which is bigger than the resonance frequency, a periodic change of the intensity appears, which is in phase with the frequency variation. But for smaller frequencies than the resonance the change in intensity is out of phase by π (See Figure 3.6). With this fact one can compare the changes in intensity and the phase to decide in which direction the frequency has to be shifted. On resonance the reflected signal has a minimum and a small frequency variation will produce no significant change in intensity of the error signal for cavities with low finesse.

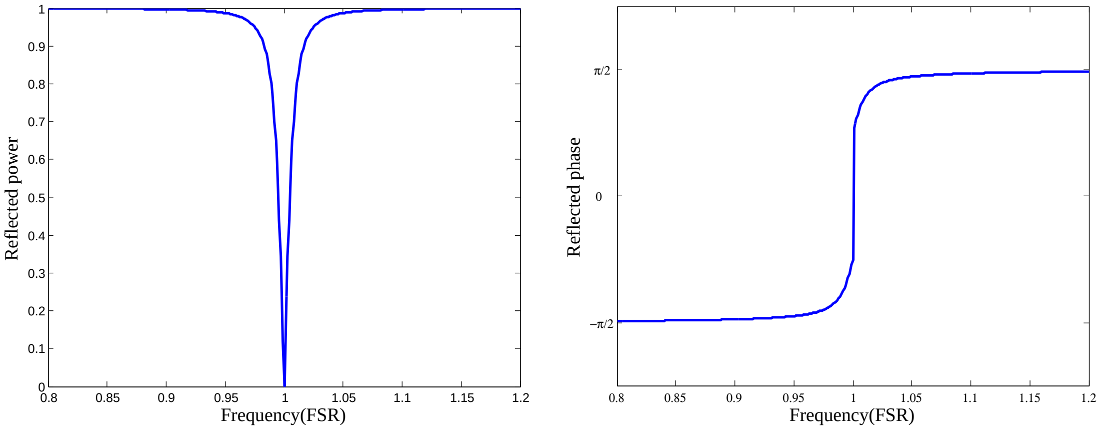

(a) (b)

Figure 3.6: Shown are the power (a) and the phase (b) of the reflection coefficient from equation (3.50) for a cavity with finesse of $\mathcal{F} = 60$. At higher frequencies than ν_0 is the variation of the intensity in phase with the change of the frequency, as shown in (b). For smaller frequencies than ν_0 it is shifted by $\pi/2$.

For the theoretical description of the PDH procedure we consider the electrical fields of the incident beam $U_{in} = U_0 e^{i\omega t}$ and the reflected beam $U_{ref} = U_1 e^{i\omega t}$, with complex amplitudes U_0 and U_1 and the laser frequency ω. For a lossless symmetric cavity the reflection coefficient $F(\omega)$ is given by [73]

$$F(\omega) = \frac{U_{ref}}{U_{in}} = \frac{R\left(\exp\left[\frac{i\omega}{\nu_F}\right]\right) - R}{1 - R^2\left(\exp\left[\frac{i\omega}{\nu_F}\right]\right)} \qquad , \tag{3.50}$$

where R is the field reflectivity of the mirrors and ν_F is the FSR of the cavity. If we modulate the phase of the light before entering the cavity with the frequency Ω and a modulation depth of β (which will be described in the next paragraph)

$$U_{in} = U_0 \cdot \exp\left[i(\omega t + \beta \sin(\Omega t))\right]$$

and expand it with the help of Taylor expansion, neglecting terms with higher orders then

$$\begin{aligned} U_{in} &\approx U_0 e^{i\omega t}\left[1 + i\beta \sin\left(\Omega t\right)\right] \\ &= U_0 e^{i\omega t}\left[1 + \frac{\beta}{2}\left(e^{i\omega t} - e^{-i\Omega t}\right)\right] \qquad , \end{aligned} \tag{3.51}$$

where we can see that in the first order approximation two sidebands arise with frequencies of $(\omega \pm \Omega)$. The power ratio between the sidebands and the carrier with the frequency ω is characterized by the modulation depth β. With this approximation the higher order terms which arise because of the beat between the sidebands themselves are not considered. These higher order terms are not essential for the PDH technique since we need only the ratio between the first two side bands and the main frequency. Equation (3.51) shows that the incident beam can be interpreted as three different beams which co-propagate into the cavity: a carrier-beam and two sideband-beams. For the calculation of the reflected beam, on can consider each of the three beams separately and multiply the components of each by the reflection coefficient $F(\omega)$ and the amplitude of the incident beam U_0. With equation (3.51) the reflected beam is than described by

$$U_{ref} = U_0 \left[F(\omega) e^{i\omega t} + \frac{\beta}{2} \left[F(\omega+\Omega) e^{i(\omega+\Omega)t} - F(\omega-\Omega) e^{i(\omega-\Omega)t} \right] \right] \quad .$$

The only measurable quantity for us is the reflected power $P_{ref} = |E_{ref}|^2$, which is the sum of the power P_c of the carrier at and the power P_s in sideband frequencies $\omega \pm \Omega$ [71]

$$\begin{aligned} P_{ref} &= P_c |F(\omega)|^2 \\ &\quad + P_s \{ |F(\omega+\Omega)|^2 + |F(\omega-\Omega)|^2 \} \\ &\quad + 2\sqrt{P_c P_s} \{ \mathrm{Re}[F(\omega)F^*(\omega+\Omega) - F^*(\omega)F(\omega-\Omega)] \cos \Omega t \\ &\qquad\qquad + \mathrm{Im}[F(\omega)F^*(\omega+\Omega) - F^*(\omega)F(\omega-\Omega)] \sin \Omega t \} \\ &\quad + (\text{terms} \propto 2\Omega) \quad . \end{aligned} \tag{3.52}$$

The terms with Ω arise from the interference between the carrier and the sidebands. The 2Ω terms originate from the cross interference between the sidebands. In figure 3.7 are the first two terms of equation (3.52) shown. One can see the mode of the resonator and the both sidebands at $\omega \pm \Omega$. However, the terms that are important for stabilizing the laser are the two which oscillate at the modulation frequency Ω. Because these terms sample the phase of the reflected carrier. All the other terms can be neglected for this calculations. In the experimental setup these disturbances can be filtered by a low-pass band filter. If the modulation frequency is large compared to the FWHM of the cavity $(\Omega \gg \nu_{FWHM})$ than the sidebands don't enter the cavity and are getting reflected nearly completely and the reflection coefficients for both sidebands are therefore equal and real. The term

$$F(\omega)F^*(\omega+\Omega) - F^*(\omega)F(\omega-\Omega)$$

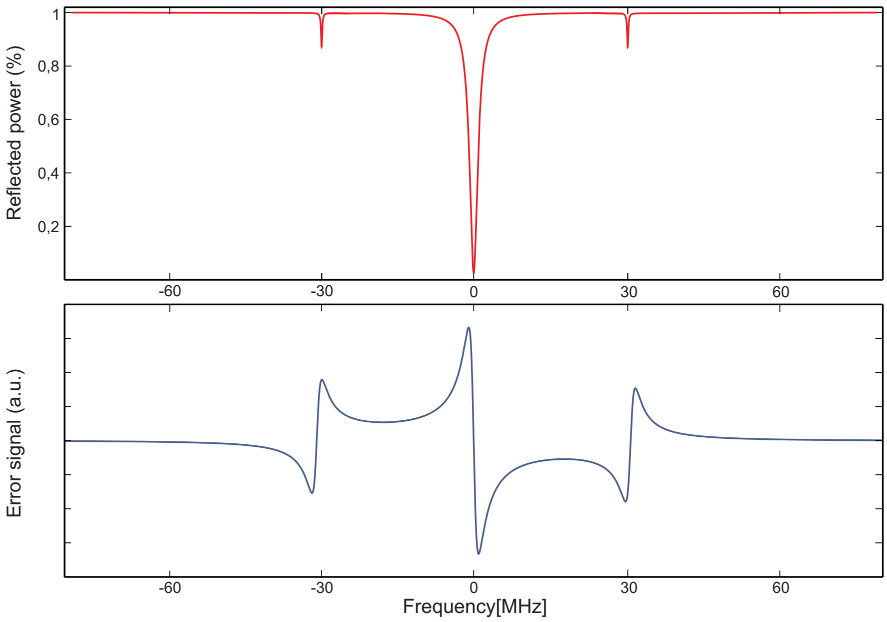

Figure 3.7: In picture (a) the reflected power of the modulated signal is plotted. The carrier and frequency and both sidebands are shown. Picture (b) shows the PDH error signal with a modulation frequency of $\Omega = 30\,\mathrm{MHz}$. The steep zero-crossing at the resonance frequency is used to stabilize the laser and the cavity onto each other. Both smaller zero-crossings are caused by the sidebands.

is therefore completely imaginary. Thereby the factor in front of the cosine term in equation (3.52) vanishes and only the sine term is left. For ($\Omega \ll \nu_{FWHM}$) on the other hand, only the cosine term is taken into account.

To investigate the interesting $\sin(\Omega t)$ and $\cos(\Omega t)$ parts of the reflected power in equation (3.52) we have to separate this modulated signal from the rest of the signal which is caused by the non-oscillating term of equation (3.52). This can be done with the technique known as demodulation which transforms frequency components of the detected signal at the modulation frequency into a constant signal and the other components to a somehow oscillating one which than can be filtered with a low pass. To demodulate we multiply the signal with a reference signal at the demodulation frequency Ω'. For the non-oscillating terms this is means that they are multiplied with $\sin \Omega'$ and the result also oscillates at frequency Ω'. The already oscillating terms produce frequencies at the sum and difference of the modulation and demodulation frequencies since the the product of two sinus waves is [55]

$$\sin(\Omega t)\sin(\Omega' t) = \frac{1}{2}\{\cos[(\Omega - \Omega')t] - \cos[(\Omega + \Omega')t]\} \quad . \tag{3.53}$$

If we use a device like a mixer which is able to multiply two incoming electrical signals and both modulation and demodulation signals would operate at the same frequency ($\Omega = \Omega'$), the $\cos[(\Omega - \Omega')]$ is a constant (DC) signal. The other term oscillates fast so that it can be filtered out. It is important to ensure that both mixed signals have no phase shift. If a sine and a cosine signal would be mixed than, instead of equation (3.53), we arrive at

$$\sin(\Omega t)\cos(\Omega' t) = \frac{1}{2}\{\sin[(\Omega - \Omega')t] - \sin[(\Omega + \Omega')t]\} \tag{3.54}$$

and the DC signal vanishes and the resulting error signal from the mixer can be difficult to use [74]. For measuring the error signal at low frequencies one has to take into account that the phase of the two mixing signals have to be matched. This can be easily fulfilled with a $\pi/2$ phase shifting of the modulation signal. The desired error signal which we want to use for the stabilization is the result of the mixing of the two sine signals. This error signal has the phase information of the reflected light. Thus it vanishes at the resonance frequency ν_0 and shows different signs for higher or lower frequencies than the resonance. The error signal is described by

$$\varepsilon = -2\sqrt{P_c P_s}\,\mathrm{Im}\left[F(\omega)F^*(\omega + \Omega) - F^*(\omega)F(\omega - \Omega)\right] \quad . \tag{3.55}$$

Picture 3.7 shows the error signal of equation (3.55) for a high modulation frequency with respect to the detuning of the resonance $\Delta\omega = \omega - \nu_F$. Near the resonance frequency ν_{FSR} in the linear regime of the function the signal slope is $\varepsilon = 4\frac{\Delta\omega}{\Delta\nu_F}$. The slope of the PDH error signal is for higher finesse and thus smaller cavity line width $\Delta\nu_F$ steeper. This means that the PDH works more exactly the higher the finesse of the cavity is. Because even smaller frequency changes respectively length changes lead to higher error signal fluctuations. In the following section the experimental setup of PDH will described.

3.4.2 The experimental setup of the Pound-Drever-Hall stabilization

The theoretical derivation of the PDH error signal was discussed in the previous section and the error signal is describes in equation (3.55). For practical use, the theoretically described signals have to implemented electronically.

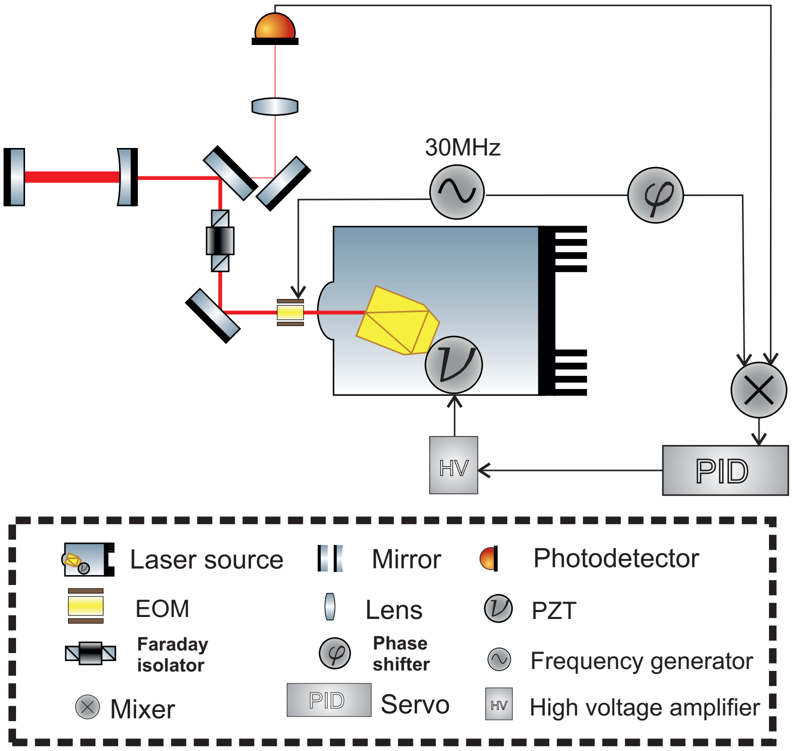

Figure 3.8: The scheme of the PDH frequency stabilization for the ALPS-II production cavity at it's current state. The sidebands are added to the laser light via an EOM which is implemented in the laser system. The laser is locked to the cavity with the feed back control loop.

For the ALPS-II PC the frequency of the incident laser light (See section 4.3.1) has to be matched to the resonance frequency of the PC. The modulation frequency for producing the error signal, which will be used for the PC control loop, is 30 MHz and is being generated by a signal generator. For later operations of the ALPS-II PC the usage of a dedicated local oscillator (LO) is planned which will provide the oscillation signal for the PDH. The modulation signal for the sidebands is implemented to the laser beam by an Electro-Optical Modulator (EOM), which is part of in the Master-Oscillator-Power-Amplifier (MOPA) laser system. Together with the sidebands the result is a reflected field which is detected by the photo detector PD1. It is equipped with an additional readout path, which is resonant at the modulation frequency and chosen to improve the signal-to-noise ratio (SNR) [3, 75]. The signal from the PD1 is now directed to the mixer which performs the needed multiplication of the signals from the photo detector and the signal generator. This multiplication is described in equation (3.53). At the output of the mixer a low-pass filter is integrated which filters the disturbances which appears also as results of the modulation. If this signal from the photo diode is demodulated we receive the desired error signal from the expression (3.55). It is easy to avoid the situation described by equation (3.54) with the use of a signal generator which has two synchronized output channels with adjustable phase. By using a dedicated LO a phaser shifter is necessary. Alternatively, one can adapt the lengths of the connection cables to ensure that we mix the two sine signals that are not phase shifted with respective to each other. The demodulated signal will be send to a proportional-integral (PI) controller. The PI controller which we use for realizing the control loop for the ALPS-II PC is the same circuit which was used in the ALPS-I experiment [1, 3]. The output of the PI controller is than amplified by a High Voltage (HV) amplifier with a dynamic range of ±150 V and fed to the piezoelectric transducer of the non-planar ring oscillator (NPRO). If the cavity length and with it the resonance frequency of the cavity changes, the frequency of the laser will follow. The control loop ensures that the error signal is always zero. This corresponds to the minimum reflection signal on the photo diode and also the maximal coupling in the cavity.

Chapter 4

ALPS-II Experiment

This chapter gives an overview of the optical part of the ALPS-II experiment. The general idea behind LSW experiments is described in section 2.2, and the main concept of ALPS-II is discussed in 2.3. We explain the three stages of ALPS-II and show the improvements and differences of the new experiment compared to its successful predecessor ALPS-I [1, 2]. First we introduce the general optical design of ALPS-II and discuss the resonator parameters of the three experimental stages from ALPS-IIa to ALPS-IIc which are mentioned in section 2.3. After that we compare the optical setup of ALPS-II with those of ALPS-I and describe the improvements and also the new challenges. With the design of ALPS-II in mind, we take a look at the central breadboard as it is the heart of the optical design of ALPS-II and describe briefly its technical specifications. Thereafter we will concentrate on the ALPS-IIa Hamburg experiment and the design and setup of the production cavity of ALPS-II which is one of the main parts of this thesis.

4.1 Optical design and aims

In section 2.2 we spoke about the general concept of the LSW experiments and defined the production and regeneration areas of such experiments. In section 2.3 we also introduced the ALPS Production Cavity (PC) and Regeneration Cavity (RC). We spoke about the enhancement of the experiments sensitivity by using the new optical design including the RC which increases the production probability of photons that are created from the axion field. In this section we will describe the general scheme of ALPS-II and summarize the parameters which we have to consider while designing the cavities.

4.1.1 Eigenmode and aperture

In the concepts of both ALPS experiments [43, 3] the PC is used to provide a field strength as high as possible from which some photons possibly convert to the axion field. As explained in section 2.3 the RC is intended to increase the photon field that was potentially regenerated from the axion field. In chapter 2 it is shown that the photons which are circulating in the RC have the same parameters as the photons in PC. Thus the Gaussian beam parameters of the regenerated field are the same than those of the circulating field in the PC. For efficiently increasing the regenerated field the eigenmode of the RC has to be matched to the eigenmode of the regenerated photons, which have the eigenmode of the PC since they were generated there [76], thus the optical axis of both cavities have to be collinear. The consequence for two hemispherical cavities (see section 3.3.1) with the same length like PC and RC is that the waist of the eigenmode should be at the flat mirrors which are mounted back to back to each other with some space in between for the light-tight wall. Figure 4.1 shows this configuration.

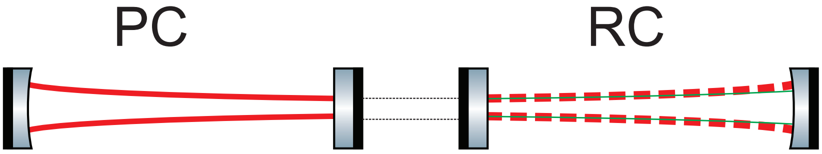

Figure 4.1: Eigenmodes of the production cavity with the infrared power enhancement (red continuous lines) and the regeneration cavity with the enhancement of the regenerated photon field (dotted red lines). The thin green line shows the control light of the RC as mentioned in section 2.3.

The next point which should be considered for designing ALPS-II is the effective maximum aperture which we can use in both cavities. As mentioned in chapter 2 the conversion probability of an ALP to a photon increases linearly with the strength of the external magnetic field B. ALPS-II will make use of the dipole magnets from the HERA which are described in section 2.3 to generate the magnetic field. After being straightened the free aperture inside the magnets will be approximately 50 mm [46, 43]. Considering alignment tolerances of the input beam, planarity of the vacuum pipe inside the magnet and fluctuations of the laser position (pointing), 10 mm are required to compensating these errors. This leaves effectively a free aperture of 40 mm to use. The requirements on the eigenmodes of both cavities and the usable aperture of the HERA magnets are the most critical points that influence any decision concerning the length of the cavities and the size of their beam waist. In the next section we will describe the desired power buildup factor (see also section 3.3.6) of the cavities. After that we will describe the geometrical parameter of the PC and the RC.

4.1.2 Power build-up and Finesse of PC and RC

The benefit of high power enhancement factors of both cavities is to rise the sensitivity of our LSW experiment. The sensitivity factor is depending on several factors and is discussed in detail in chapter 2, we remind ourself that it should be as small as possible and write expression (2.5) here again to recollect:

$$S(g_{a\gamma}) \propto \frac{1}{BL}\left(\frac{DC}{T}\right)^{1/8} \cdot \left(\frac{1}{\eta \boldsymbol{\dot{N}_{Pr}}\, \boldsymbol{PB_{PC}}\, \boldsymbol{PB_{RC}}}\right)^{1/4} \quad . \tag{2.5}$$

The bold parameters are the important factors from the optical point of view. The number of photons per seconds that are generated by the laser source is $\dot{N}_{Pr}$, which will be described in this chapter. The factors PB_{PC} and PB_{RC} are the power buildup factors of the production cavity and the regeneration cavity. The sensitivity factor of the experiment improves proportional to the inverse of fourth-root of these factors. For the ALPS-II experiment the same laser source than for ALPS-I is used. There for the same number of photons $\dot{N}_{Pr}$ is emmited by the laser. Although we can gain higher PB factors in both cavities which lead to a better sensitivity of the experiment. To achieve a better power buildup the parameters of the cavities are different:

Production Cavity

The circulating power inside the PC is limited by the damage threshold of the mirror-coating due to thermal effects. The mirrors we use for ALPS-II are fused silica [77] substrates of the type (SQ1) with an ion-beam sputtering (IBS) coating. The IBS methode provides a high quality uniform coting with low roughness on the surface [78]. The mirrors are produced by the company LASEROPTIK [79]. Our mirrors have a damage threshold of a few 1000 kW/cm^2 [43]. For the ALPS-II PC we decided to stay well below the damage threshold and to limit the maximum intensity on the mirrors to 500 kW/cm^2 [43]. This is a power level on which laser systems like the Advanced LIGO pre-stabilized laser are working over a long period of time at the same wavelength as ALPS-II without damaging the mirrors [80].

An input power of 30 W and a power buildup factor of approximately 5000, lead to a circulating power of P_{cir} of 150 kW inside the PC. With a beam waist of not more than 6 mm on the surface of the flat end mirror we will operate with no more than 270 kW/cm^2 and thus far below this threshold.

From the general idea of the ALPS-II and from the explanation of the LSW experiments in chapter 2 it is known that it would not be advisable to have all the in-coupled laser power P_{in} transmitted through the PC towards the opaque wall on central breadboard (CB). Unfortunately this would be the case for the impedance matched cavity (as explained in section 3.3.6) in which the transmitted power from expression (3.39) has its maximum and the reflected power from equation 3.41 is zero. Considering at these two factors: high circulating power in the cavity and low transmitted light from the cavity, we have decided to configure the PC as an over coupled cavity which is described in section 3.3.7. The mirrors from LASEROPTIK were ordered with specified values of lesser than 5 ppm for the scattering losses A_s and less than 6 ppm for the absorption losses A_a. The transmission of the flat end mirror is chosen to be $T_{out} \approx 11$ ppm to achieve about 1 W light transmitted onto the central breadboard (CB). With these values and equation (3.38), we can determine the optimum transmission of the incoupling mirror T_{in} to $T_{in} \approx 750$ ppm.[1] With these values the power buildup in the PC of $PB_{PC} \approx 4900$ is evaluated. We can calculate the finesse of the PC: $\mathcal{F}_{PC} \approx 8020$ (see also equation (4.10)). One should note that expression 3.43 does not apply for a cavity which is not impedance matched.

Regeneration Cavity

The regeneration cavity does not have to store a high amount of infrared light but it is needed to increase the probability of regenerating a photon from the ALP field. Therefore the considerations about the damage threshold of the mirrors are not necessary. The RC can be designed with the highest possible power buildup. The only limitation to the PB in the RC are the losses $A_s = 5$ ppm and $A_a = 6$ ppm (see section 3.3.6). With the objective of maximizing the circulating power in the RC in mind we decided to design this cavity as an impedance matched cavity. With a look at expression (3.42), we can see that, to achieve this situation, we need to make the transmission of the incoupling mirror T_{in} equal to the sum of the transmission of the outcoupling mirror T_{out} and all cavity-losses. The interesting point concerning the RC is that there is no designated incoupling mirror existing in the conventional meaning. The RC enhances the regenerated photon field which

---

[1] While measuring the transmission factor of 750 ppm was simple to perform and measuring the small transmission of 11 ppm was, with some efforts, also possible, measuring of the losses is problematic. At the moment we have to trust the information the manufacturer provided.

is not transmitted into the cavity through one of the mirrors but reconverted from the ALP filed inside the cavity. The field will leave the cavity through both mirrors. This situation is shown in figure 4.2. In conclusion, we are free to designate one of the mirrors as the incoupling mirror and set the transmissivity of this mirror equal to $A + T_{out}$. To push the power buildup as high as possible we have to choose T_{out} as low as possible. This means that the regenerated infrared photons will leave the cavity predominantly through the mirror with the transmissivity T_{in}.

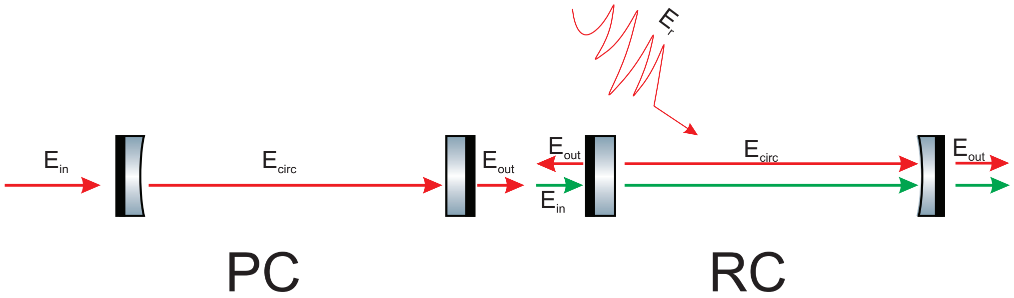

Figure 4.2: Fields in the production cavity and the regeneration cavity. While the infrared beam of the PC and the green control beam of the RC are transmitted through the incoupling mirrors of their respective cavity, the regenerated infrared photons are being converted inside the RC. These photons are leaving the cavity through one of the mirrors.

This demands a decision at which place we want to set up the detector of ALPS-II. For this decision it is also important to pay attention to the green control light in the RC which is mentioned in section 2.3 and will also be described below. We decided to set the detector in the middle lab, next to the incoupling mirror of the RC and close to the CB because the current auto alignment scheme does not compensate for lateral movements of the table on which the outcoupling mirror of the RC is mounted. Putting the detector on that table would lead to a relative movement between the detector and the stabilized spacial cavity mode which would lead to a moving spot on the detector. With the considerations mentioned above we chose the transmissivity of the curved mirror as low as possible with $\approx 3\,\text{ppm}$. The sum of the scattering and absorption losses of both mirrors is roughly 22 ppm. This leads to a desired transmissivity of the flat mirror of $\approx$25 ppm. With these values the power buildup of the RC can be calculated to be $PB_{RC} \approx 40000$. This cavity is in contrast to the PC impedance matched and we can use formula 3.43 to calculate the finesse to $\mathcal{F}_{RC} \approx 120000$. As explained in section 2.3 the control light of the RC will be provided by a 532 nm beam. Although this wavelength should be far away from the wavelength of the regenerated photons, it is advisable to control the cavity with as little green power as possible to minimize the probability of a green photon reaching the detector. Thus the mirrors of the RC are also coated for green light. Contrary to the infrared field, the green beam has a defined input mirror which is the flat mirror. This mirror has a transmissivity of ≈5% for green photons while the curved mirror has a transmissivity of ≈1%. With these values the power buildup factor of the RC for green light is ≈ 55. We should note that because of different coatings for the 532 nm and 1064 nm beams, the penetration depth of these two wavelengths into the cavity mirrors is different. This means that the cavity has for each wavelength a different resonant frequency. This is problematic as long as we want to stabilize the cavity with help of green photons for the regenerated infrared photons. How to circumvent this problem is explained in section 4.2.1 where we describe the general concept of ALPS-II.

4.1.3 Cavity length and Radius of curvature

The calculated power buildups can only be reached if we can prevent additional losses in the cavity due to clipping of the Gaussian beam at edges or borders of the setup. For the decision that sets the cavity length it is important to remember the free available aperture through the magnets. As described above we can assume an aperture with $r_{ap} = 20\,\text{mm}$ radius after straightening the magnets. We have only a finite size of aperture at our disposal and we want the cavity length to be as long as feasible. Therefore we have to calculate the optimum diameter and divergence of the beam inside the cavity which is directly related to the beam size at the cavity end (at the curved mirrors) $w(z)$ and the waist w_0 at the flat mirrors (see equation (3.8)). This means that we have to minimize $w(z)$ at a given z with respect to w_0. We look again at equation (3.6) and set the derivative of it with respect to w_0 to zero.

$$\frac{dw}{dw_0} = -\frac{2\lambda^2 z^2}{\pi^2 w_0^4 \sqrt{\frac{\lambda^2 z^2}{\pi^2 w_0^4} + 1}} + \sqrt{\frac{\lambda^2 z^2}{\pi^2 w_0^4} + 1} \overset{!}{=} 0 \qquad , \tag{4.1}$$

solving this equation (4.1) for z gives the optimum length of the cavity with respect to w_0 and λ:

$$z = \frac{w_0^2 \pi}{\lambda} \qquad . \tag{4.2}$$

We can see that z is nothing else than the Rayleigh length described in equation (3.7) and in [81]. With the explanation regarding the eigenmodes in section 4.1.1 and the discussion above we can say that the Gaussian beam inside the cavity has minimum losses that can be contribution of beam clipping with the beam waist at one of the end mirrors and the cavity length equal to the Rayleigh length of the beam [43, 81]. As we can design the geometrical properties of the Gaussian beam inside the cavity by determining the shape of the end mirror, we should first determine the length of the cavity.

To obtain the power buildup factors of the RC and PC, we calculate the losses due to clipping at the free aperture of the magnets r_{ap} and add these to the total losses A from the equation (3.37). The production and regeneration cavities of ALPS-II will have their beam waist at the plane mirrors. Therefore the clipping losses will appear on the outer mirrors as it is shown in figure 4.1. For a hemispherical cavity with the length l and the the beam radius $w(l)$ at the curved mirror the losses are given by [51]

$$A_c = \exp\left[\frac{-2r_{ap}^2}{w(l)^2}\right] \qquad . \tag{4.3}$$

We can therefore include these additional clipping losses into expression 3.38:

$$PB \approx \frac{4T_{in}}{(T_{in} + T_{out} + A + A_c)^2} \qquad . \tag{4.4}$$

Solving this equation for A_c and inserting it in equation (4.3) gives a relation between the waist on the curved mirror, the power buildup and the free aperture. As was shown above the optimum distance between the mirrors of our cavities is equal to the Rayleigh range.

This leads to a relation between the minimal aperture and the length of the cavity for a fixed power buildup factor.

$$r_{ap} = \sqrt{\frac{l\lambda}{\pi}} \cdot \sqrt{-\ln\left(\sqrt{\frac{4T_{in}}{PB}} - T_{in} - T_{out} - A\right)} \qquad , \tag{4.5}$$

this equation is plotted in figure 4.3 for both power buildup factors of the PC and RC. This plot shows that with the available free aperture of the magnets of 4 mm, the power buildup of $PB_{RC} \approx 40000$ is feasible for a cavity length of not more than 100 m. The requirements for the PC are less critical in this range, because of its lower power buildup factor, larger clipping losses are acceptable. This means a longer PC would be possible. However, the infrastructure of the HERA tunnel [43] does not allow for this option. Equation (4.5) shows that for longer cavities a larger aperture will be necessary to prevent limitations due to clipping losses. It also shows that a beam with a shorter wavelength allows for a longer cavity with the same power buildup. For example it is shown in [3] that a regeneration cavity for 532 nm light with 200 m length would be possible with the same free aperture. As the sensitivity of the LSW experiments is strongly depended on the length of the production and regeneration areas it follows that an experiment with visible light will achieve a higher sensitivity than an experiment with infrared light. The reasons for designing ALPS-II with infrared light are mentioned in chapter 2.3 and explained in more detail in [3].

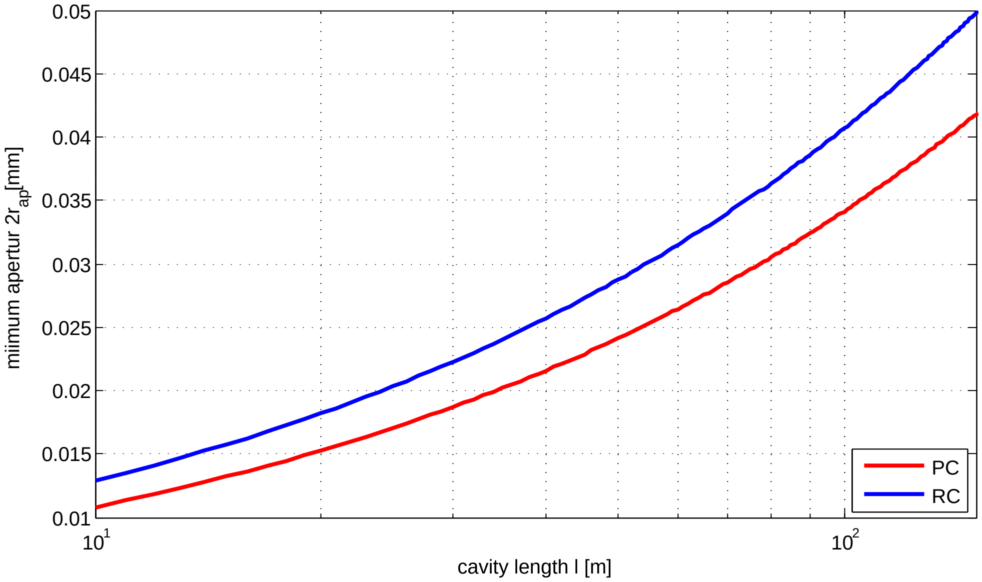

Figure 4.3: The minimum allowed aperture size that allows the power buildup factors of the production and the regeneration cavities. The mirror parameters of the cavities are given in section 4.1.2 .

With the information about the cavity length we can calculate the beam waist w_0 of the cavities by using equation (3.7). With a beam waist of $w_0 = 5.9\,\mathrm{mm}$ for both cavities we can calculate the ROC of the curved mirrors. From equation (3.6) it follows:

$$R = \frac{(w_0^2\pi/\lambda)^2}{l} + l \tag{4.6}$$

and we receive a ROC of $R \approx 200\,\mathrm{m}$ for the curved mirrors. To use the same mirrors in all three ALPS-II stages the ROCs of the purchased curved mirrors are

250 m. With the intensity of the Gaussian beam

$$I = \frac{2P}{\pi w_0^2} \quad , \tag{4.7}$$

we can calculate the peak intensity on the flat mirror of the production cavity. With a beam waist $w_0 = 5.9\,\mathrm{mm}$ and a circulating power of $P_{cir} = 150\,\mathrm{kW}$, to $270\,\mathrm{kW/cm^2}$ which is far below the damage threshold of our IBS coatings.

Knowing the geometrical properties of ALPS-II we can briefly describe the complete setup of the experiment in the following section and compare it with its predecessor experiment.

4.2 Concept of ALPS-II

After the considerations about the parameters of both ALPS-II cavities, we remember the task of the RC, which is increasing the probability of regenerating light from the axion field. The regenerate field benefits from the power buildup in the RC, if PC and RC have a common optical axis. Two Gaussian beams which are propagating along a defined axis for example the z-axis and have to be matched to each other can have differences in their alignment, that includes the translations δx ,δy, the angles $\delta\Theta_x$ and $\delta\Theta_y$, the waist position δz_0, the waist size δw_0 and also the waist position along the x- and y-axis [82]. For ALPS-II it is important to keep this differences small to have a high matching of the eigenmodes of both cavities. To reach this goal it is planned to use rectangular substrates for the flat end mirrors of RC and PC and mount them both onto the CB to ensure a stable relation between these two mirrors. The cavity eigenmodes will be aligned with respect to these mirrors. The requirements on the spatial differences between the two cavities of ALPS-II are discussed in [3] and [43] and can be directly connected to a requirement on the planarity of the CB which will be discussed shortly in the next section.

Since the infrared light cannot be used for the length control of the RC, as it would contaminate the detection signal, light at a difference wavelength was chosen to ensure the resonance condition of the RC. This wave length should be - as mentioned in 2.3 - outside of the spectral acceptance range of the ALPS-II detector. To achieve this we are using 532 nm laser light as control light for the RC. Below we will describe the concept for providing this light and also the alignment of both cavities as well as the general concept of ALPS-II before we concentrate on the production cavity of ALPS-IIa which was build as a part of this thesis.

4.2.1 Optical Scheme and general description

In this section we will describe the optical scheme of ALPS-IIc which is basically the same scheme as the one of ALPS-IIa including the regeneration cavity. The difference between the ALPS-IIc scheme and the scheme of the ALPS-IIa including the production cavity, which is currently running in Hamburg, lies in the stabilization of the laser frequency to one of the resonance frequencies of the PC. In the scheme described in this section we intent to use piezo-electric transducer (PZT)s for aligning the laser beam to the eigenmode of the PC. Furthermore it is intended to use photodiodes for sensing the parallel shift and tilt of the laser beam with respect to the PCs optical axis via the differential wavefront sensing (DWS). All of these devices (two PZTs and two photodiodes) were not included in the first setup of the production cavity. Figure 4.4 shows the general optical setup of the ALPS-II experiment. Below we will briefly explain the working principle of this setup and explain important components for the alignment of the RC.

On optical table 1, two PZT mirrors AM1 and AM2 are depicted. These mirrors are needed for an auto alignment of the 100 m ALPS-IIc production cavity. These mirrors guide the infra red light to M1 which has, a transmission of 1% for the infrared light. Via M1 the light is send to the PIC which is the curved mirror of the PC with a ROC of 250 m and a transmission of 750 ppm. These values have been discussed in the previous section. 1% of the reflected light from the cavity transmits through the mirror M1 and is subsequently split via a beam splitter onto two quadrant photodiode (QPD)s [83] (QPD1 and QPD2). The detection area of these photodiodes is divided into four quadrants with the signals of these quadrants we can obtain informations about shifts and tilts of the optical axis of the cavity with respect to the laser beam by using the DWS scheme [84]. One of these QPDs will be used for the PDH signal detection by taking the sum of all four quadrants. In the current setup, instead of QPD1, a single element photodiode PD1 is installed. The reason for that is explained in section 3.4.2. A PZT for fast positioning is attached to the PIC mirror such that we can either use this one or the PZT in laser to keep the PC resonant. Since we currently use the laser PZT for this purpose, the PZT on the PIC not installed yet.

The flat mirror of the PC, labeled CBS1a, is mounted on the central breadboard (CB). This breadboard is marked in the figure 4.4 with a beige background. We will discuss the properties of this board in the next section. The purpose of using this board is to have a stable, common optical axis between the PC and RC. To accomplish this, it is planned to mount the flat mirrors of both cavities directly on the CB and fix them in a way in which they are precisely parallel to each other. One has to note possible complications concerning translations and tilting of these mirrors with respect to each other. The resulting requirements on the relative

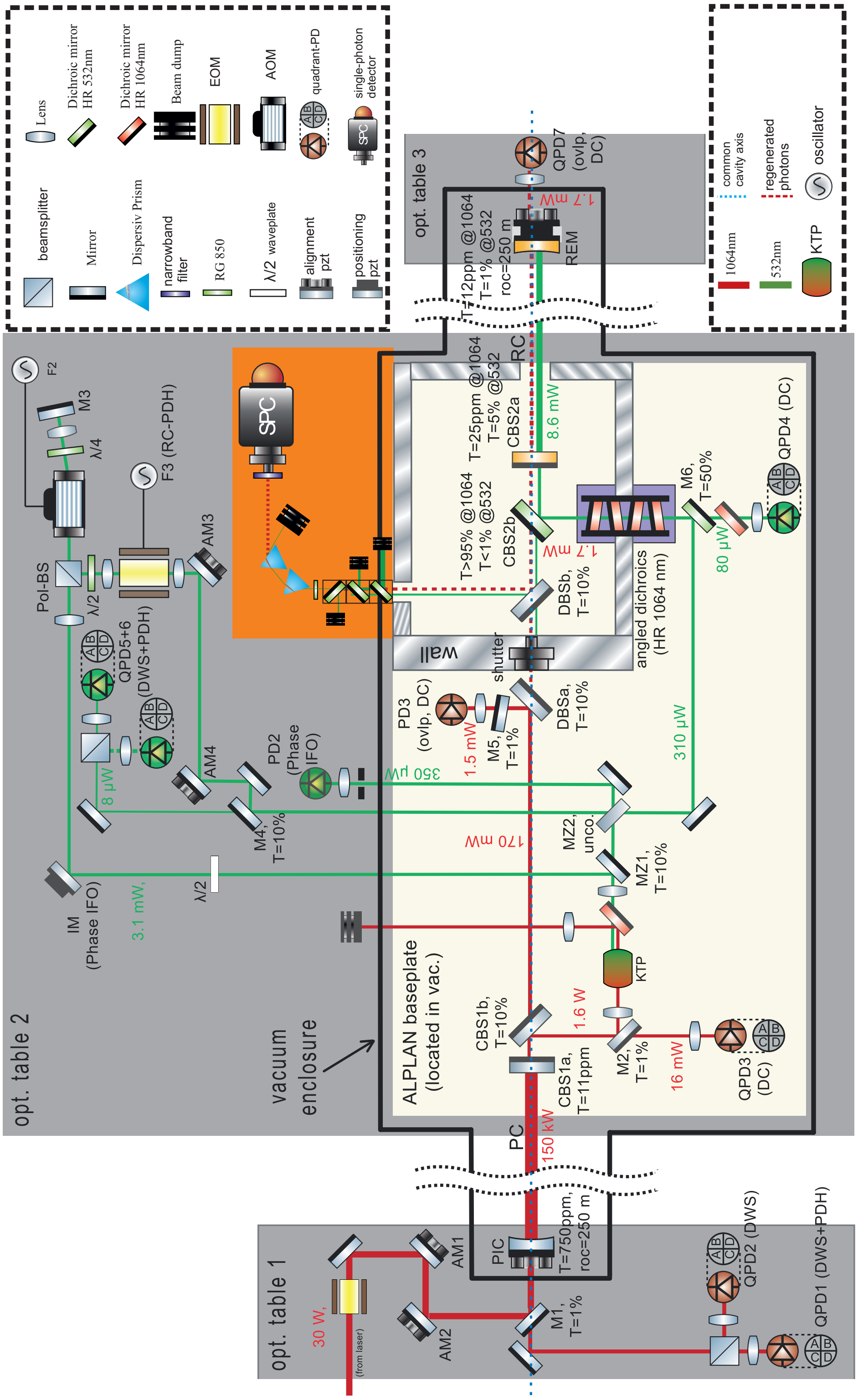

Figure 4.4: Optical scheme of ALPS-IIc [43]. Description in text.

position accuracy will also be discussed in the next section. How to mount the mirrors (either by gluing, bonding [85] or clamping) and with which procedure we can establish and control the common optical axis of these mirrors before fixing them are aims of the ALPS-IIa setup that is currently being worked on in Hanover. 90% of the light transmitted through CBS1a will be reflected by CBS1b onto the mirror M2 which has the same transmissivity as M1. The light transmitted through M2 is being detected on QPD3. Thereby we can calibrate the spatial position of the optical axis of the PC and fix the axis for the light transmitted thorough the PC. With this control scheme all degrees of freedom of the PC are fixed with the respect to the CB [43]. This means that the PIC will follow the movements of CBS1a.[2] About 1.5 W of the light transmitted by the cavity is reflected by M2 and send into a Kaliumtitanylphosphat (KTP) crystal which, via a SHG process, produces a beam at a wavelength of 532 nm [86]. The infrared and the green beam will be separated with a dichroic mirror directly behind the KTP crystal.

As mentioned earlier we have to note the different penetration depths of the two wavelengths into the cavity mirror coatings which leads to a tiny difference of the cavity length l for the green control light and the regenerated infrared light. This leads to a shift of the resonance peaks of the infrared and green light with respect to each other as depicted in Figure 4.5.

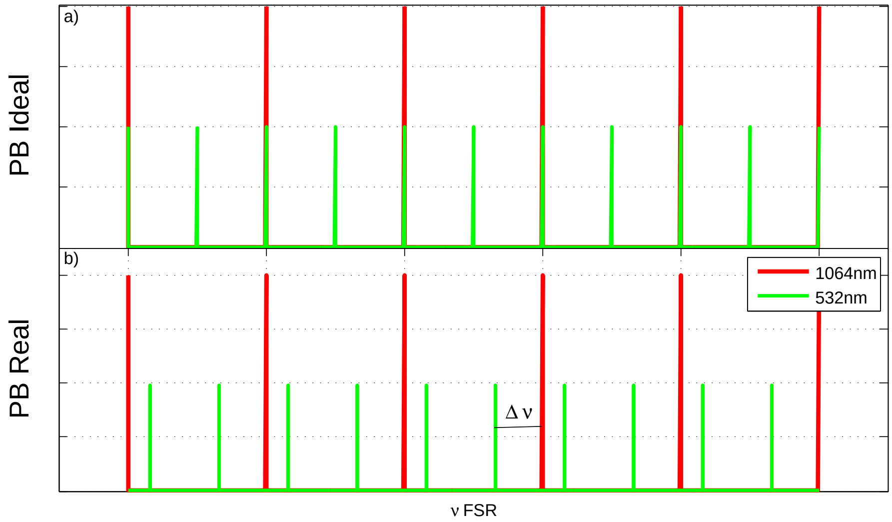

Figure 4.5: The mismatch between the green ν_{FSR} and the FSR of the infrared photons. Plotted are the PBs at resonance frequencies for both wavelength in an ideal and a real situation.

---

[2] A fixed connection between CBS1a and CB assumed.

As seen in figure 4.5, in the ideal case every second resonance for 532 nm light in a cavity also is resonant for 1064 nm light. However in reality the penetration depths into the mirrors are different for each wavelength. This variation can be corrected by shifting the green beam produced by the SHG with the help of an acousto-optic modulator (AOM) [87] to make the RC resonant again for the infrared light. To implement this, the green beam is being lead off the CB via MZ1. In chapter 2 we discussed reasons for operating most of the experiment in vacuum and concluded that the CB should be placed in the central vacuum chamber as shown in figure 4.4. Operating the AOM, which we use to shift the frequency of the green beam, in vacuum would impose unnecessary complications. Therefore the green beam is guided out of the vacuum before its frequency will be shifted by using the AOM in a double-pass configuration [88]. The frequency shifted light continues to an EOM which imposes the phase modulation sidebands needed for the PDH locking and DWS of the RC. The PZT mirrors AM3 and AM4 have the same function as AM1 and AM2 for the PC which is aligning the light onto the cavity axis of the RC. The green light is now guided back to the CB and can enter the regeneration area. However the frequency shifted green beam might be subject to phase fluctuations generated by the various optical elements and other disturbances on the long optical path. These fluctuations can also be caused by air turbulence or vibrations of optical components which are needed for frequency shifting and the alignment control of the RC. To detect the probably existing phase fluctuations the beam splitters MZ1 and MZ2 are creating a Mach-Zehnder interferometer [89] with a long arm which consists of the beam outside of the vacuum chamber and a short arm between the two beam splitters. The phase information is detected by PD2 and a correction signal sent to the PZT mirror IM. It is not planed to implement this control loop in Hanover but it will be part of the design that operates in Hamburg. In figure 4.4 there is an area separated by walls from the rest of the CB. This ”wall” is in fact a cylindric box, milled from one aluminum block to assure the light tightness, called the ”shutter box”. At the moment we test the light tightness of the connection of this box to the CB. The shutter box has, just like the wall in figure 4.4, four entry/exit ports which all have to be light tight for the infrared photons from the production region. The first one is the shutter which is placed in the common cavity axis of PC and RC. The second one is the entrance of the green control beam which is a light tight dichroic mirror holder that has the purpose to block the infrared light and simultaneously transmit the green control light to the RC. This connection is marked with a purple background in figure 4.4. The third port is the connection of the central vacuum chamber to the third lab which is the area of the RC and the forth one is the connection to the detector, where the regenerated infrared photons will be transmitted by CBS2a and guided via the attenuation box to the detector. This exit is marked with an orange background in the picture.

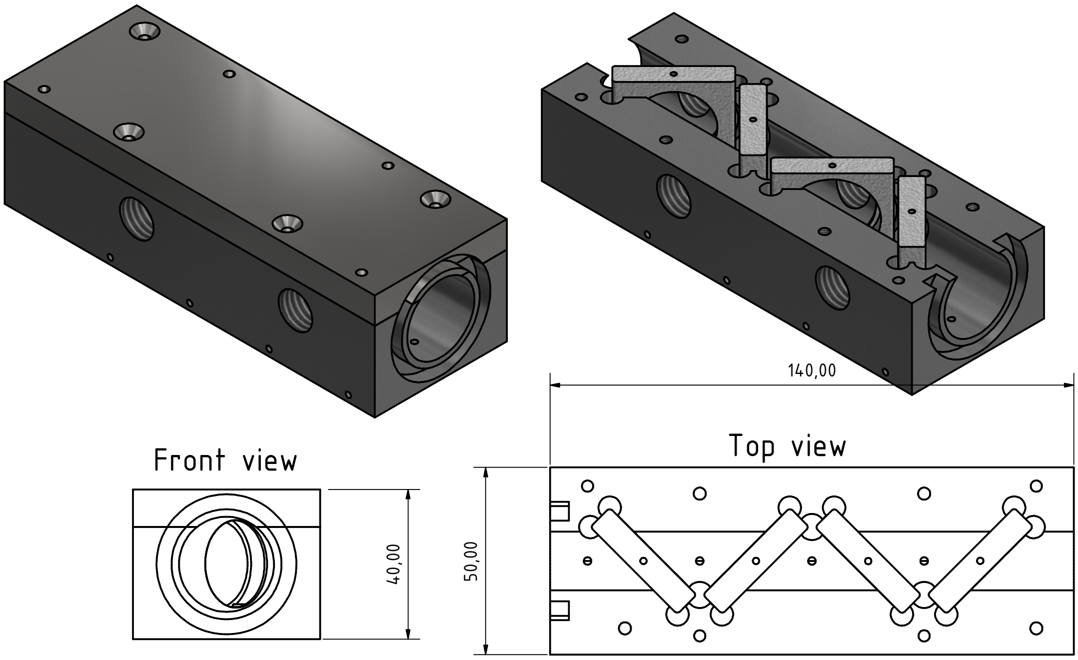

Figure 4.6: The design of the holder for the dichroic mirrors (the purple area in figure 4.4). The final light tightness of this device still has to be evaluated.

A CAD sketch and technical drawings of the purple marked connection (see figure 4.4) containing the dichroic mirrors are shown in figure 4.6. This mirror holder contains four dichroic mirrors of which all normal vectors of their surfaces are tilted by 45° with respect to the light-path. They are able to reflect the infrared light through additional ports into the area of the PC and transmit the green light to the RC area. With the help of aeration bores it is possible to place a mirror in a holder without accidentally creating air buckets which can hinder the pumping of the vacuum chamber.

After $\approx 155\,\mu\text{W}$ of the green light has entered the regeneration area it will be injected into the RC by the CBS2b mirror which is a dichroic mirror that is highly reflective (HR) for 532 nm photons and at the same time HT for infrared photons. The combination of the mirrors CBS2a and REM build the RC. These mirror create, as explained in 4.1.2, at the same time a high finesse cavity for infrared light and a low finesse cavity for the green light. The curved mirror REM has PZTs to align the axis of RC and also to control its length. The circulating green light will be coupled out of the RC through CBS2a and returns back on the path of the incoming green beam and will be detected by the QPDs 5 and 6 which have the same functions like QPDs 1 and 2. These photo diodes are being used for the detection of DWS and PDH errors signal that are required to control the alignment of the RC and its length with respect to 532 nm control beam. These control loops are currently in test phase in Hanover and will be described in [90].

With the setup described above we are able to lock both cavities separately but it is still not shown that they have the same optical axis. This in fact is the reason why we have to mount both flat mirrors CBS1a and CBS2a rigidly and completely parallel to each other on the CB. This constrain imposes requirements on the surface quality of the CB and the flatness of the mirrors which will be described in the next section. Assuming that the parallelism is given and both cavities are separately resonant for the infrared and green beams, one can open the shutter and let infrared light which is transmitted by the PC impinge on the RC. The resonant transmitted light from the PC has to pass through the mirrors CBS1b, DBSa and DBSb, each of with with 10% transmissivity for infrared and therefore 1,7 mW can arrive at the RC. By moving the PZT mirror REM we can now match the eigenmode of the RC with respect to the 1064 nm beam. While moving the REM it could happen that the length of the RC is not matched for green light anymore. This can again be corrected by shifting the frequency of the green light via the AOM. At the moment in which both lengths are resonant we can use QPD4 to mark the spatial position of the RC. A dichroic mirror in front of QPD4 prevents that disturbing infrared light reaches this photo diode. With QPDs 3 and 4 the references for the optical axes of the PC and the RC are being set. This makes it possible to set the RC eigenmode co-linear to the optical axis of the PC. To accomplish this, it is essential that both QPDs and the flat mirrors CBS1a and CBS2a can not move with respect to each other. If this is ensured than the RC will be resonant for infrared photons from the PC if it is resonant for the green photons. Hence it is also resonant to any light field regenerated from the WISP particles. The probably regenerated infrared light-field can be enhanced by a factor of $PB_{RC} = 40000$ and will be transmitted by CBS2a and CBS2b and guided via DBSb to the detection area which is marked orange in the picture.

4.2.2 Science run

Before starting a measurement run we are able to open the shutter and verify, by using the transmitted light of the PC, the resonance condition of the RC for infrared photons. As shown in figure 4.5 this condition is not always fulfilled. For the WISP search we, of course, close the shutter. Independent of the kind of detector we use (a silicon-based charge-coupled device (CCD) or a TES) and no matter if we guide the regenerated photons directly to the detector or focus it into a fiber first, we should avoid the arrival of the green photons at the detector. These photons could be interpreted as regenerated photons and thus falsify the measurement. To prevent this, a so called "attenuation unit" was planed, which will be described in detail in the next chapter. This unit utilizes a combination of dichroic mirrors and dispersive prisms and is located in the orange-marked area of figure 4.4.

4.2.3 The technical requirements for the central breadboard

As mentioned before, the central breadboard (CB) is a key component of the ALPS-II optical design [43]. The optical components which are mounted on this board have to be stable during the measurement. Therefore not only the mounting of the components is important but also the stability of the board itself. Since both flat mirrors of the cavities are mounted directly onto the CB, it has to be ensured that the external conditions are not changing the mechanical and geometrical properties of this board.

One important property is the thermal expansion coefficient (CTE) of the CB material. As explained before the circulating power in the PC is about 150 kW and the mirror CBS1a -which is directly connected to the surface of the CB has a transmissivity of 11 ppm which means that about 1,6 W are transmitted through this mirror. Because of the absorption properties of the coating and the substrate of CBS1a we should assume that a heating of this mirror occurs. Due the direct connection of the mirror and the CB we can also assume a spatially limited heating of the CB. Thus, a small CTE is important to avoid the deformation of the breadboard. Considering the mounting the components on the breadboard and the experiences gained while designing and operating gravitational wave detectors, [91, 92] zerodur, a glass-ceramic material [93] would be a good choice as the CB's material. However, since the flat mirrors of both cavities are mounted on this platform and the essential point is the light-tightness of the regeneration area for infrared photons, zerodur is not suitable for ALPS-II, as it has a high transmission coefficient for infrared light of ≈90%. The transmission curve of zerodur is shown in figure A.2. The disadvantage of zerodur for our purpose is its low thermal conductivity of $\kappa = 1.5\frac{\mathrm{W}}{\mathrm{m}\cdot\mathrm{K}}$. This means that the heat cannot be transported away on a useful timescale and the temperature of the contact point between the substrate and the CB can increase over the duration of the experiment. The other possibility is to chose a material which has a high thermal conductivity by which the heated area can be cooled just by distributing the heat over the whole material body. Aluminum is such a material with a high thermal conductivity but it suffers also from a higher value of CTE, compared to zerodur. Table 4.1 shows the thermal properties of these two materials [94].

Material	Zerodur	Aluminum
CTE	$5 \cdot 10^{-8} \frac{1}{\mathrm{K}}$	$2,3 \cdot 10^{-5} \frac{1}{\mathrm{K}}$
CTE inhomogeneity	$3 \cdot 10^{-9} \frac{1}{\mathrm{K}}$ over 40 cm	$< \cdot 10^{-7} \frac{1}{\mathrm{K}}$ over 40 cm
thermal conductivity κ	1,5 $\frac{\mathrm{W}}{\mathrm{m} \cdot \mathrm{K}}$	240 $\frac{\mathrm{W}}{\mathrm{m} \cdot \mathrm{K}}$

Table 4.1: Thermal properties of zerodur and aluminum. Zerodur has the lower CTE value while aluminum offers a higher thermal conductivity.

For the central breadboard material we decided to use a special aluminum alloy called ALPLAN which is an aluminum magnesium mangan (AI Mg4.5Mn0.7) mixture. This material is not only intrinsically harder than normal aluminum and therefore better resists deformation but is also specially rolled and cooled during the manufacturing process to achieve a high planarity in room temperature environment. The planarity which is required for the surface of the CB is depending on the requirements on the total angular beam shift between RC and PC. As mentioned before, the eigenmode of the regenerated light is the same as the eigenmode of the PC. Thus a high mode overlap between both cavities is needed to make sure that the regenerated light field is enhanced in the RC. The overlapp integrals for the eigenmodes of the ALPS-II cavities are calculated and described in detail in [3]. To achieve an overlap of $\approx 95\%$ between the eigenmodes of the ALPS-IIc cavities [43], the lateral shift of these two has to be smaller than 1 mm and the angular shift smaller than 10 μrad. The lateral shift requirements are easy to fulfill due to the large beam waist at the flat end mirrors of the cavities. However, the requirement for the angular tilt between the cavities below that mark is harder to achieve. The angular tilt requirement directly translates to a requirement on the surface of the ALPLAN and also the surface of the substrates of the both mirrors that connects them to the CB. It is also problematic to achieve this requirement by fixing the mirrors on the breadboard. During the construction of the LISA optical bench [95] there were bonding methods used to achieve similar requirements but bonding on aluminum is less favorable because the bottom surface of the substrate will be affected after the first bonding process so that in the event of a fault it will not be possible to place the substrate at the same place. Gluing is another alternative method that might work. At the moment it is planned to clamp the substrates on the CB. The flatness certified by the manufacturer of the substrates has yet to be checked and confirmed. Also the flatness of the CB is at the moment under our investigation.

For the ALPS-IIaHH, the flatness of the CB was not important as long as no RC was build. However, a CB was used in the ALPS-IIaHH setup to test its vibrational behavior in the lab and in the vacuum chamber which is the subject of the following section.

4.3 ALPS-IIaHH

As mentioned in section 2.3 the first step of ALPS-II is ALPS-IIa. This experiment itself is separated into two parts which are currently running in the ALPS laboratories in Hamburg and Hanover. The aims of these experiments are primarily to minimize the risks of future ALPS-II setups and to learn about the realization of the optical design described in last section. The section in Hanover is building a 1 m model of the RC and the PC to prove the consistency of the optical layout and the locking method with the second wavelength [90].

The other part of ALPS-IIa, that is simultaneously running in Hamburg, includes a high power test of the production cavity of ALPS-II with the length of approximately 10 m, which is a part of this thesis. Building the cavity in the new laboratories of the ALPS experiment allows us to examine several issues which are important for the final ALPS-II setup.

- Examination of the vibrational conditions in the new laboratories of ALPS-II. This knowledge is important for the physics run of ALPS-IIa (see section 2.3).
- We can also gain informations about the vibrational behavior in the HERA hall from the correlation measurements between the cavity and seismometers in our lab and seismometer measurements in the HERA tunnel.
- The conceptual design of mounting the CB onto the table and its vibrational damping can be tested.
- The influences of the environment on, primarily, the vibrational noise caused by the vacuum system and on the stability of the cavity can be tested.
- The properties of the mirrors and their coatings can be examined.
- Characterizing the production cavity and its properties like the transmitted power, the stability of control loops and characteristic of the mirrors.

With the existing cavity in Hamburg it is also possible to test potential designs for the light-tight area of the CB and also the light-tightness of the shutter (shown in picture 4.4) in a similar situation compared to the ALPS-II final setup. These steps are still ongoing and not part of this thesis. If the light-tightness of the connections is proven, a proper connecting between the regeneration area and the detector which could be a CCD camera as well as the TES detector[3] has to be

---

[3] Assuming that this is only reasonable if all components are ready and there is still work left to do in Hanover. Otherwise it is planned to build a RC in Hamburg.

established. However, it is shown that building the production cavity in Hamburg gives answers to many relevant questions of the final ALPS-II setup even without the regeneration cavity.

4.3.1 Optical design

The ALPS-IIa laboratories are located at DESY in building 50 on the -1st floor in room 607. These laboratories are consisting of three clean-rooms (CR1-3) and two gray-rooms. These rooms provide protection against contamination of the optical setup by dust particle. Especially PC cavity mirrors are, because of the high circulating power inside the PC, endangered. A particle that adheres on these mirrors can increase the mirror absorption and thereby damage the mirror. Although the RC will not have a high circulating power inside of it, a contamination of the RC mirrors changes the losses associated with these mirrors because of an increase of the absorption or/and additional scattering at the mirrors. One can argue with equation (3.38) that this would lead directly to a decrease of the power buildup of the RC. The gray-rooms are containing periphery devices of the experiment. The three clean rooms are used for:

- **CR1** contains the first optical table with the laser system for the experiment and the optical setup for the alignment of the PC. Furthermore the input curved mirror of the PC is placed in a vacuum chamber in this room.
- **CR2** contains the second optical table and the CB with the flat mirrors of the PC and the RC inside the central vacuum chamber. As described in the last chapter the components for frequency shifting the green beam and also the optics necessary for RC-PDH locking are placed in this room. In case a CCD camera is used as the detector it would also be placed in this room.
- **CR3** contains the third optical table with the curved mirror of the RC in a vacuum chamber which completes the vacuum system. In case ALPS-II uses the TES as the detector, it could be placed in this room (if a clean room environment is needed). A fiber could connect the TES with the output of the RC (see figure 4.4 orange backgrounded area).

The optical tables are damped by passive damping elements from the company MÜPRO [96] for a better isolation of the environmental noise. The ALPS-IIaHH is using these laboratories already. Figure 4.7 shows room 607 and the segmentation of the clean rooms. As mentioned above the setup of the ALPS-IIaHH needs the first two clean rooms to assemble the production cavity.

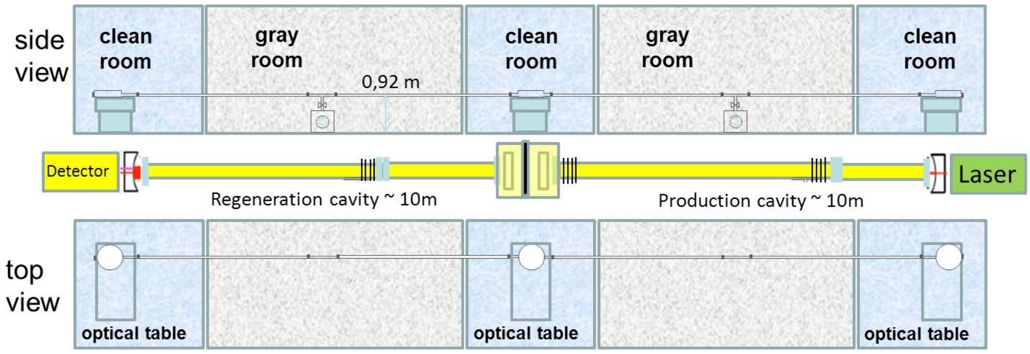

Figure 4.7: The scheme of the ALPS-II laboratories in building 50 at DESY. The top and side views of the lab and the path of the optical cavities are shown. One should note that the position of the detector can be in the second and third clean room or in second gray room. Picture is taken from [43].

Laser source

As the laser source we use the already in the ALPS-I [1] experiment employed laser system. The Master-Oscillator-Power-Amplifier system (MOPA) is a narrow band laser system operating at 1064 nm. The laser is provided by the company neoLASE. This laser system is described in [97] and developed for gravitational wave detection experiments like GEO 600 [98], the 10 m AEI prototype [99] and Advanced LIGO [100].

The enormous advantage of this system compared to most 1064 nm systems is the stable narrow linewidth emission which is essential for the enhancement of the laser power inside the production cavity. This emission is provided by a NPRO [101]. The spectral linewidth of the NPRO is in the order of 100 Hz within a measurement interval of 25 ms [102] and therefore far smaller than the linewidth of the cavity that will be described later in this chapter. The NPRO is furthermore frequency stable with a long term stability of 1 $^{MHz}/_{min}$ [3]. The NPRO is acting as the master laser in the MOPA system, therefore the frequency of the NPRO is the dominating frequency of the system. With this master laser the MOPA system can provide an output power of $\approx$ 33 W of narrow band 1064 nm light. The MOPA system contains elements to control its frequency. For our purpose the most important element is the PZT which was already mentioned in section 3.4 and is being used for the PDH frequency stabilization. The PZT is installed on the laser crystal of the NPRO and makes it possible to shift the frequency by applying mechanical pressure on the crystal. The shift can reach up to ±120 MHz with a response bandwidth ranging from 0 to ≈100 KHz [3]. In principal the NPRO allows also for compensation of slow frequency shifts by controlling the temperature of the crystal with a tuning coefficient of -3 $^{GHz}/_{K}$[97]. However, this possibility was not used in our experiments. The MOPA system contains an EOM and an AOM. The EOM is used for phase-modulating the light, which is needed for the PDH locking and the AOM offers the possibility of amplitude-modulation of the laser light. Therefore the emitted light from the master laser passes through these two devices before being amplified to 33 W.

The Cavity

In contrast to ALPS-IIc where the free available aperture inside the HERA magnets is the crucial factor (see section 4.1.3), this does not apply as a limitation for ALPS-IIa. However, due of the cost-considerations we decided to use the mirrors that are designed for the final experiment (100 m cavities) also in ALPS-IIa. The defined length[4] of the production cavity of ALPS-II HH is 9.30 m. With this length and the given ROC of 250 m for the curved mirror we can calculate the waist of the beam inside the cavity by transposing equation (4.6) to w_0

$$w_0^2 = \frac{\lambda}{\pi}\sqrt{L \cdot (R-L)} \qquad . \tag{4.8}$$

With a wavelength of λ=1064 nm we can calculate a beam waist of w_0=4 mm for the eigenmode of our cavity.

The free spectral range of the cavity can be calculated with equation (3.21) to be $\nu_F \approx 16.1$ MHz. Since we use the same mirrors as the ALPS-IIc PC, this cavity is also over-coupled and has the same finesse as calculated in section 4.1.2. With the same transmission and reflection coefficients of both mirrors of the PC the expected PB is 4900.

Here it should be noted that the curved end mirror originates from the same production-series as the one for the ALPS-IIc setup. In contrast, the flat mirror substrates are round and therefore not similar to those of ALPS-IIc. The reason for this difference is that in the current phase of ALPS-IIa there is no RC planned. Furthermore the technique for mounting the rectangular substrates which are essential for the mode overlap of the cavities (see section 4.2) is currently tested in Hanover. The round mirror with the ROC= ∞ is clamped in a mirror holder which is mounted on the central breadboard. Due to a different length and therefore a different FSR of this cavity, compared to the PC discussed in 4.1.2, the full

---

[4] This length is depending on the position of both mirrors inside the vacuum chambers. If needed, the length can be changed.

width half maximum is also different. The FWHM for the cavity of ALPS-IIa can be calculated with equation 3.35 to be $\nu_{FWHM} \approx 1{,}95\,\mathrm{kHz}$.

To Summarize, we can say that the planned cavity of ALPS-IIaHH is designed to have the same power buildup and finesse as the final version of the ALPS-II experiment. However, its geometrical behavior is different from ALPS-IIc. It is shorter and thus it has larger FWHM and FSR. Compared to the final version of ALPS-IIa it differs because of the flat cavity mirror. Below I will briefly describe the optical setup of the experiment and name it's important components.

Setup

After the light has passed through the modulation devices and is amplified to 33 W, it leaves the laser box of MOPA with a beam waist of 250 µm at the output facet and a waist diameter of ≈ 660 µm after a distance of 13 cm (see figure 4.8).

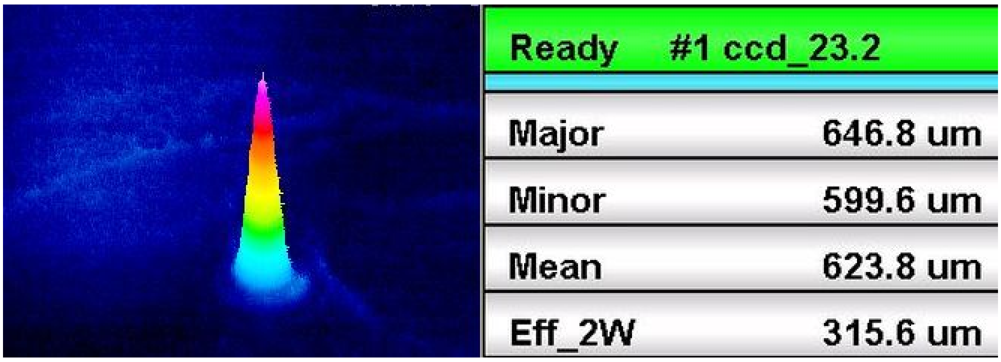
Ready #1 ccd_23.2
Major 646.8 um
Minor 599.6 um
Mean 623.8 um
Eff_2W 315.6 um

Figure 4.8: The waist of the laser mode. Measured in 13 cm distance from the output port of the laser.

The output beam passes through a λ/2 plate and polarization beam splitter which form an attenuation unit for the beam that is directed towards the experiment. Thereafter the laser light passes through a Faraday isolator. The isolator blocks back reflections originating from the subsequent optical setup. Based on the beam size at the output port of laser, our desired beam waist of 4 mm at the flat end mirror of the cavity, the cavity length of 9.30 m and the optical path length from the output port of the laser to the curved mirror of 2.70 m we can calculate the mode matching of the production cavity. Figure 4.9 shows the optical layout of the ALPS-IIaHH experiment which is currently existing in Hamburg.

Because the desired beam radius behind the last lens (f=300 mm) is bigger than 4 mm it is recommendable to chose the last three mirrors, that are being used for the lateral alignment of the laser beam into the cavity, with two inch

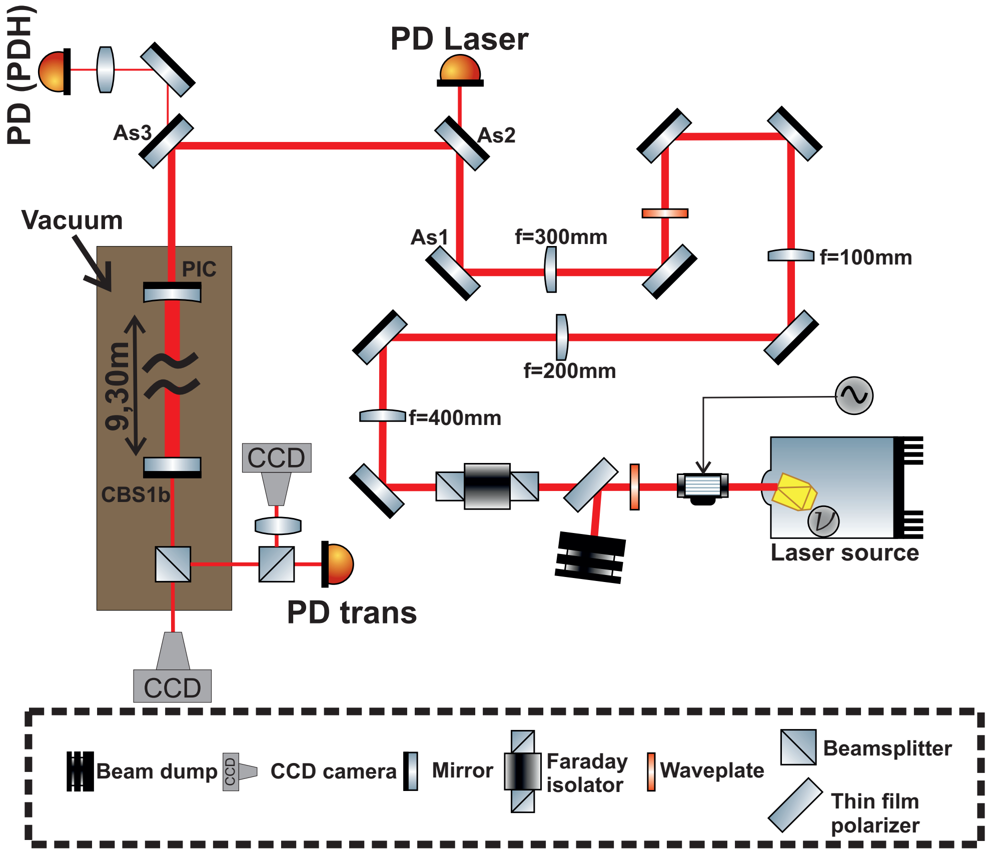

Figure 4.9: Optical layout of the experiment in Hamburg. Inside the MOPA, which serves as the laser source, modulation elements are housed. With two CCD cameras behind the cavity we can observe the resonant cavity eigenmode spatially and control their movement.

diameter to have more space for "beam walking". The mirrors of the cavity PIC and CBS1b are mounted in vacuum-compatible mirror holders. For the purpose of adjusting the cavity eigenmode we use pico-motors, mounted on the holder, that are also vacuum-compatible. They are of the type 8321-V sold by Newport. With these motors we are able to adjust the mirrors with respect to each other. A part of the reflected light form the cavity is transmitted by the alignment mirror AS3 and be detected by the Pound-Drever-Hall photo diode to control the laser PZT as explained in section 3.4. With the setup described above it is possible to lock a cavity with a length of nearly 10 m between the two first optical tables of the ALPS-IIa setup. Despite of these cavity specific properties like finesse and power buildup, we can also measure environmental influences on the cavity which are important for the general concept of ALPS-II. These measurements are shown below where we will also discuss their impact on the rest of the experiment.

4.4 Production cavity characterization

The production cavity was set up during this thesis as the first step of the ALPS-IIa experiment. In this section the results of the cavity characterization is presented.

4.4.1 Control loop characterization

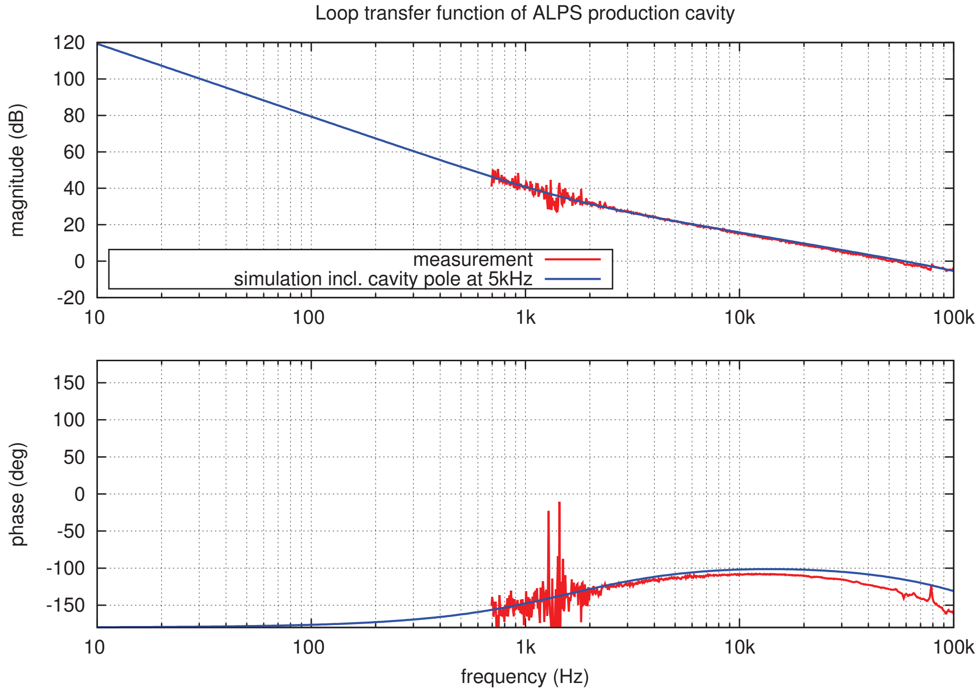

Figure 4.10: Measured transfer function of the production cavity control loop which stabilizes the laser frequency to the resonance frequency of the PC (red line) and a LISO simulation of the transfer function.

It was not necessary to design new electronics to employ the Pound Drever hall locking scheme on the ALPS-IIa production cavity as we were able to use the existing electronics which were originally built for ALPS-I. The PDH scheme is described in section 3.4.2. Figure 3.8 shows the components of the feedback control loop.

The utilized control loop can be separated into two main parts. The electronics and the cavity which provides the frequency reference for the PDH scheme. Figure 4.10 shows the measured loop transfer function of the PC (red line), compared with a simulation of the control loop, done with the inear Simulation and Optimization of analog electronic circuits (LISO) [103] (blue line). The unity gain frequency (UGF)[5] of the currently used ALPS-IIaHH control loop is 50 kHz with a phase margin of 70 degrees. The first goal of the control loop which is the realization of a stable lock is achieved. The second important point is the suppression of the dominant noise source to a sufficient level.

As it will be shown in section 4.4.3, the largest noise we have to compensate for is the seismic or vibrational noise because of the cavity length and the positioning of both cavity mirrors on two separate optical tables (see figure 4.7). To sufficiently attenuate this noise, that follows a $1/f^2$ dependency for frequencies above 10 Hz [104], two integrators are employed in the controller below 1 kHz. The required $1/f$ attenuation above 1 kHz is provided by the cavity pole that is described in the next section. For the LISO simulation, a cavity pole of 5 kHz is assumed. The simulation fits very well with the measurement until a frequency of 10 kHz is reached.

With this control loop a continuous lock for more than one hour was achieved. Currently the possibility of a long term observation of the cavity look is not given. Later we will discuss a 540 s observation of the cavity with different input powers. The control loop provides a gain of 120 dB at 10 Hz.

4.4.2 Pole frequency measurements

A reliable way to calculate the FWHM for this kind of cavity is the measurement of its cutoff-or pole frequency. The advantage of this measurement is the observation of the circulating light, independent from the mode matching and alignment. For this measurement the laser output is sinusoidally power-modulated with an AOM shown in figure 4.9. The result is a power fluctuation of the laser light which is then measured in front of the cavity with a photodiode (PD Laser in figure 4.9). The power noise of the cavity transmission is measured with a second photodiode behind the cavity (PD Trans in figure 4.9). The transfer function between this two photodiode signals is measured. An attenuation of 3 dB of the transmitted power determines the cavity pole frequency. Figure 4.11 shows the measured pole frequency of the PC cavity (also called the cavity pole).

Repetitive measurements showed that the cavity pole is varying between 4 kHz and 7 kHz. This variation of the cavity pole is currently not understood. A reason could be the phase shift of the reflected cavity signal and the mixing signal for the PDH scheme. However such a phase shift would be stable and thus the cavity pole

---

[5] The UGF defines the bandwidth of the feedback control loop since it does not provide feedback at higher frequencies.

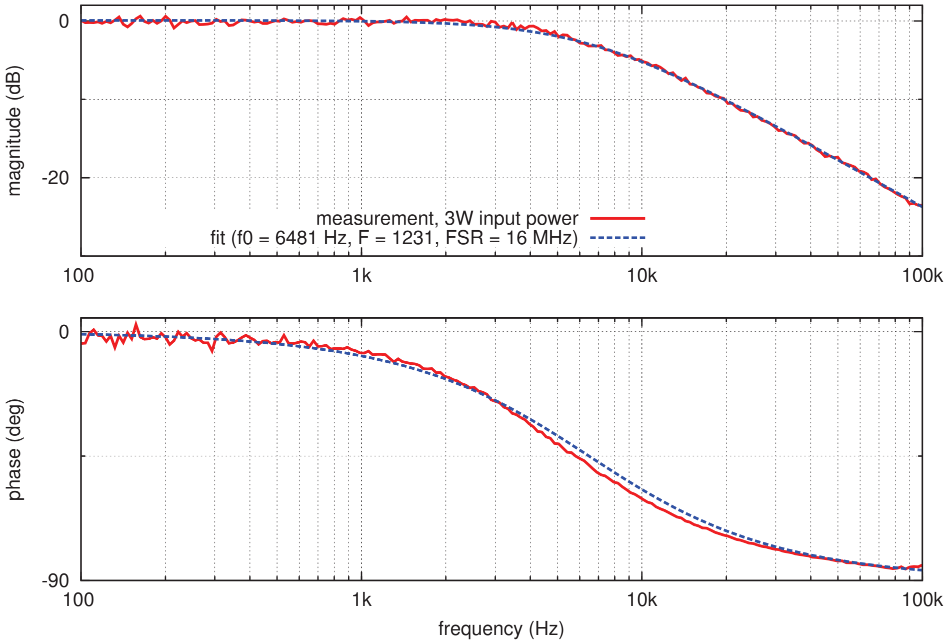

Figure 4.11: Exemplary measurement and fit of the PC pole. The pole is at ≈ 6.5 kHz. These measurements were repeated several times. Thereby the pole was shifted between 4 kHz and 7 kHz

would differ from the expected value but also be the same for each measurement. There is currently no explanation why the phase of the transmitted light should not be constant. The second problem of the ALPS-IIaHH cavity is the calculated FWHM of the PC. The relation between the FWHM of the cavity and its pole frequency f_p is given by [105]

$$\nu_{FWHM} = 2f_p \qquad . \tag{4.9}$$

This leads to a ν_{FWHM} of 8-14 kHz which does not match with the design goal of 1.95 kHz, calculated in section 4.3.1. While the variation of the light inside the cavity pole frequency is not optimal, a too high pole frequency is a serious problem for our setup. A higher value leads to a smaller finesse factor and therefore to a smaller power build-up of the cavity. A smaller PB would have a direct impact on the general sensitivity of the ALPS-II experiment as is shown in equation (2.5).

There are several reasons that can lead to a smaller finesse as originally desired. From equation (3.36) we can see that a lower reflectivity of the cavity mirrors could be a reason for a decrease in finesse. However, that can not be the case because we were able to confirm the transmission values of 11 ppm and 750 ppm for the two

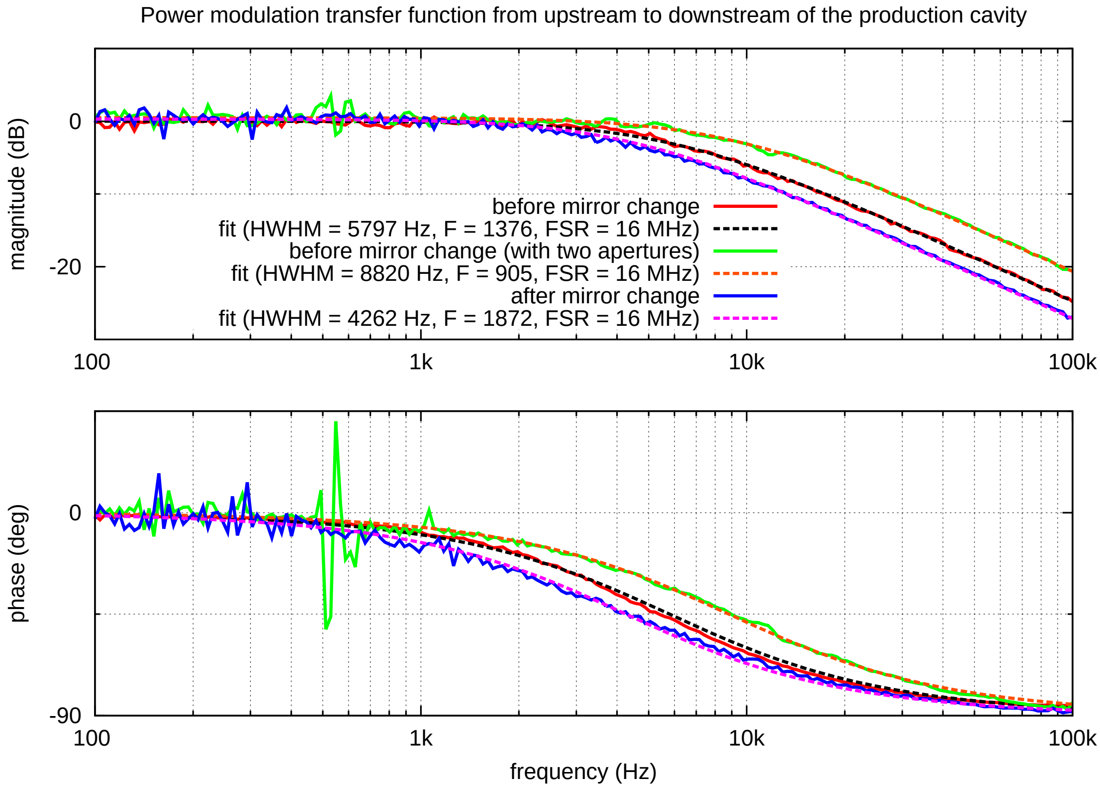

Figure 4.12: Cavity pole measurement for cleaned mirrors and added artificial apertures. The improvement of the pole frequency is not sufficient.

mirrors which were specified by the supplier. Equation (3.38) points to another possible problem: Additional losses could lead to the high pole frequency. Possible explanation for this losses are:

- **High absorption losses**
  The absorption losses of the mirror substrates could cause the low finesse. This assumption would be consistent with an observed decrease of the power, transmitted by the cavity, at high input power levels. The absorption could also be caused by the contamination of the surfaces of the mirrors. This contamination would also lead to scattering losses and also damage the coating of the mirrors irreversibly.

- **Scattering losses**
  A part of the losses could appear due to scattering. It was shown with the cavity pole measurements that replacing the cavity mirrors by new mirrors improves the cavity performance by a factor 2 (see figure 4.12). However the scattering losses of the mirrors due to the decontamination can be, at

most, only a part of the total losses. The reason behind this assumptions is the investigation of the former mirrors with a high-intensity fiber light source. This investigation shows minor scattering sources on the surface of the mirrors. Most of these sources were dust particle which could be cleaned. However the scattering losses caused by micro-roughness of the substrate are not visible with that light source.

- **Aperture**
  A small aperture would lead to clipping losses of the cavity and decrease the power buildup factor. At the moment there are no hints that the aperture of our vacuum tubes can cause such a problem as they have a diameter of 100 mm. However, a coating of the mirrors that does not fully extend to their edges would cause additional clipping losses.

Figure 4.12 shows different cavity pole measurement with the aim to determine the loss channels. The red curve shows a pole measurement with the same mirror-conditions as in the measurement shown in figure 4.11 with a pole at 5.8 kHz. The green curve shows a measurement with two 1” apertures installed inside the cavity and ≈5 cm away from the cavity mirrors. These artificial apertures shifted the pole frequency to 8.8 kHz. The best results were achieved by exchanging both cavity mirrors with new mirrors. This change accomplished the best measured result during this thesis with a stable cavity pole at 4.2 kHz. This indicates that the contamination losses were, at least partially, accountable for the high cavity pole. These losses on the old mirror surfaces can explain the different pole frequency values. Aligning the cavity axis before conducting a new measurement can lead to slightly different laser beam positions on the mirror surface compared to the previous measurement. We also intentionally changed the position of the eigenmode on the mirror surface to check the influence of non-equally distributed contaminations on the cavity pole. Thereby each time heating different spots on the mirrors surface. If the surface is not completely clean there would be different scattering losses due to different amounts of e.g. dust particles. With new dust free mirrors, a stable measurement of the pole frequency was achieved. In comparison it is likely that a fraction of the losses arose from scattering and absorption due to contaminations on the old mirrors. Unfortunately the pole frequency of 4.2 kHz is still a factor of 4 too high compared to the design goal after exchanging the mirrors.

With the measured pole frequency and by using equation 4.9 we can calculate the FWHM of the produced cavity to be 8.4 kHz. The FSR of the ALPS-IIa cavity is $\nu_F \approx 16.1\,\mathrm{MHz}$ (see section 4.3.1). With these values we can calculate the current finesse of the cavity with equation (3.35) to be $\mathcal{F} \approx 1900$. As shown above, the desired finesse value is 8020. To determine the magnitude of the unknown losses we extend equation 3.36 with a term A for the losses:

$$\mathcal{F} = \frac{\pi\sqrt{r_1 r_2 \alpha}}{1 - r_1 r_2 \alpha} \qquad \text{with} \qquad \alpha = \sqrt{1-A} \qquad . \tag{4.10}$$

With the given reflectivity of both mirrors, excess losses of ≈3400 ppm can be calculated. This value is far too high to be caused only by absorption and scattering losses and does not match with the specifications provided by the manufacturer (see section 4.1.2). The low finesse cannot be accepted because the PB of the PC is an important factor contributing to the overall sensitivity of our experiment. With this value for the losses we can estimate the power build-up of the cavity using the equation 3.38 to be $PB_{PC} \approx 170$. The estimated power buildup matches the calculations based on the measured transmitted light and the circulating power in the cavity. With an input power of $P_{in} \approx 3.2\,\mathrm{W}$, the light transmitted by the cavity was measured with a S121C power meter from Thorlabs [106] to $P_{tr} = 6.3 \pm 0.6\,\mathrm{mW}$. This leads to an estimated power buildup factor of $PB_{PC} = 179 \pm 11$.

To find out more about the reason behind such high losses it is first of all necessary to be sure about the substrate quality of the used mirror. Currently, the loss-problem of the PC remains unsolved. Nevertheless the constructed cavity allow us to make further measurements of the environment which are very important for the final version of ALPS-IIa.

4.4.3 Cavity length noise

The length fluctuations of the cavity can be a problem for the locking procedure and for the goal to have less than 5% power fluctuation during the science run [43].

By looking at the control signal we can determine these noises. It is crucial to distinguish between the different noise sources. The most important information for our experiment are the environmental noises which are only partially under our control. Other noise sources are electronics noise of the photo diodes used for the measurements, quantum noise and the frequency noise of the laser system. It is also important to avoid self-induced noise sources like vibrational noise produced by the turbo pump, utilized for the vacuum system, or flow boxes which are needed to provide clean room conditions in the lab. Nevertheless the main challenge could be the environmental noise of the laboratory caused by DESY water pumps which are on the same floor as our laboratory. These pumps are also share the ground floor with our optical tables. This problem could be lower than expected. Suppose the floor movements are in phase for two points on the floor spaced by about 10 m, the cavity does not recognize this vibration due to the simultaneous movement of both optical tables in the same direction (and consequently the cavity mirrors). This effect means that the cavity is "blind" for these vibrational noises which I call coherent movement or coherent vibrations.

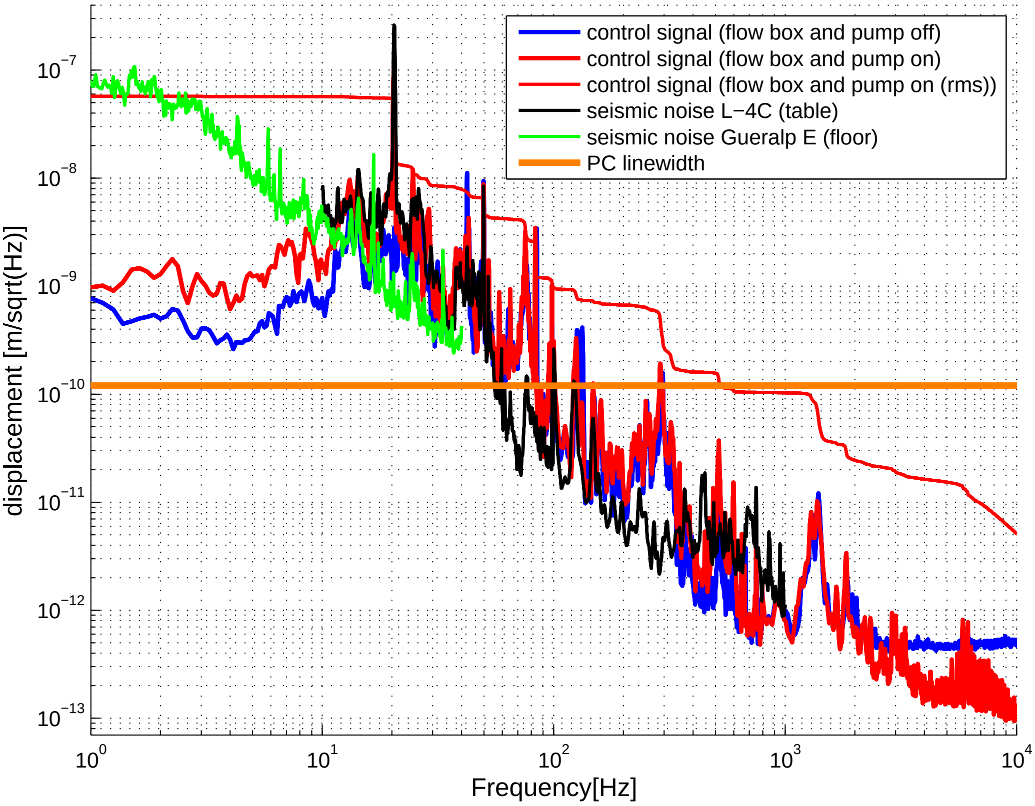

Figure 4.13: Compared length noise measurements with changing environmental conditions measured in vacuum. The vibration measurements provided by a seismometer (green) placed on the ground and a geophone placed on the central table (black) are independently calibrated. The production cavity linewidth is marked in orange.

The control signal of the control loop is measured at the HV output (see section 3.4). The measured voltage signal is calibrated to represent length noise and shown in Figure 4.13. To gain informations about the possible coherent vibration of the ground floor, vibrations are also measured with a L4C geophone which was placed on the first optical table. The L4C geophone is only calibrated for frequencies above 10 Hz. For measuring noises from 1-10 Hz we used the recorded data from a CMG-3TD seismometer from Guralp [107] provided by another DESY group. Figure 4.13 shows that from 10 Hz to 300 Hz the seismic noise is dominating the length noise spectrum. Below 10 Hz the seismic noise exceeds the length noise of the cavity. This shows that the vibration noise below 10 Hz is coherent and not an issue for the cavity. A comparison of the blue and red lines shows that there are still some undesirable couplings between the optical system and the flow boxes or the vacuum pump respectively. The 20 Hz peak is assumed to be caused by the flow boxes because it vanishes when the flow boxes are turned off. It should be possible to decouple these noises from the optical system. This means the blue curve can be seen as the length noise level of the ALPS-II PC. The saturation of the blue control signal above 3 kHz is currently not understood. Also the length noise caused by the seismic noise can be reduced with active or passive damping systems. Fortunately, the achieved noise level with use of passive damping elements under the optical tables is satisfying to reach a robust lock over time scales of one hour. This measurements were taken in vacuum. The measurements with a vented system show no major difference in the length noise spectrum.

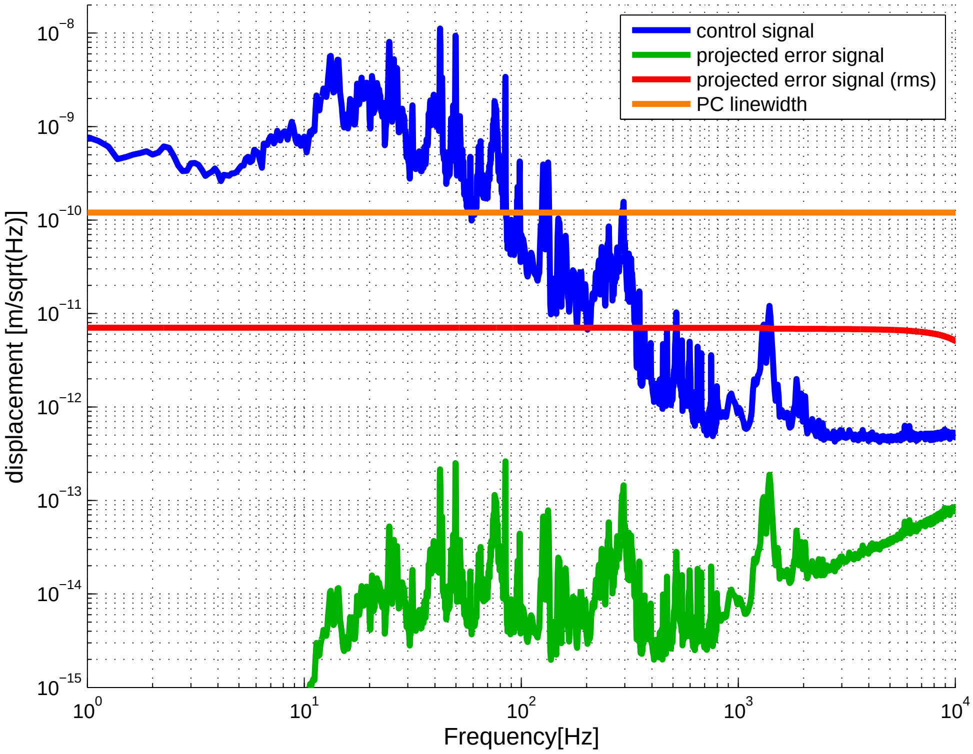

Figure 4.14: Comparison of the projected RMS of the error signal and the linewidth of the production cavity for the designed power builup of ≈5000.

Figure 4.14 shows the control signal (same curve as in Figure 4.13) and a projected error signal, which is the control signal divided by the loop gain of the control loop (see Figure 4.10). Unfortunately it was not possible to calibrate the measured error signal.[6] The RMS of the projected error signal is shown as a red line and the cavity linewidth as the orange line. As the RMS is about a factor of ten below the cavity linewidth, we can conclude that the laser frequency follows the resonance frequency of the cavity.

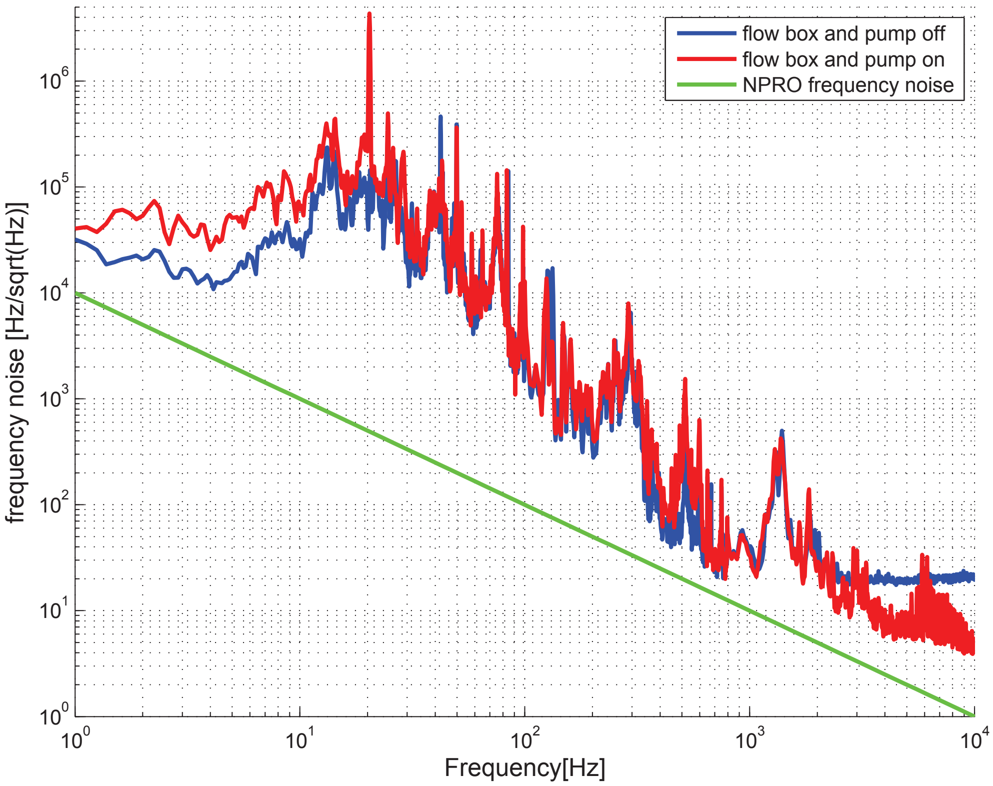

Figure 4.15: Measured vibration noise of the ALPS-IIa production cavity for active flow boxes and inactive flow boxes compared with the typical frequency noise of the used NPRO (green line) taken from [108].

Figure 4.15 shows the control signal calibrated to represent frequency noise. It can be seen that the noise caused by the seismic vibrations is larger than the frequency noise of a typical NPRO laser. The frequency noise of the NPRO can be approximated to be $10\,{}^{\mathrm{kHz}}\!/\!_{f}$ [108]. The high peak at 2 kHz caused no significant jump of the RMS value shown in Figure 4.13. Figure 4.15 also shows that at 1 kHz the vibrational noise is almost as low as the noise of the laser source.

---

[6] Ring down effects and seismic noise contaminate the error signal while scanning the length of the cavity. Calibrating the error signal by injecting of a signal at a frequency higher than the UGF did not work due to instabilities of the control loop and lock losses.

4.4.4 Power noise

Another important aspect of the PC is the power-stability of the transmitted light. This light will be used to generate the green light needed for the locking of the RC (see section 4.2). Too high noise levels will lead to a high power fluctuation of the green light and thus couple into the RC. Despite the fact that the finesse is lower than desired (see section 4.4.2) we are able to measure the power noise of the transmitted light to evaluate its stability.

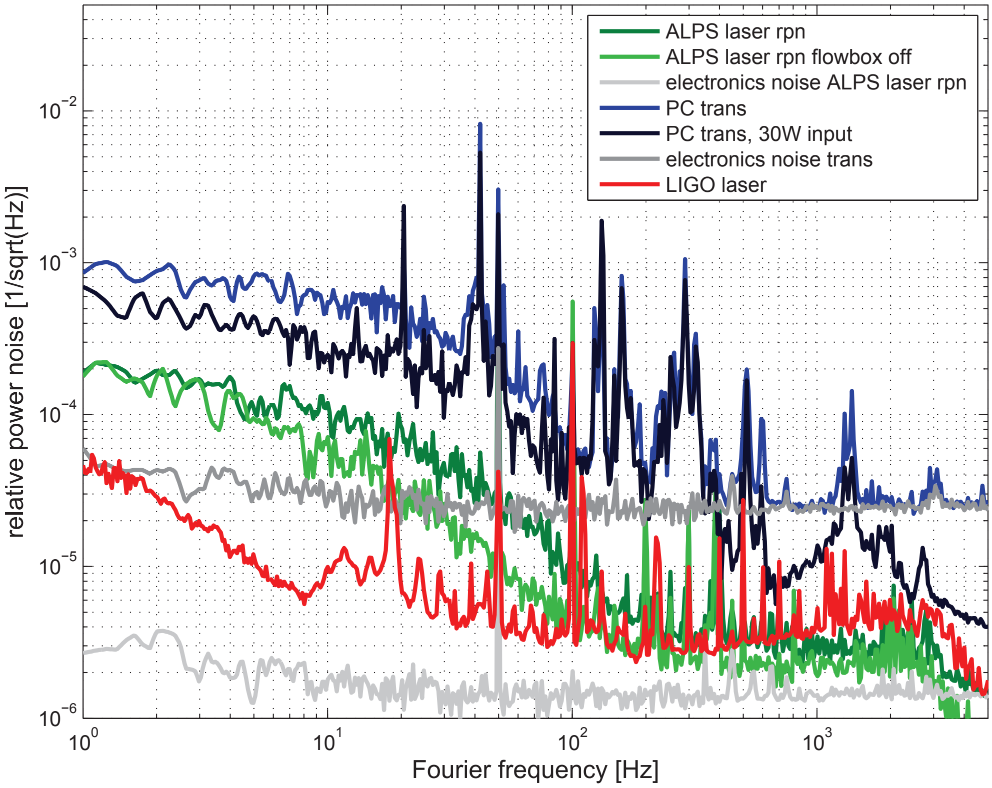

Figure 4.16: Relative power noise measurement of the ALPS-II laser and the transmitted light of the production cavity for two different input powers. The power noise of an NPRO as it is being used by the LIGO collaboration is also shown.

Figure 4.16 shows the relative power noise of the input beam and the transmitted light from the PC. These signals are measured with PD trans and PD laser respectively (see Figure 4.9). The relative power noise (rpn) is the measured spectral density $\delta \mathrm{P}(f)$ divided by the measured average power $\bar{\mathrm{P}}$ [109]. In the case of our measurements $\bar{\mathrm{P}}$ is the measured DC signal of the used photo diodes. Grey lines in figure 4.16 show the electronic noise of the photo diodes used in the measurement. The green lines show the power noise of the laser source which is placed on the first optical table. A comparison of the power noises of laser with and without working flow boxes shows that there is a slight influence from the flow boxes on the laser power noise ranging from 10 Hz to 200 Hz. A mechanical connection between the frame which holds the flow boxes and the optical table via the laboratory ground can also be a cause of this problem. At low frequencies the power noise of the ALPS laser is higher than the LIGO laser. The difference can be, once again, attributed to the air current in our lab, which LIGO does not suffer from due to the better acoustic enclosure. Another problem could be inhomogeneities of the photo diode across its active area. The transmitted light of the cavity shows a broad band increased noise level compared to the laser power noise. The blue line shows the measured transmitted power noise with an input power of $P_{in} \approx 4\,\mathrm{W}$. This measurement was repeated with $P_{in} \approx 30\,\mathrm{W}$ to achieve a better signal to noise ratio. The main reason for the higher power fluctuations could be alignment fluctuations of mirrors placed on the optical table shown in figure 4.9. These fluctuations are then converted to power fluctuations of the transmitted light of the cavity. Additional fluctuations could be caused by the beam splitters which lead the beam to the PD trans. Especially the first beam splitter, which is mounted inside the vacuum chamber and therefore out of reach for later alignments, can cause additional noise due to clipping combined with pointing of the cavity eigenmode relative to it. Since it is difficult to mount optical elements on the CB with ordinary clamps clipping could not be avoided at the time.[7]

---

[7] As explained in section 4.2.3 it is planned to fix the optical elements directly on the CB without using additional mechanical mounts. For ALPS-IIaHH we had to use ordinary mounts. Also gluing was not an option because there was only one CB available which was used to mount different optical components onto it. Because the CB was designed for the alternative mounting method, the hight of the CB was not optimized for ALPS-IIaHH.

4.4.5 Noise coherence

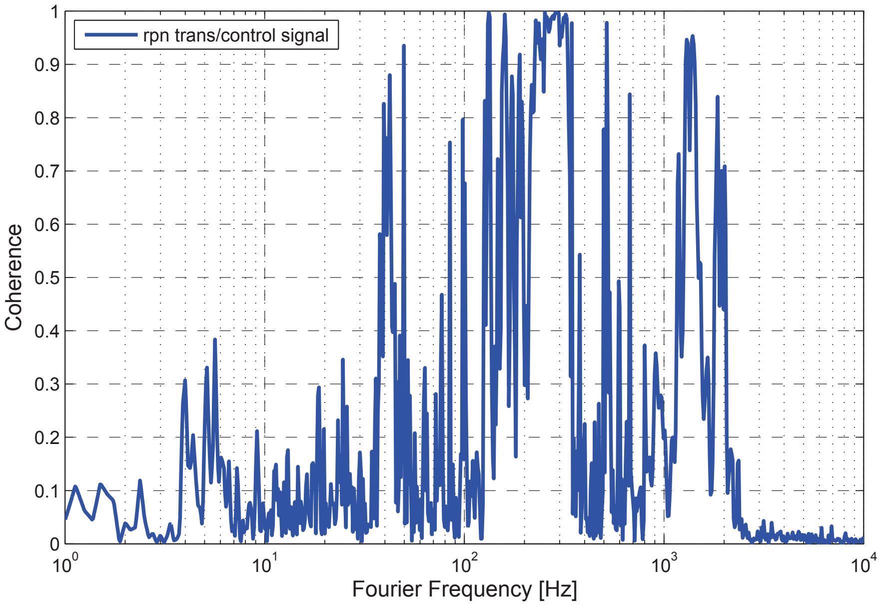

Figure 4.17: Coherence between the control signal representing the sensed length noise of the cavity and the power noise in transmission of the cavity.

To improve the overall stability of future ALPS-IIa experiments it is useful to learn as much about the noise sources as possible even though they might be, at this stage, sufficiently suppressed by the control loop. Figure 4.17 shows the coherence between the relative power noise of the light transmitted by the cavity and the control signal of the PDH control loop. A coherence of one at a given frequency therefore implies the same noise source in both signals. A strong coherence at 40 Hz is visible. This coherence could be the first harmonic of the vibrational noise caused by the flow boxes at 20 Hz (see Figure 4.13). From 100 Hz to 400 Hz the coherence is also almost always over 80%. These coherences can be explained with the seismic noise which is assumed to be the same in all directions. This seismic noise caused the alignment fluctuations that are leading to the power fluctuations of the transmitted light at the same time this noise causes the length noise in the cavity. Above 2 kHz no coherence between the signals is measured. This effect is not completely understood. An explanation can be that the frequency noise of the cavity above 2 kHz is near the Laser frequency noise and not caused by vibration noise. To proof how far these two signals are influenced by seismic noise, the correlation of each signal with the signal measured by the geophone is determined.

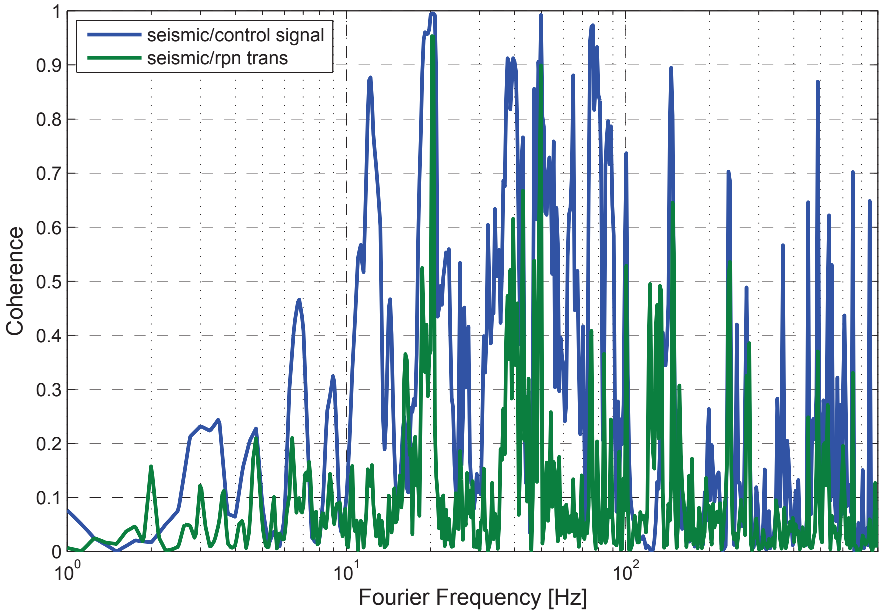

Figure 4.18: Comparison of the coherence of the seismic noise with the cavity control signal (blue) and the power noise in transmission of the cavity (green). In both cases the flow boxes were turned on. This is important as we assume that part of the vibrational noise is caused by the flow boxes.

Figure 4.18 shows the coherence between seismic noise and control signal in blue and seismic noise and transmitted power noise in green respectively. The coherence of the control signal and the seismic noise is stronger than the coherence of the control signal and the transmitted power noise. This can be explained by seismic movements collinear to the cavities optical axis which are suppressed by the control loop and thus not influence the transmitted power noise. The peaks which are observed in figure 4.13 at 20 Hz, 40 Hz and 90 Hz are also visible in the coherence measurement. The coherence at 20 Hz in both signals is assumed to be caused by an unintended connection between the flowboxes Vibrational noise that couples via length noise to the control signal and via pointing noise to the power noise in transmission of the cavity should cause a large coherence in both measurements. However, it seems that this a not the case for a broad frequency band.

4.4.6 Cavity stability

A stable and robust lock of the production cavity is very important for the stability of the regeneration cavity in all ALPS-II stages. Currently, a long term monitoring system for the ALPS-II experiment is under construction. Such a long term measurement was not necessary during this thesis since the main goal was the realization of a the PC.

Low input power

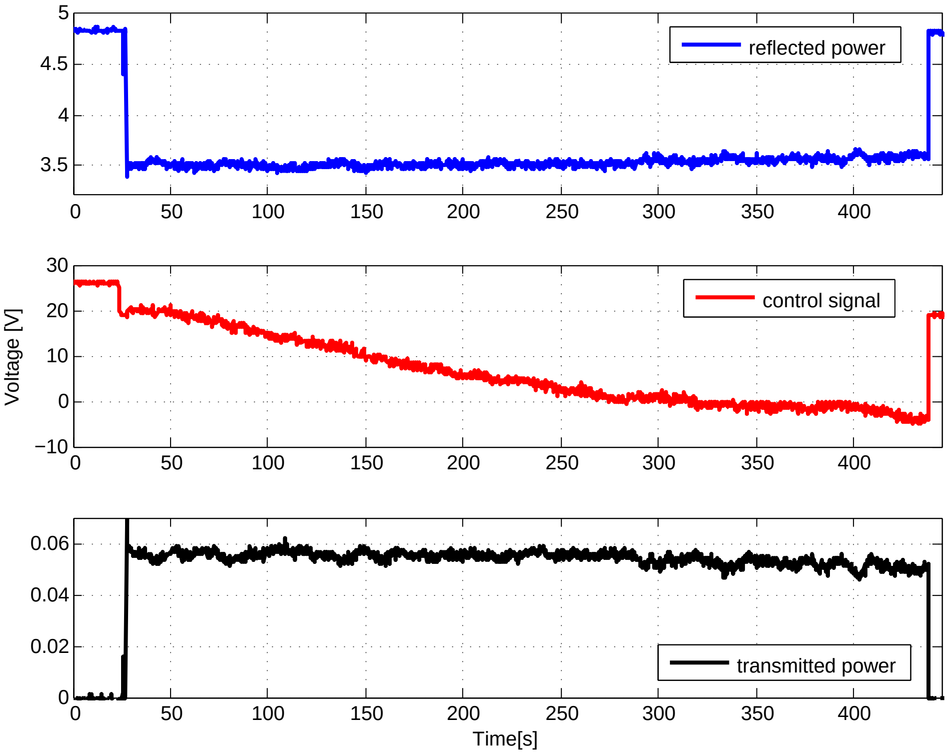

Figure 4.19: The transmission, reflection and control signal of the cavity. The cavity lock was broken on purpose at the end of the measurement.

Figure 4.19 shows the monitored transmission and reflection signals of the PC for a locking duration of about 400 s with an input power of $P_{in} = 3.2\,\mathrm{W}$. Also shown is the PZT signal for the laser source. As described in section 3.4.2 the PZT has a range of ±150 V. Figure 4.19 proofs that the control signal is non critical regarding the PZT range. The blue and black lines confirm that within the time period of 400 s the cavity transmission was stable. It should be noted that it was locked shortly after the measurements were started to display the reflected signal unlocked for calibration. At the end of the measurement the lock was broken on purpose. The PC stays locked for longer than 120 min in this configuration.

Variation of the input power

Despite the stable operation of the cavity at relatively low input powers it is important for the experimental aims of ALPS-II to proof that the cavity is also stable at high input power levels.

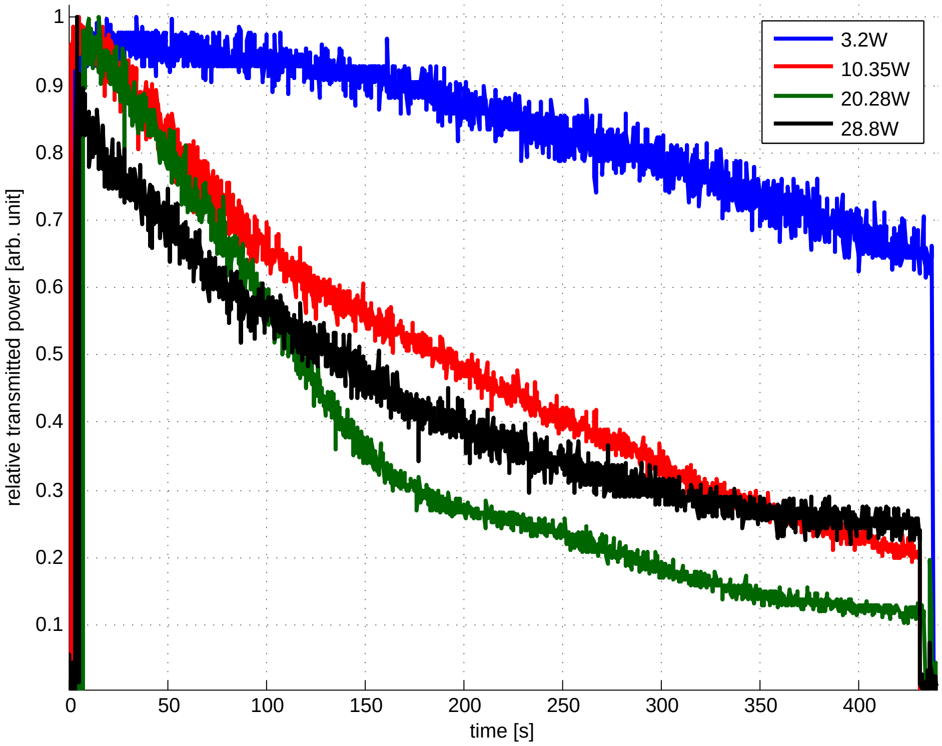

Figure 4.20: The cavity transmission signal at various input powers P_{in}. Despite the stability at all input power levels, the transmitted power decreases at high input powers.

Figure 4.20 shows the transmitted power levels with respect to a variation of the input power. The starting points of the red line and the green line should naturally not be at the same level but for the third measurement run with $P_{in} \approx 20\,\mathrm{W}$, we used a filter to prevent saturation of the photo diode (PD trans in figure 4.9). While the transmitted power is more or less stable for $P_{in} \approx 3\,\mathrm{W}$, it can bee seen that the power decreased over time with higher input power. A decrease of the transmitted power while the input power stays constant can only be explained by a decreasing performance of the PB during operation. This effect can be caused by two different hints. The absorption coefficients of the cavity mirrors could lead to heating and therefore expansion of the substrates and a change of the ROC due to thermal lensing. These effects are also observed for the mirrors of the arm cavities of the advanced LIGO interferometers[110]. This would lead to a change of the waist size of the cavity eigenmode and to a mode mismatch between the input beam and the eigenmode of the cavity. The consequences are that a smaller part of the input beam can be enhanced resonantly and thus the transmitted power decreases. The second option is a misaligning of the cavity eigenmode with respect to the input beam. This can be caused by heating of the mirror holders. In that case, the holders could change their position in transversal and angular direction. This leads to a change of the alignment to the cavity eigenmode which then leads to a lower overlap of the input beam and the cavity eigenmode. This effect also leads to a less circulating light and thus the transmitted power drops. Assuming that the calculated losses of ≈1700 ppm for each mirror (see equation 4.10) are caused by absorption of the substrates, and assuming an input power of P_{in}=29 W we can calculate a PB of 170 which in turn leads to an absorbed power of ≈8 W for each mirror. This assumption is only valid if we neglect scattering losses.

4.5 Conclusion

The construction of the ALPS-IIa production cavity was a major part of this work. At the end of my thesis the production cavity has been stabilized with a robust lock, working for more than two hours. The mirrors of the cavity are located inside the same vacuum system which will be used for the ALPS-IIa experiment. A modified central breadboard was placed inside of the vacuum system. On this board the flat mirror of the production cavity was mounted. The technical procedure with which this board is mounted into the vacuum system is the same in all ALPS-II stages. This setup gave the opportunity to investigate the vibrational noises, caused by the mechanical vibration of the vacuum system and their coupling to the CB. The results of these measurements are important for the use of the CB in both, this laboratory and the HERA tunnel. Furthermore vibrational noises of the environment of the new lab are investigated. This data is important for the first step of the ALPS-II experiment which will be done in these laboratories.

Although the production cavity is running very stable, the high circulating power performance which is anticipated for the ALPS-II experiment could not be reached. The finesse of the cavity is roughly a factor of four lower than the design goal resulting in a power buildup factor of ≈170 for the production cavity. The reasons of this ”low finesse” are currently not understood. Possible explanations are High absorption losses, scattering losses and a too small aperture. Due to the drawn-out fabrication process of the mirrors and, consequently, the deliverydelay, it was not possible to investigate these possibilities in more detail during this thesis. They have to be considered in the future. To address the findings of this thesis, the next steps of the ALPS-IIa experiment could be:

- The construction of the regeneration cavity despite the low finesse of the production cavity. In this work it was shown that the stabilization of the cavity is reliable. The same can be concluded for a regeneration cavity with the same length of approximately 10 m. This argument is only valid if the transmitted light is sufficient for producing enough green light via the SHG process.
- Simultaneous to the work on the RC, the flat mirror of the production cavity should be replaced by the recently delivered rectangular mirror to test the direct mounting of that mirror on the central breadboard. The alignment of both cavities with a common optical axis incorporating the new mirrors can be tested. The resulting stable production cavity should be characterized. This could give clues about the sources of losses of the cavity.
- To investigate the sources of the losses of the production cavity, it would be helpful to build two short cavities. These cavities should contain a curved mirror with well known losses and transmission. As the second and flat mirror, both mirrors of the production cavity can be used for these short cavities. One of them is of course flat, the other one has a ROC of 250 m. Fortunately, a ROC that large can be regarded as a flat for a cavity with a length of only a few cm (e.g.10 cm). With these two cavities we can characterize each PC mirror separately. Losses caused by the environment like the vacuum tubes of the PC can be excluded with these setups.

CHAPTER 5

Attenuation of 532 nm light

Considering the ALPS-II setup it is evident that a part of the green beam which is used to keep the RC aligned, can leak out in the same direction as the regenerated infrared light from the axion field, towards the detector. Therefore the green leakage light will also be co-linear with the regenerated infrared light. Usually the CCD-based detectors are incapable of distinguishing between wavelengths. They have only different quantum efficiencies for different wavelengths. For example the CCD-based PIXIS camera with a CCD47-10 sensor [111] which was used in the ALPS-I experiment [1] has a quantum efficiency of $\eta_{1064} \approx 1,21\%$ for 1064 nm photons [47] and $\eta_{532} \approx 95\%$ for 532 nm photons. The planned TES system for ALPS-II [29] is indeed able to distinguish between photons with different energies with a resolution of about 0,1 eV. However, a possible irradiation with green photons would generate a high count rate which will reduce the total sensitivity of the detection in ALPS-II. Therefore it is necessary to prevent the green photons from arriving at the detector. The easiest way to realize this, is to develop an attenuation unit which is able to block green photons while it is transparent for infrared photons. Such a unit could be build with using laser line filters like the "1064 nm MaxLine Filter" from Semrock [112]. Such filters are absorbing filters. However, absorbing the non desirable coherent photon flux comes not without disadvantages. If a monochromatic beam passes through an optical medium or if it is absorbed by that medium, it may lead to several effects, which result in the generation of photons with lower energies. We have to consider these frequency down conversion effects since we have to detect lower energetic photons with 1064 nm in the ALPS-II experiment as signal and attenuate the higher energetic 532 nm photons.

5.1 Conversion types

In general there are many parameters which influence down conversion effects, e.g. the intensity or the amplitude of the incident beam, the martial of the optical medium and possible nonlinear properties or the temperature dependence of the mediums optical properties. The down conversion effects cannot only be classified by their causes but also by their radiation spectrum or angular distribution. The goal of the experiments described in this chapter is to prevent the different kinds of down conversion effects. In the following some of the effects causing down conversion will be described.

A molecule with all its degrees of freedom is a well suited system to explain several possible decay paths of down conversion [113]:

- With non-radiative transitions. Here the excited state decays via internal transitions (rotational and vibrational) or collisions with the environment. Both eventually lead to heating effects of the environment [114].
- With radiation-less transitions from the singlet state to a triplet state ($S \leftrightarrow T$). This process is called intersystem crossing (isc) and changes the spin of the electron [115]. From the triplet state the system can decay to either a lower triplet state or the singlet ground state. Those decays are radiative.
- The molecule can either directly decay to the ground state or non-radiatively relax to a lower rotational or vibrational state and than decay to the ground state by emitting a photon with a defined wavelength.

5.1.1 Fluorescence

The third option is called fluorescence and is one of oldest known types of down conversion. It was first described by G.G. Stokes in 1852 [116]. If an atom is in a low energetic electronic state, for example the ground state, it can be exited by absorbing light which leads to raising the energy state from S_g to a higher, exited and instable quantum state S_e.

$$S_g + h\nu_i \rightarrow S_e \qquad ,$$

where h is the Planck constant and ν_i is the frequency of the irradiating light. If the atom decays back to the ground state possibly via several decay paths it will emit radiation with the same (resonant fluorescence) or a lower frequency. This process is called fluorescence. The emitted photon ν_{em} has the same or a lower energy than the irradiating photon ν_i.

$$S_1 \rightarrow S_0 + h\nu_{em} + E_{th} \qquad \text{with} \quad \nu_{em} \leq \nu_i \quad \text{and} \quad E_{th} \geq 0 \qquad ,$$

where E_{th} is the thermal energy. The fluorescence lifetime describes the average time between the excitation of the molecule and its returning to the ground state. It is typically near 10^{-9} s [113]. The intensity of the fluorescence light is depends on the fluorescence quantum yield Φ_F [117] and the intensity of the absorbed light with $\Phi_F = I_F/I_i$. Here, I_i and I_F are the intensities of the irradiating and emitted light. Thus the intensity of the fluorescence light from a system, for example an optical element is proportional to the intensity of on the irradiating light.

5.1.2 Phosphorescence

If the excited molecule is in a singlet state and undergoes an intersystem crossing [115] and changes from this state to a triplet state, it can decay back to the ground state by a second non radiative step (internal conversion) or by emitting light from the triplet state [118]. The radiative change from the triplet to the ground state is called phosphorescence:

$$S_1 \rightarrow T_1 \rightarrow S_0 + h\nu_{em} \qquad ,$$

where T_1 is an excited triplet state. The decay from the T_1 to S_0 is electronically forbidden and therefore much slower than the $S_1 \rightarrow S_0$ decay by the fluorescence [119]. The lifetime of phosphorescence is typically much longer than that of fluorescence and between 10^{-3} s and 1 s [113]. Much longer lifetimes are also possible. So called "glow-in-the-dark" toys [120] for example radiate for several minutes due to the slow return of excited molecules.

The phosphorescences quantum yield Φ_P is the product of two factors: The number of excited electrons that undergo an isc from S_1 to T_1 and the number of electrons which relax from T_1 to the ground state via phosphorescence [121]:

$$\Phi_P = \left(\frac{k_{isc}}{k_F + k_{nr}} \right) \cdot \left(\frac{k_P}{k_p + k'_{nr}} \right) = \frac{I_P}{I_i} \qquad ,$$

where k_{isc} is the number of isc transitions, k_F is the number of fluorescence photons, k_P is the number of phosphorescence decays, k_{nr} and k'_{nr} are the number of non-radiative decays from S_1 and T_1 respectively. Figure 5.1 shows the diagram for a photoluminescence system with several decay paths. I_P is the total intensity of phosphorescence light. Similar to the case of fluorescence the intensity of phosphorescence is proportional to the total intensity of the irradiated light [122].

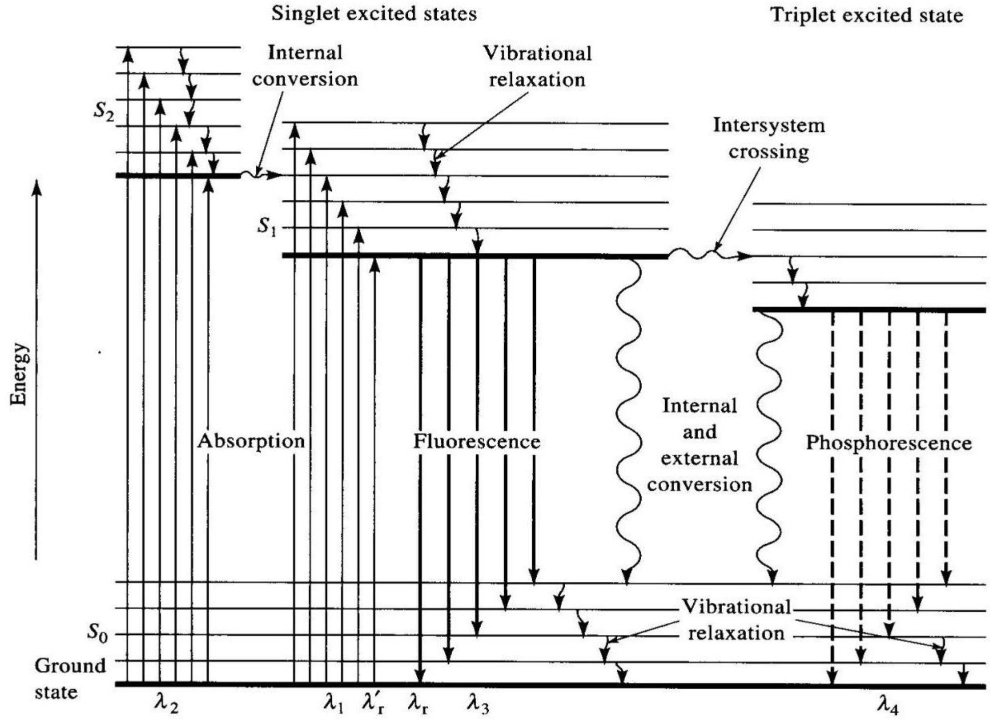

Figure 5.1: Different types of down conversion. The picture is taken from [121]

5.1.3 Spontaneous parametric down-conversion

Spontaneous parametric down-conversion (SPDC), is a second-order nonlinear optical process. It describes the spontaneous splitting of a high energetic pump photon (UV to VIS area) while passing an optical element, normally a nonlinear crystal, into two lower-frequency photons. We don't use nonlinear crystals for our setup but even conventional optical components like filters or prisms have small nonlinearities which can become relevant in a high precision, low photon-count experiment like ALPS-II. For better qualitative understanding of SPDC the following section will deal with the effects in nonlinear crystals. During this process the pump photon does not exchange its energy with the nonlinear crystal. SPDC can be considered as the inverse process of the more widely known up-conversion processes of sum-frequency generation (SFG), where two low energy photons are mixed nonlinearly to produce one high-energy photon [123].

Due to energy conservation, the sum of the energies of the two resulting photons is equal to the energy of the pump photon $\hbar\omega_p$. $\omega_p = \omega_1 + \omega_2$,where ω_1 and ω_2 are the frequencies of the two resulting photons. For historic reasons, the two produced photons are called signal (s) and idler (i) photons. The signal and idler photons are highly polarization-correlated and even entangled in energy and momentum [124]. The other conservation law that has to be fulfilled is momentum conservation [125].

$$\vec{k}_p = \vec{k}_1 + \vec{k}_2 \qquad \text{with} \qquad k_i = \frac{2\pi n}{\lambda_i} \qquad ,$$

where $\vec{k}$ is the wave vector and λ is the wave length of light and n is the refractive index of the medium for a defined wave length. The photon counting rate for the measured signal or idler beams is given as [126]:

$$\begin{aligned} I_s &= \alpha_s |\eta|^2 \langle I_i \rangle \\ I_{id} &= \alpha_{id} |\eta|^2 \langle I_i \rangle \qquad , \end{aligned}$$

where α is the quantum efficiency of the detector for signal and idler photons, $|\eta|^2$ is the down conversion efficiency and $\langle I_i \rangle$ is the average intensity of the pump light. The coincidence counting between the resulting signals is very similar to the single channel counting rate of signal and idler detectors [127]

$$I_{s,id} = \alpha_s \alpha_{id} |\eta|^2 \langle I_i \rangle \qquad .$$

For this work only the intensity of the SPDC photons, which are a source of a false positive signal for APLS-II, is relevant and not the precise parameters leading to their production.

There are also many other conversion mechanisms, like two photon emission (TPE) [128] or black body radiation, which could be problematic for the detection system of ALPS-II. Therefore it becomes necessary to construct an experiment with the aim of building the attenuation unit for preventing the green control beam from reaching the detector in which we eventually can seek out down conversion effects and prevent them.

5.2 Aims and requirements

The attenuation unit which was build has to be highly transmissive for 1064 nm signal photons. As the unit is the last optical element in front of the detector a lower transmissivity would directly diminish the total efficiency of ALPS-II. As explained in section 4.2.1, 155 µW of the SHG-produced 532 nm beam which is used to lock the RC will penetrate the regeneration area behind the wall through the dichroic unit which prevents entering of diffuse or directed 1064 nm light into the regeneration area (see also figure 4.4). The RC will have a power build up of approximately 60 for 532 nm light. This means that it will have about 155 μW·60 ≈ 9 mW of circulating green light. The transmitted light field from CBS2a which has a transmissivity of 5% interferes with the incoupling field so that approximately 85 μW leave the RC towards CBS2b. The green light will be reflected by the CBS2b mirror which has a transmissivity of 1% for 532 nm light. Thus no more than 1 μW of green light will propagate towards the detector. The main task of the attenuation unit is to prevent that this light reaches the detector.

As mentioned above different kinds of down conversion processes should be considered. The transmitted green light from the RC could produce light with lower energy by passing through CBS2a and CBS2b. The possibility that this diffuse light arrives at the detector can be prevented by designing an attenuation unit which is not only attenuating 532 nm but is also narrow band transmissive for 1064 nm photons. Generally down conversion effects could appear as well in CBS2a and CBS2b. This was not investigated since these mirrors were not available at the time of the experiment described here.

5.2.1 Magnitude of attenuation

The attenuation unit should prevent 1 μW of directed green light from arriving at the detector while not producing infrared light. To estimate the order of magnitude for the attenuation it is helpful to know which flux of green photons corresponds to 1 μW. With

$$E_{photon} = h \cdot c/\lambda \qquad \Rightarrow \qquad E_{532\mathrm{nm}} = 3.7 \cdot 10^{-19}\,\mathrm{J} \qquad ,$$

the number of photons RC_c heading towards the detector can be calculated:

$$1\,\mu\mathrm{W}_{532\mathrm{nm}} \mathrel{\hat{=}} 2.7 \cdot 10^{12}\,\frac{\mathrm{ph}}{\mathrm{s}} = RC_c \qquad .$$

h The dark count rate of the TES detector designated to ALPS-II is expected to be $1 \cdot 10^{-6}\frac{\mathrm{ph}}{\mathrm{s}}$ [43]. The attenuation should ideally decrease the number of green photons below this value. The required attenuation OD_D for the designed detector noise of ALPS-II (DC) can be calculated:

$$OD_D = \frac{DC}{RCc} \mathrel{\hat{=}} \frac{1 \cdot 10^{-6}}{2.7 \cdot 10^{12}} = 3.7 \cdot 10^{-19} \qquad .$$

This value is intended to be the design goal of the needed attenuation of the attenuation unit. The value of 3.7 $\cdot 10^{-19}$ for green photons is also only necessary if the TES detector reaches the dark rate of $1 \cdot 10^{-6}\frac{\mathrm{ph}}{\mathrm{s}}$. Eventually we can also distinguish between the photon energies which lowers these requirements.

5.2.2 High transmissivity for 1064 nm

The high transmissivity for 1064 nm photons is important and a transmittance above 90% should be set as a goal. This transmissivity has to be narrow banded to ensure that produced photons with wavelength $\lambda > 532\,\mathrm{nm}$, which are produced because of down conversion effects (like fluorescence etc.) inside the attenuation unit or the RC, cannot arrive at the detector. These photons would, if they arrive at the detector, increase its back ground rate. To summarize the requirements for the down conversion experiment, one can note the following three points:

- Attenuation of the 532 nm beam transmitted by the RC on the scale of $\approx 4 \cdot 10^{-19}$.
- High transmissivity for 1064 nm photons regenerated from an axion-like field.
- Investigating possible conversion effects of 532 nm photons and prevent the converted low energetic photons from arriving at detector.

5.3 Measuring with the SBIG camera

A ST-402ME camera from SBIG [129] was used as a detector. The SBIG camera is a CCD detector with a Kodak KAF-0402ME chip [130]. This camera has a high quantum efficiency $\approx 62\%$ for 532 nm photons and like most CCD detectors a very low quantum efficiency for 1064 nm photons $\approx 2\%$.[1] The dark count rate of this camera is $1\,\frac{\mathrm{ph}}{\mathrm{s}}$ pro pixel. Therefore the detector noise DC of the SBIG is three orders of magnitude higher than the PIXIS camera used in ALPS-I with the dark count rate of $1 \cdot 10^{-3}\frac{\mathrm{ph}}{\mathrm{s}}$ pro pixel. Despite this fact the SBIG camera was chosen for the attenuation experiment because it was already available and easy to handle. The PIXIS camera was at that time used to precisely investigate its quantum efficiency [47].

CCD cameras divide the amount of detected photons in so called analog to digital units (ADU). The ADUs are the fragmentation of the CCD between the lowest number of photons it can detect and the highest number of photons. Each CCD has an upper limit on electrons which it can hold in one pixel before it starts to leak into its other pixels. Images from this camera are 16-bit images. This means

---

[1] The company specified the QE of the KAF-0402ME chip only until 1000 nm. For 1000 nm the QE is $\approx 5\%$. However, similar chips to the KAF-0402ME like KAF-3200 [131] and KAF-1001 [132] which are also "Full Frame CCDs" [133] are specified for 1064 nm with a QE of $\approx$2%. Moreover, since we specify the attenuation in orders of magnitude it is not necessary to precisely determine the QE of the CCD.

that the camera can translate the number of electrons each pixel can detect into a brightness value between 0 and 65535. The gain factor is the amplification factor that the analog/digital converter needs to show the full fragmentation between 0 and saturation of each pixel. The camera has an analog/digital gain of

$$\text{gain}_{ST-402ME} = \frac{\text{Number of } e^{-} \text{ per pixel}}{\text{Number of ADUs per pixel}} = 1.5 \quad . \tag{5.1}$$

A full characterization of a CCD detector similar to the SBIG of this experiment can be found in [47]. In this section it will be briefly described what is important to note when working with the SBIG camera and how basic data taking for the down conversion experiment works.

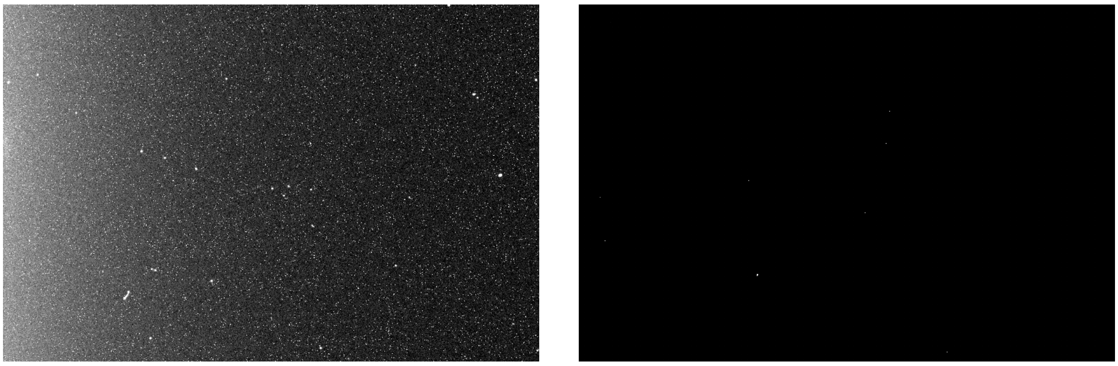
(a) (b)

Figure 5.2: (a) a typical dark frame of the camera. (b) a picture taken with an open camera shutter and switched off room light from which picture (a) was subtracted.

To analyze the recorded images it is always necessary to take so called ”dark frames” before exposing the camera to the real lighting conditions which is called taking a bright frame. Recording dark frames is important to estimate the impact of two different issues which can falsify the results if they are not considered.

- **Camera internal noise**
  Every CCD chip has a specific dark current noise. Its influence can be weakened if the CCD is working at lower temperatures. However, it is not possible to eliminate this effect entirely. By the readout and digitization of images from CCDs a second noise of the chip appears which is caused by the on-chip amplifier which processes the weak signals in the CCD. By recording a dark frame it is possible to eliminate the effects of dark current and read out glow because the build up of both noise contributions at a given

constant chip temperature and a defined exposure time is a repeatable effect. Recording a dark frame and a bright frame of equal exposure at the same ambient conditions and subtracting the dark frame from the second one the effects are removed. Figure 5.2 shows a typical dark frame of the camera.

- **Room background light**
  Even a room with very few light sources is not really dark for a highly sensitive camera like the SBIG. Due to the external influences in the laboratories, there was always a certain amount of back light remaining which disturbed the measurement. In Hanover the magnitude of this disturbing light was much larger than in the Hamburg laboratories, the latter being designed for these types of measurements. However it is possible to compensate for the back light influence by measuring the dark frame for as long as the measurement of the bright frame takes. It is very important to make sure that the lighting situation in the lab does not change while taking both frames.

To ensure that the mentioned effects are not disturbing the measurement, dark frames were recorded after every change in the experimental setup like modification of optical components, exposure times or lighting situations. Normally, in experiments that don't need to be quite as sensitive as ALPS-II, the dark frame used to compensate for the internal noise effects of the camera is recorded with a closed camera shutter. In our case the shutter of the camera probably does not provide the level of light-tightness required. Therefore the whole detection setup is placed in a box custum made for this setup to keep the light out. The design parameters of that box are being discussed in section 4.2.1. Another shutter, this time placed directly at the entrance port of the box, keeps the light out for the dark frame measurement. Therefore it is possible to estimate both the internal noises of camera and the back light in the laboratory.

5.4 Experimental setup

The general idea behind the down conversion experimental setup is as follows: There is an infrared test beam which defines a designated path from the entrance aperture of the attenuation box to the detector. This beam simulates the path of potentially regenerated photons towards the detector and transmitted from the RC. With the test beam the position where the infrared photons hit the CCD surface will be marked. A second beam with a wavelength of 532 nm which simulates the green RC controlling beam will be overlapped with the infrared test beam before entering the attenuation box. The overlapping of both beams makes sure that the green and red photons hit the same region of the CCD chip if there were no barrier for the green photons. During the measurement of the attenuation the infrared beam which was used to position the spot on the camera will be blocked such that only the green beam enters the attenuation box. Picture 5.3 shows this general idea.

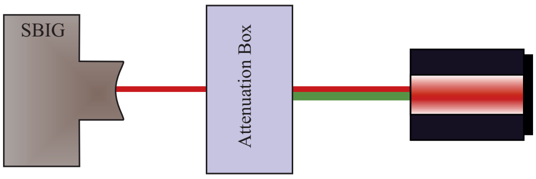

Figure 5.3: The general idea of the experiment. The probe beam marks the detection position on the CCD chip. The attenuation unit is highly transmissive for the probe beam and blocks the green beam.

Due to the renovation of the new ALPS laboratories in Hamburg, the attenuation experiment was divided in two phases. The first phase of the experiment took place at AEI in Hanover. In this step a general setup was designed and realized. With this setup initial knowledge could be gained which was helpful for the second and final setup. That second part with the final setup was build in the newly installed laboratories at DESY in Hamburg. Due to new knowledge about difficulties and how to overcome them, more than one setup was probed, in Hanover as well as in Hamburg. Due to different environments in both laboratories like the total possible length of the experiment and different back-light sources, it is useful to divide this chapter by the location of the experiment.

The goal of this experiment and all the other down conversion experiments was to see a dark screen by recording frames with the camera (recording frames is described in 5.3 and always refers to recording a bright frame and a compatible dark frame). It is considered a success, if this setup does not produce any photons with $E_{photon} \leq E_{532nm}$ which could arrive at the detector. Figure 5.3 shows the described setup. In the following section the setups which were important for the solving of the down conversion problem will be described chronologically.

5.4.1 Setup Hanover

For the experiment in Hannover an infrared neodymium yttrium aluminum garnet (ND:YAG) laser system with an output power of 9 W was at hand. The 1064 nm beam was frequency doubled to 532 nm with a SHG process in a nonlinear periodically poled potassium titanyl phosphate crystal (PPKTP) [3]. It was possible to achieve a coherent light beam with an output power of up to 5 W. The process of SHG is not the topic of this chapter and is briefly described in chapter 4. For the test beam a small part of the infrared beam was separated before entering the SHG crystal and guided directly to the box via a single mode fiber. Then the test beam and green beam were overlapped and entered the attenuation box.

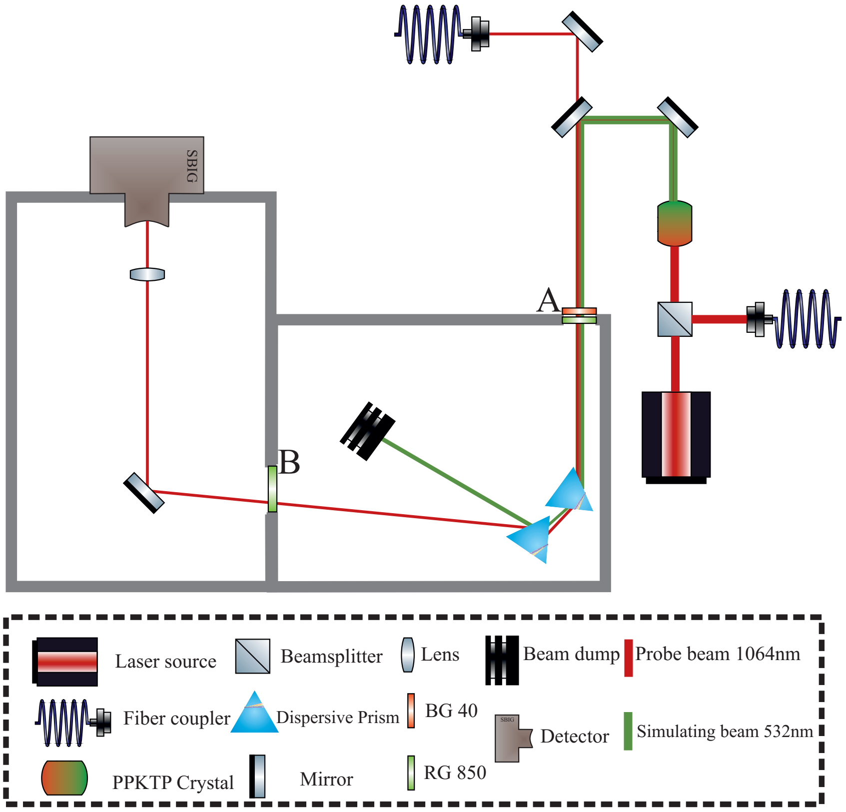

Figure 5.4: Scheme of the first setup in Hanover. The attenuation is in this scheme performed by dispersive prisms and absorbing filters. The probe beam is provided from the laser source via the optical fiber.

The components of the attenuation unit have been placed in a designed light tight ”attenuation box”. The primary purpose of this box was to accommodate all needed optical components for the down conversion experiment including the detector. In particular due to the back light in the lab in Hanover such a box was necessary. Depending on the spatial properties of the final ALPS-II setup the same box can be used as the final host of the attention unit and a connecting link between the optical setup and the detector setup.

The first setup consisted of dispersive prisms, broadband absorbing filters RG850 which weaken beams with wavelengths below 700 nm by five orders of magnitude (see Figure (A.1)) and BG40 absorbing filters which weaken beams with wavelengths above 700 nm by one to three orders of magnitude.This filter absorbs particularly the 1064 nm photons by two orders of magnitude (see Figure (A.1)). When entering the box, the main portion of the unwanted green beam will be filtered by absorbing RG850 filters in front of the box at position **A** in Figure 5.4. The dispersive prisms separate the paths of the overlapped green and infrared beams. These prisms guide the remaining green beam into a beam dump. A second set of RG850 filters at the position **B** blocks the stray light from the beam dump. The infrared test beam propagates to the CCD detector where it marks pixels relevant to the analysis. BG40 filters at the position **A** are needed to block the residual 1064 nm light from the frequency doubling process. These filters are being removed for the adjustment of the infrared test beam on the surface of the CCD chip and reinstated for the measurement. Picture 5.4 shows this setup.

For the first steps, the process of analyzing the recorded data was kept as simple as possible to save time and make the work on this part of the experiment more efficient: To reach the attenuation factor explained in section 5.2.1 it is necessary to record data for at least one hour. As long as the CCD detector shows saturated frames while the duration of illumination stays under one hour, a complete analysis concerning of number of photons is superfluous. In this case it is much more important to find and mitigate the source of the detected light.

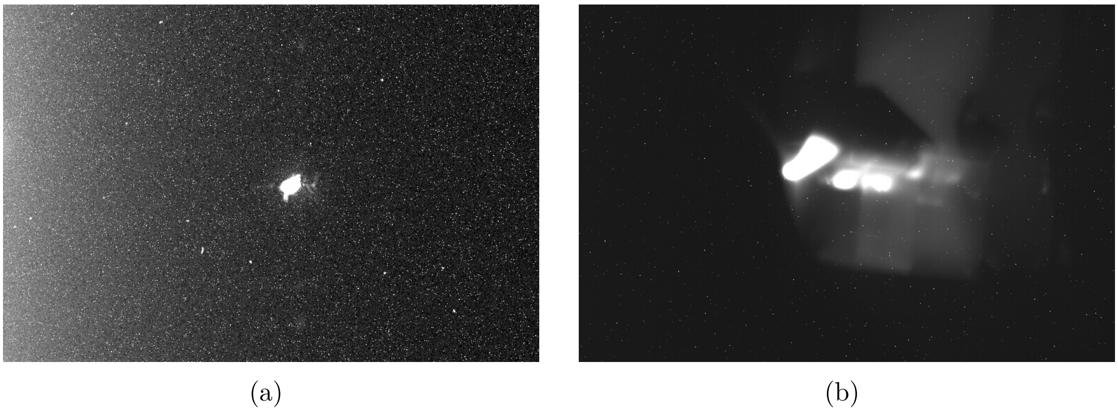
(a) (b)

Figure 5.5: First measurement with the setup illustrated in Figure 5.4. Picture (a) shows the probe beam and picture (b) shows this setup irradiated by green light.

This first setup illustrated the main problem of the experiment. Of all the possibilities discussed in section 5.1, the main source of converted photons which arrive at the detector is due to fluorescence (see section 5.1.1). Figure 5.5a shows a picture of 2 μW of the infrared probe beam which is guided by both dispersive prisms to the detector and detected with an exposure time of 10 min. It can be seen that the detector shows a spot as it would be expected for a laser beam. Figure 5.5b shows a picture taken with the same optical setup and exposure time but with 28 mW of green laser light with blocked infrared beam. It can be seen that picture of the green beam (Picture 5.5b) is different from the one of the probe beam, which doesn't show a directed beam but undirected and dispersed light. Of all the candidates of possible conversion processes discussed above, a florescences process is the one which explains this picture completely. The bright fragments which can be seen in Figure 5.5b are only visible as long the laser is irradiating towards the box. In the case of SPDC (see section 5.1.3) there are two defined wavelengths for idler and signal photons. In that case we expect two defined spots on the CCD surface. Fluorescence as the main reason for the detected light is the best explanation in this case. Moreover, the observed effect could be a mixture of SPDC effects and fluorescence or a very short life time type of phosphorescence. However, it is more important to identify components which cause down conversion effects than to determine the type of these effects.

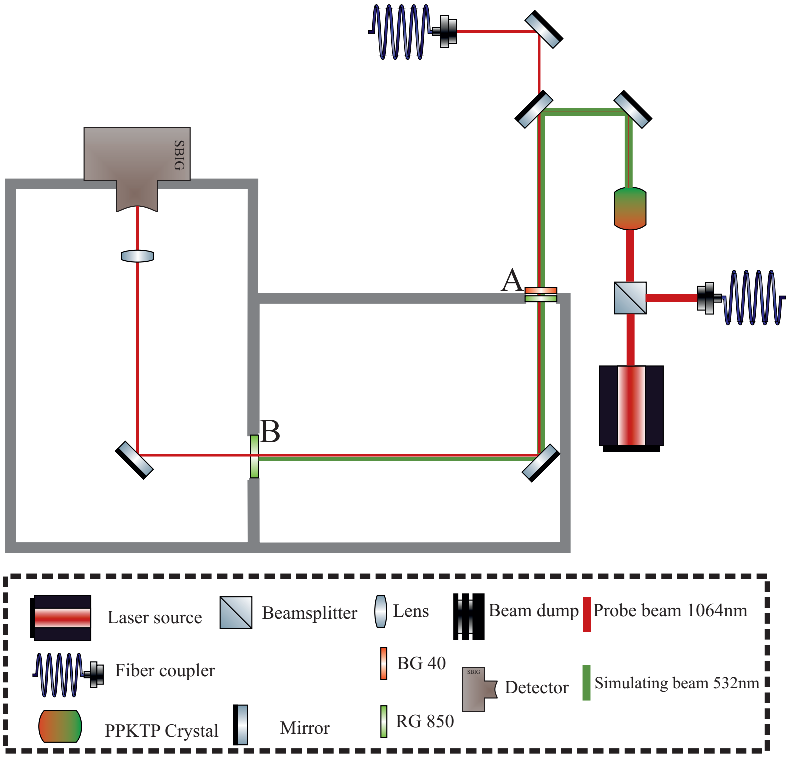

Figure 5.6: To distinguish between the filters and prisms as the source of the disturbing light, we used highly reflective mirror instead of dispersive prisms. The probe beam is provided from the laser source via an optical fiber.

To distinguish between the contributions of prisms and filters we replace both prisms with coated fused silica mirrors that are HR for 1064 nm in case of an angle of incidence of 45° and recorded frame with 5.3 mW of green light with an exposure time of 10 min. This setup is shown in Figure 5.6. Figure 5.7a shows that the disturbing light is still visible, only the pattern has changed. We now detect two half circles instead of the blurry pattern in the previous setup. The fact that the light is still present shows that a large part of this fluorescence light is most likely caused by absorption effects in the optical filters. The reason behind the pattern-change is the different type of light guidance in a prism and a mirror. The mirror reflects the light according to the law of specular reflection but a dispersive prism transmits the light depending on its wavelength into several angles. Taking into account that the fluorescence light is broadband and undirected, this results in a blurry pattern when using a prism. Since the HR mirror is optimized for 1064 nm other wavelengths can penetrate the substrate and will be reflected at the back. This effect causes the second circle in Figure 5.7a. To check this assumption we replace the HR coated mirror with an aluminum coated mirror in which the broadband light won't penetrate the surface. As can be seen in Figure (5.7b) the double-pattern vanishes and only one circle is visible. With this setup the fluorescing characteristics of the absorption filters is proven.

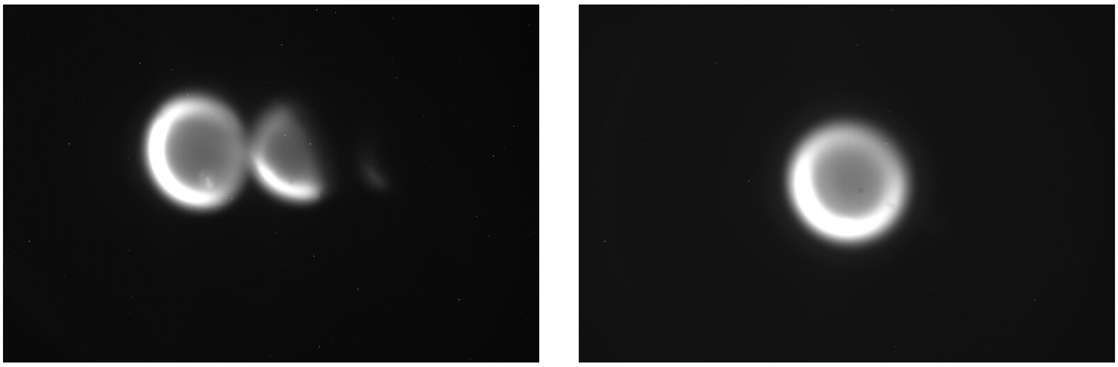

(a) (b)

Figure 5.7: Measurement after replacing the dispersive prisms with mirrors. Picture (a) was taken with an HR mirror instead of the prisms. In Picture (b) the HR mirror was replaced by an aluminum coated mirror.

Since the intensity of the fluorescence light is proportional to the incident light and the power used for this experiment is only 5.3 mW compared to 1 W in the final setup of these investigations, absorbing filters are not suited as components of the attenuation unit. With the setup described above it is only determined that the RG850 filters are exhibiting fluorescence but the influence of the prisms as the other dispersive optical components in the setup is not clarified. In a further step, the lens which is used to focus the beam on the camera was adjusted in a way that we were able to record a sharp image of the prisms.

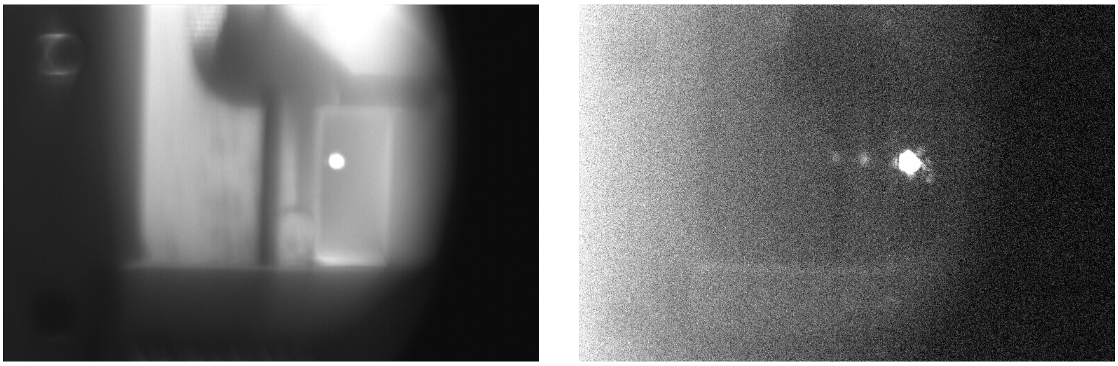

(a) (b)

Figure 5.8: Picture (a) shows the silhouette of the second prism and the position of the probe beam as shown in Figure 5.4. Picture (b) shows the same setup with less room light. For obtaining a sharper picture the contrast was increased digitally.

Figure 5.8a shows the image of the second prism in the setup which is shown in Figure 5.4 and the infrared probe beam which is transmitted through it. Before recording this image the RG850 filters were removed and the light tight box was opened enough for background to light enter and to illuminate the contours of the prism. The picture was recorded with an exposure time of 500 ms. As can be seen in this picture a clear spot is visible. The changes of the setup leading to the picture of Figure 5.8b are that the box is closed once again and that a RG850 filter was installed at position **B** (see Figure 5.4) right after the light has passed the prisms. Since the filters at position **A** exhibit fluorescence they were not present while taking both pictures. For the first picture this measure had no effect on the quality since the lab-background light was required to get an image of the prism. In case of the second picture this means that even with a closed box some background light can enter the system. Therefore the RG850 was installed at position **B** to filter out the remaining room-light. The residual light that can be seen in the second picture caused by using only one filter which does not filter out all room-light. In later setups more than one filter was used. The picture was also exposed for 500 ms. Because of the room-light the contour of the prism is weakly visible. The probe beam spot is clearly visible, the weaker spots around it are the reflections of the infrared light on the surfaces of the prisms. Figure 5.9 shows the schematic setup with which this pictures were taken.

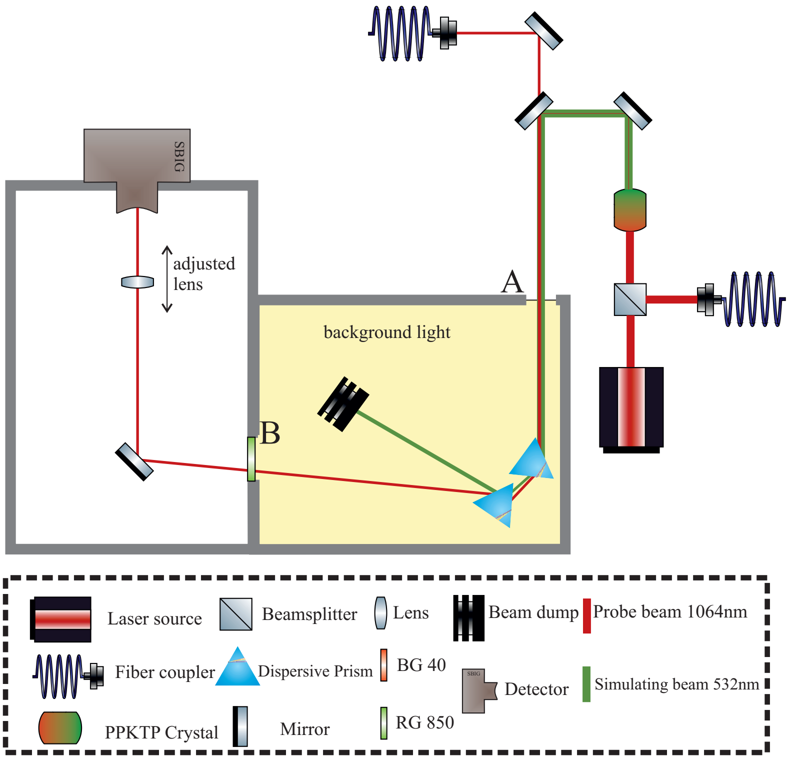

Figure 5.9: Scheme of the setup to get a sharp pictures of the prisms. The highlighted area shows the part which is exposed by room light. The lens in front of the SBIG is adjusted to make a sharp picture of the prism.

To investigate the fluorescence of the prism caused by 532 nm light, we send the green light into the box while turning off the probe beam. Additionally we installed a BG40 filter at position **A** (see Figure 5.4) to block the infrared fraction of the room light. Now only 532 nm light hits the prisms and we know its position on the CCD. The main reason for keeping the RG850 filter at position **B** is to ensure that the stray light coming out of the beam dump for 532 nm is kept away from the detector. Although the filters have shown to be fluorescent at 532 nm the intensity of the stray light is low enough so it cannot be detected on the time scales of this experiment. In case the prisms are not exhibiting any fluorescence, a picture only taken with a green beam should remain completely dark.

For the picture in Figure 5.10a both filters were installed as described above and 30 mW of green light were irradiated for 3600 s. As can be seen there are some light artifacts visible. Due to the installed RG850 filters this light must be of larger wavelength than 532 nm. This assumption was proven by installing a BG40 filter behind the RG850 filters at position **B** and recording a picture under the same conditions. The result is not shown here but was essentially a dark frame

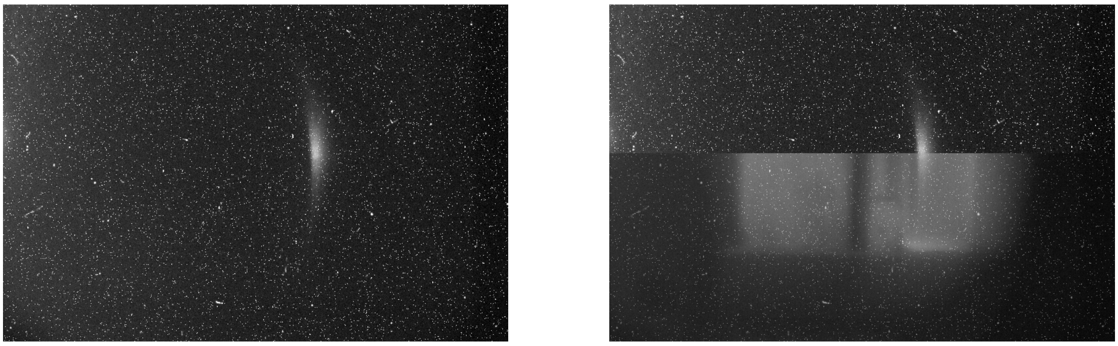

(a) (b)

Figure 5.10: Picture (a) shows the fluorescence light produced by the prism. Picture (b) is a combination of (a) and picture 5.8a.

which means that the light visible in Figure 5.10a was indeed infrared.[2] Figure 5.10b is a combination of pictures 5.8 and 5.10a. It illustrates that the infrared light originates from the same position in the picture as the probe beam. Since the 532 nm beam and the probe beam were overlapped the conclusion can be drawn that the 532 nm light induces fluorescence in the prisms. Due to the low rate of the irradiating green power we are far away from our requirements. Thus a photon-counting was not done at this point. The fact that the prisms exhibit fluorescence when irradiated by the green beam leads to the necessity of designing a new setup.

The fact that even intensities as low as 34 mW of green light caused undesirable light converted in both the absorbing filters and the dispersive prisms, leads us to design a new setup in which the main part of the green beam is not absorbed or transmitted. In the new setup we use dichroic mirrors which are highly reflective (HR) for 532 nm photons and highly transmissive for infrared 1064 nm photons. The mirrors from the company Laser Components GmbH reflect up to 99,5% of the incoming green light and simultaneously transmit up to 97% of the infrared light. Using more then one of these mirrors consecutively should result in the desired attenuation.

---

[2] At least we know that the light has a wavelength of $\lambda > 532$ nm. Although, because of its form, we can expect that it is caused by the infrared light which goes through the SHG crystal.

5.4.2 Setup Hamburg

For the construction of the new setup we were able to use the new laboratories in Hamburg. As already mentioned in section 5.4, the laser system and its frequency doubling setup (see section 5.4.1) as well as other experiments in the same lab in Hanover caused a high level of background light that made measurements near the dark rate of the detector challenging. The two important advantages of the laboratory in Hamburg compared to Hanover are:

- **Laser source**
  In Hamburg we could fall back to a Verdi Laser from the company Coherent. The Verdi laser system is a solid state, diode pumped, frequency doubled laser that provides a single frequency green beam with 532 nm wavelength and an output power of 2 W. The laser has a Neodymium Vandate (ND:YVO) crystal as the gain medium and a Lithium triborate (LBO) crystal as the frequency doubling crystal. Due to an optical diode it is unidirectional. The laser transition is homogeneously broadened and therefore the system runs very well on a single frequency. The output mirror of the internal infrared resonator is dichroic and therefore highly reflective at 1064 nm but essentially completely transparent at 532 nm [134]. With this laser source we had much less problems with unwanted infrared light from the SHG generation than in Hanover.
- **Background light**
  As mentioned above the background light originating from the laser system and also other experiments produced a high dark count rate in our lab in Hanover. In Hamburg we were able to use two completely dark laboratories for our measurements. The Verdi laser as the source could be set up in a different room from the CCD detector (see Figure 4.7). For sending light from one lab to the other, both laboratories are connected via a 10 m long opaque tube. In this way it was much easier to keep the detector free from unwanted light from the laser system and to guide only the green laser beam to the attenuator unit and the detector.

First setup

The first of several setups constructed in Hamburg was, considering the experiences gained in Hanover, based on an attenuation via dichroic mirrors reflecting the green light. A narrow band fiber coupled diode laser model 51nanoFCM from the company Schäfter+Kirchhoff with the wavelength of 1064 nm and an attenuated output power of 1 mW was used as the probe beam. Optical apertures were used to ensure that the green beam from the Verdi laser and the infrared beam of the diode laser overlapped over the range of 10 m.

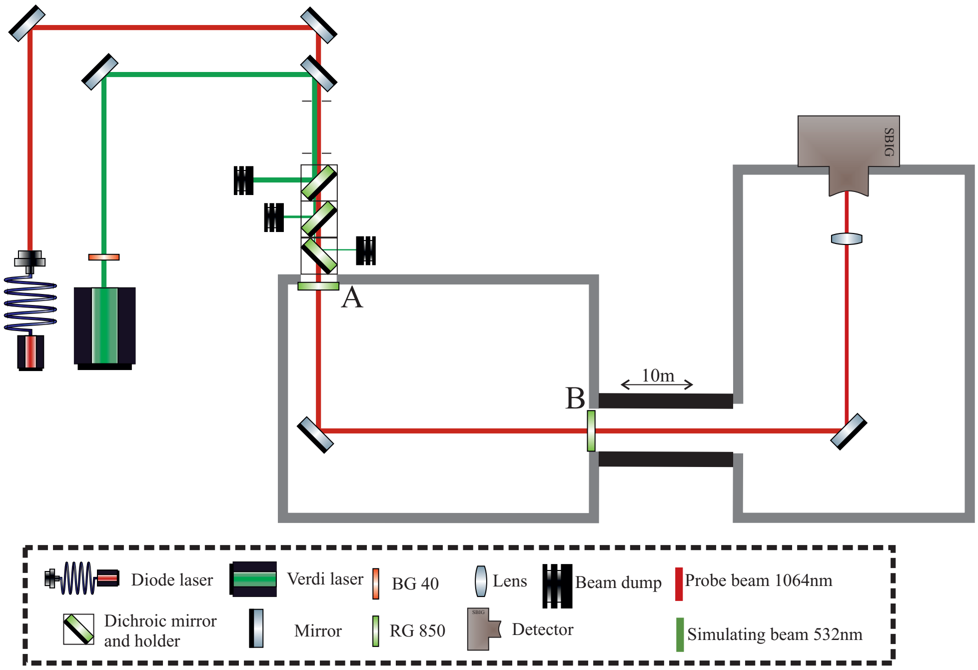

Figure 5.11: First setup in Hamburg with 10 m distance between the laser and the attenuation unit with the detector. The dichroic mirrors are used for attenuation.

In the first setup the laser and the attenuation unit were set up in a room, separate from the detector (see Figure 5.11). Due to the 10 m long tube, only a small percentage of light emitted from an unfocused source of down conversion would be able to reach the detector. The dichroic mirrors which were used for attenuating the green beam were placed at the input aperture of the light-tight box so that the reflected green beam could not enter the box and hit the detector. For this purpose special mirror holders were designed. These holders were mounted light-tight to the detector box. Each holder contains one dichroic mirror with an angle of 45° relative to the laser beam. Multiple holders were fixed to each other such that the green beam was reflected out of the holder on the left or on the right side. Figure 5.12 shows the design of these holders designed by Robin Bähre [90].

Behind the dichroic mirrors three RG850 filters were installed inside the box at positions **A** and **B** to absorb the remaining green light. An aluminum mirror guides the beam through the 10 m long tube into the detector lab. In this lab a second light tight box was installed directly attached to the tube. On the other side of the box the CCD camera is mounted. An HR coated mirror reflects the 1064 nm probe beam which is focused with a lens onto the camera.

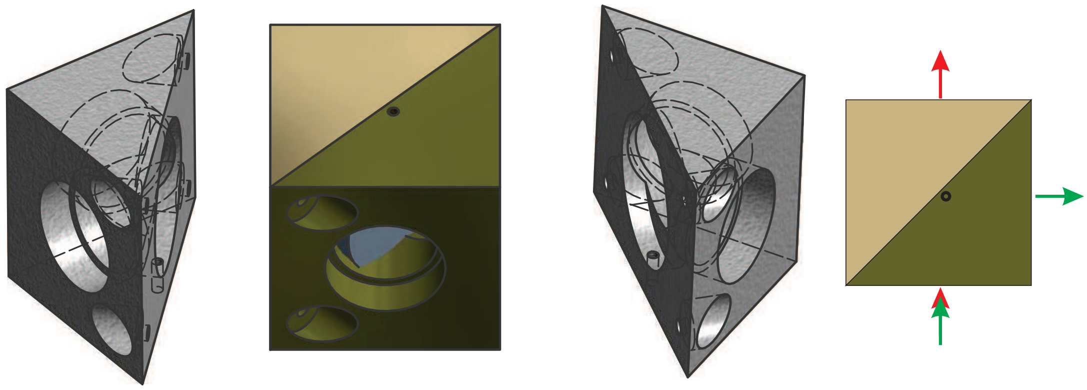

Figure 5.12: CAD drawings of the mirror holders that are being used for the light-tight connection of the dichroic mirrors to the attenuation box.

Figure 5.13 shows the two possibilities of the adjustment of the infrared beam position on the camera. Figure 5.13a shows the 1 mW infrared test laser beam. The exposure time of this picture is 100 ms. Figure 5.13b shows the infrared content coming out of the Verdi laser. To record the infrared light of the Verdi a much longer exposure time of 600 s was required. It is interesting too see that the infrared part of Verdi, which is not wanted for operating an experiment with this laser, is still very well directed after more than 10 m. One can explain this with the setup of the internal amplification cavity for the SHG process in the Verdi, which produces collinear by fundamental and second harmonic beams [134]. However we were able to use the infrared part of the Verdi to confirm the spot of the probe beam on the camera.

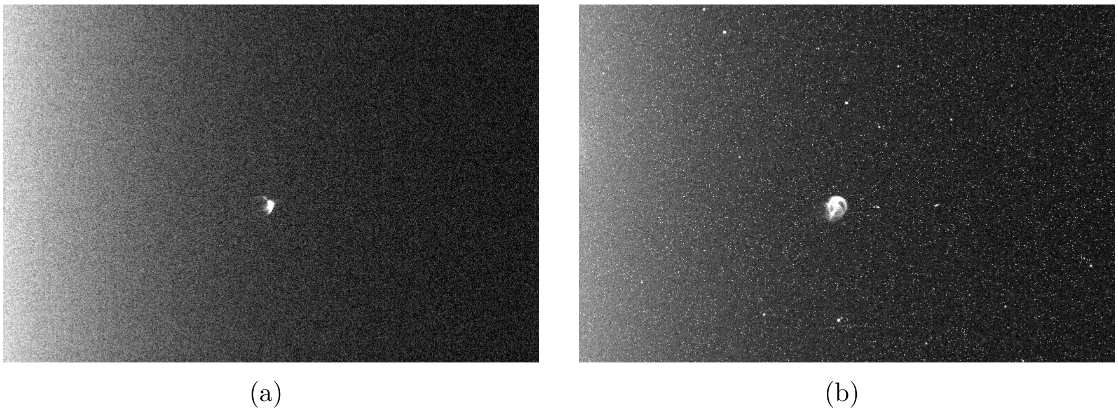
(a) (b)

Figure 5.13: Two possibilities for realizing a probe beam in the setup shown in Figure 5.11. Picture (a) shows the probe light of the test laser and picture (b) shows the residual infrared part of the Verdi laser.

Since the picture in Figure 5.13b was produced by infrared contributions of the Verdi it was necessary to install a BG40 infrared filter to block this light. The BG40 filter was mounted in the laser room in front of the attenuation box. With this setup it was possible to carry out the first longtime exposure measurement with the CCD camera. The longest, reasonable exposure time with our camera was 3600 s. Pictures with longer exposure times than one hour could be distorted because of effects like signals from cosmic rays or radioactivity which can lead to a count on the CCD camera [1].

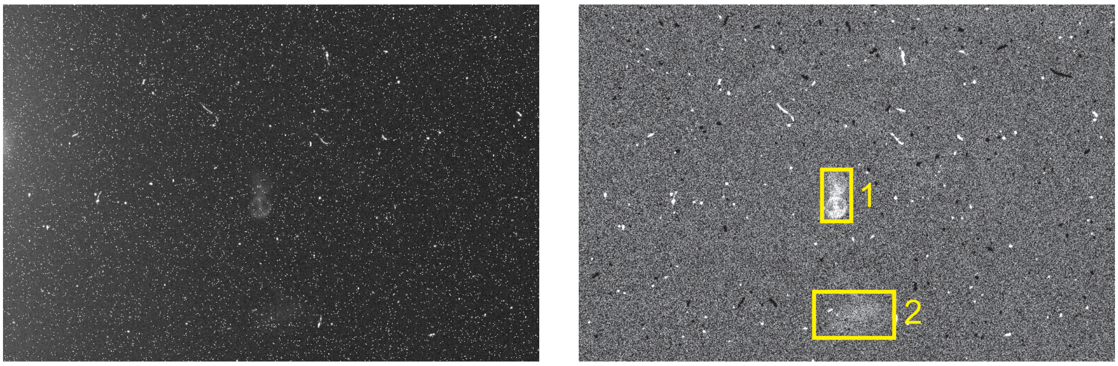

(a)

(b)

Figure 5.14: First measurement in Hamburg with an exposure time of 3600 s. Both frames shown here are the from the same measurement. Picture (b) is with a subtracted dark frame.

Figure 5.14 shows the result of the first longtime measurements with acceptable attenuation. Figure 5.14a shows the recorded bright frame with a green power of 1 W and an exposure time of 3600 s. Figure 5.14b shows the same picture subtracted by an one hour dark frame. The fact that the longtime frame is far from overexposing the CCD camera makes it interesting to calculate the number of photons which arrive at the camera. However, one can learn another fact only by looking at the recorded frames. Two circles are visible which remind us of the pictures taken in Hanover (see Figure 5.7). In Hanover we were able to deduce that the broad banded fluorescence light is being reflected on the two surfaces of the HR 1064 nm coated mirror. It is reasonable to assume that the same effect causes the circles in this picture from Hamburg. The major difference between the pictures from both labs is the position of the second reflex. This can be explained by a change in the relative orientation between the normal vectors on the faces of mirror and camera chip in the Hamburg lab compared to the Hanover lab. In Figure 5.14b one can see a second spot at position **2** . This spot has the same origin than the main spot (it will be proven later) and is not disturbing us because it is far away from the area where the probe beam hits the CCD. To confirm the assumption that this light is similar to the fluorescence light detected in Hanover we placed a BG40 filter at position A behind the RG850 filters. The energetically lower fluorescence light should be absorbed by this filter and we should record a completely dark frame. The measurement with this filter was completely dark as exemplified in Figure 5.2. To calculate an approximation of the number of photons that arrive at the detector, we have to make the assumption that all photons which are detected have a wavelength of 1064 nm so we can calculate a quantum efficiency of approximately 2%. However at this moment we know only that the detected photons have a wavelength between 800 nm and 1200 nm. For the calculation we need the number of irradiated photons. The number of photons per seconds results from

$$n_{ph} = \frac{\overline{ADU} \cdot g_{e-} \cdot S}{T \cdot Q_e} \qquad , \tag{5.2}$$

where S is the irradiated area in pixels, and $\overline{ADU}$ the average value of the analog to digital units averaged over the pixels in area S. This value is calculating directly by the operating software for the SBIG camera. For the simplification I used this value and multiplied it with S to calculate total number of ADUs in the irradiated area. g_{e-} is the conversion factor from ADU to photon counts (see equation (5.1)), T the exposure time in seconds and Q_e is the Quantum efficiency of the SBIG at 1064 nm wavelength. The area **1** in frame 5.14b is 40 × 25 pixels and the average $\overline{ADU}$ in this area amount to 30. With an exposure time of 3600 s and a gain factor of 1.5, we can calculate that approximately $n_{ph} \approx 625 \pm 2.9\,\frac{\mathrm{ph}}{\mathrm{s}}$ arrived at the detector.[3] It should be again noted that this calculation assumes that all detected photons are 1064 nm. For wavelengths smaller than 1064 nm the quantum efficiency is higher and thus the calculated photon number smaller. With the formula

$$n_{verdi} = \frac{P \cdot t \cdot \lambda}{h \cdot c} \qquad , \tag{5.3}$$

we can calculate the number of photons in the incoming green laser beam. Where h is the Planck's constant, P is the power of the incoming laser beam and c is the speed of light. Considering equation (5.3) we know that 1 W of green light from the Verdi laser emits $n_{verdi} \approx 2.68 \cdot 10^{18}\,\frac{\mathrm{ph}}{\mathrm{s}}$. With

$$\mathrm{OD} = \frac{I}{I_0} \propto \frac{n_{ph}}{n_{verdi}} \approx \frac{625}{2.68 \cdot 10^{18}} \qquad ,$$

we can calculate that with this setup an attenuation of $\mathrm{OD} \approx 2.33 \cdot 10^{-16}$ was reached.

---

[3] The standard deviation of $\pm 2.9\,\mathrm{ph}/\mathrm{s}$ can be neglected because we are interested in the orders of magnitude of the attenuation. Adding a few single photons is not crucial for the calculations.

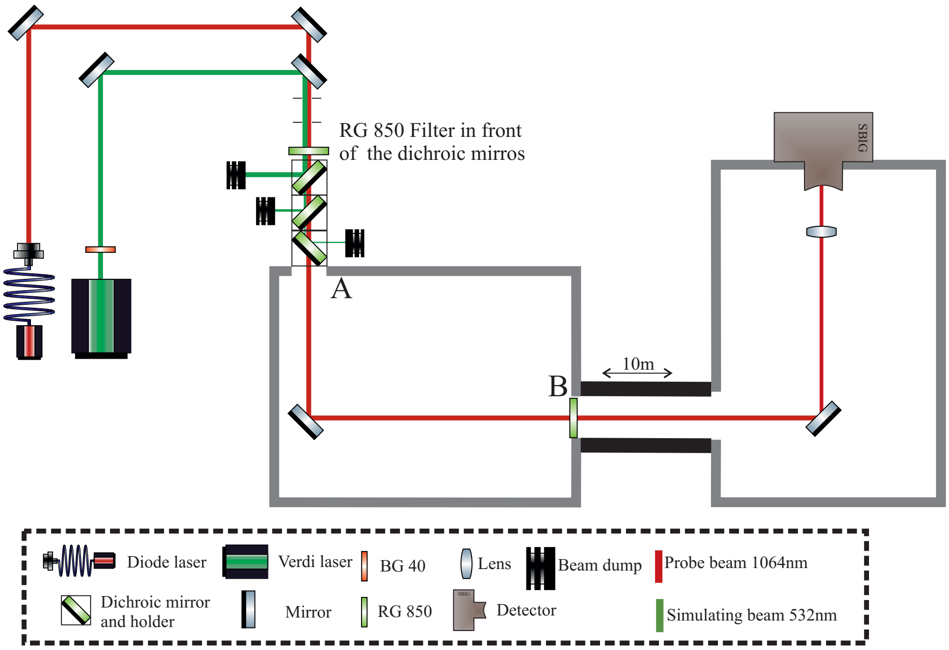

Figure 5.15: Position change of the absorbing filters compared to Figure 5.11 from being behind the dichroic mirrors to the in front of them. This setup shows its fluorescing abilities.

The last change in setup that we discuss in this section supports a strong evidence for the fluorescing characteristics of the absorbing filters. For this purpose we changed the position of the RG850 filters and mounted them in front of the dichroic mirrors. This setup is shown in Figure 5.15. Principally the order of the attenuating elements should not change the attenuation. The only difference is that the green laser beam will go through the filters at first and only the remaining 532 nm photons will be reflected by the dichroic mirrors.

Figure 5.16a shows a picture with 3600 s illumination time and 1 W laser power. This picture can be explained only by fluorescence effects in the filters. After being created in the filters the fluorescence light consists of various wavelengths which are not reflected by the narrow band dichroic mirrors. Figure 5.16b shows a second picture with one hour exposure time with two BG40 filters behind the RG850 filters. It is visible that a small part of the fluorescence light can leak through the infrared filters. This indicates that the fluorescence light is broad banded.

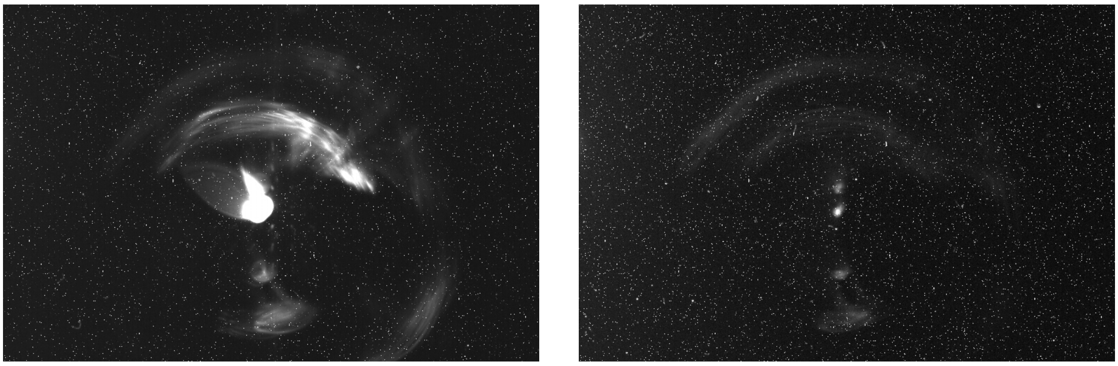
(a) (b)

Figure 5.16: Picture (a) was taken with the setup shown in figure 5.15 and shows the disturbing light produced by the RG850 filters. Picture (b) was taken with the same setup but with BG40 behind RG850 filters.

Final setup

After the setup mentioned above produced some promising results, we decided to modify the setup and bring it closer to the actual ALPS-II experiment. As described in chapter 4, the attenuation unit is included in the actual plans of ALPS-II and located just next to the detector. That implies for the second setup in Hamburg the change of the position of the attenuation box from the lab where the laser was placed into the lab where the detector was placed. On the basis of the information we gained from the last setup, we decided to make other modifications. We wanted to be able to make more detailed statements than it was possible with the pictures shown in 5.14. We placed a narrow band absorption filter (LL01-1064) from the company Semrock in front of the camera. This type of filters are designed for cleaning up the laser outputs and transmit more than 90% of the light at a precisely defined wavelength and at the same time offering steep edges in the transmission spectrum to remove optical noise due to spontaneous emission [112] (see table A.3). Furthermore we replaced an HR 1064 nm mirror with two dispersive prisms. With this we want to try a better separation between 1064 nm photons and other photons with different wave lengths. Picture 5.17 shows the new setup. For the new setup we used the same procedure as for the first setup to mark the position of infrared beams on the camera, but this time make some efforts to focus the laser beam as small as possible onto the camera. Since we want to replace the camera with a fiber which will guide regenerated photons to the TES [29, 43], we can as well produce a focus like a fiber coupler would at the place where the fiber will be situated in the final ALPS-II setup.

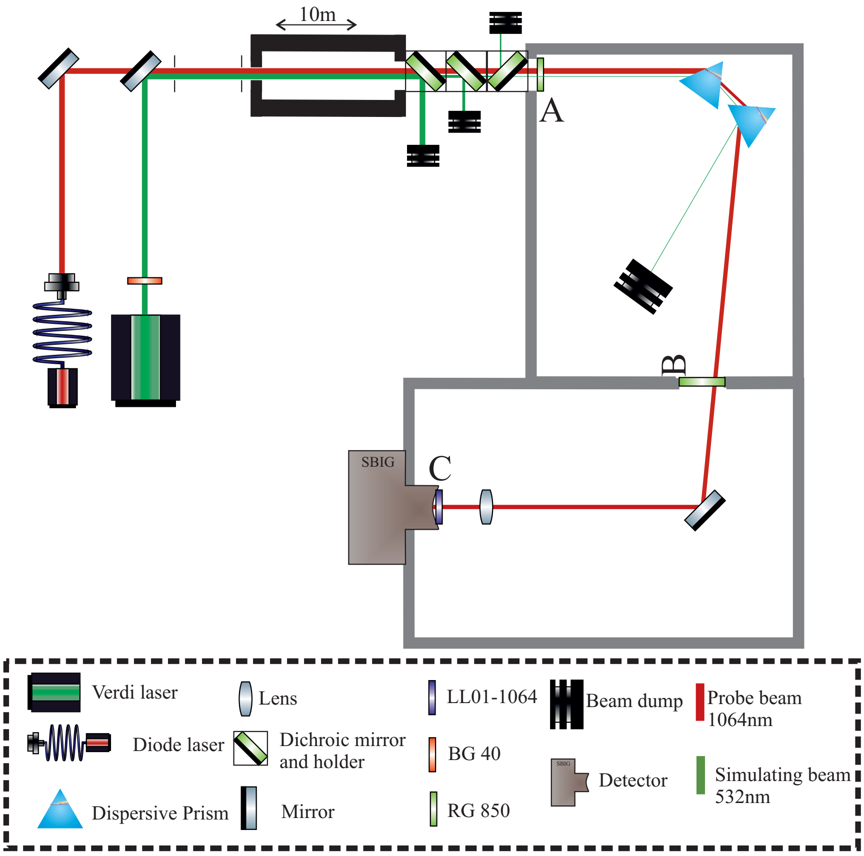

Figure 5.17: Second setup with dispersive prisms and including a narrow band filter. The attenuation unit is placed in the lab with the SBIG detector. This setup is more similar to the proposed ALPS-II setup.

Picture 5.18 shows the spot of the probe beam and the spot of the infrared part of the Verdi laser. The best that we could focus the test laser was a spot of 9 × 6 pixels. That picture has an exposure time of 100 ms and is shown in Figure 5.18a. Figure 5.18b shows the infrared part of the Verdi. This beam is not as well focused as the probe beam and covers an area of 13 × 4 pixels. The reason for the different sizes of the spots is that the lens in front the camera is only adjusted for the probe beam and not for the Verdi beam which has different geometrical characteristic.

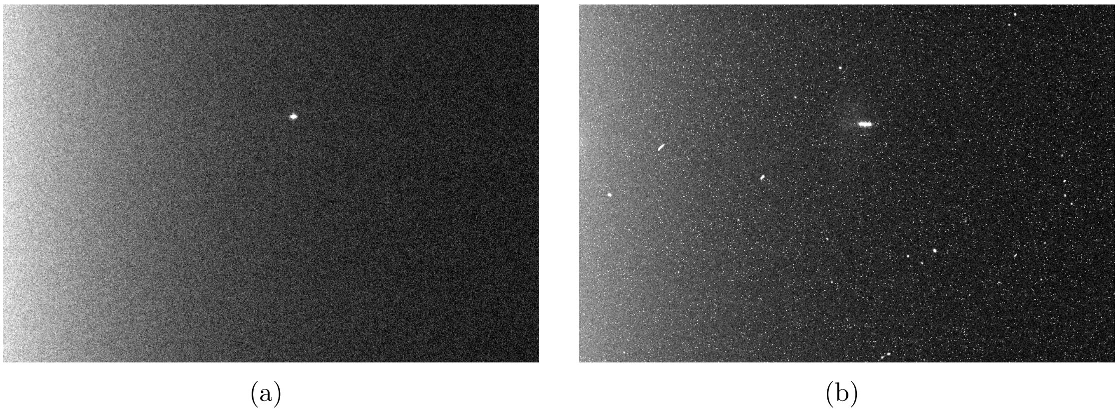
(a) (b)

Figure 5.18: Picture (a) shows the focused beam of the probe laser. Picture (b) shows the focused beam of the infra red light from the Verdi. Because of the different geometrical properties of these two beams,they do not have the same size.

Figure 5.19 shows the two final pictures taken with the setup explained above. Each picture was exposed for 3600 s. Figure 5.19a was recorded with 1 W output power from the Verdi and Figure 5.19b was recorded with 2.5 W. This is the highest possible output power of our Verdi laser. With Equation (5.2) we can calculate the photon numbers. For 1 W we get once more $2.68 \cdot 10^{18}\,\frac{\mathrm{ph}}{\mathrm{s}}$ and for 2.5 W there are $6.69 \cdot 10^{18}\,\frac{\mathrm{ph}}{\mathrm{s}}$. With Equation (5.2) we can calculate the number of photons which arrive at the camera.

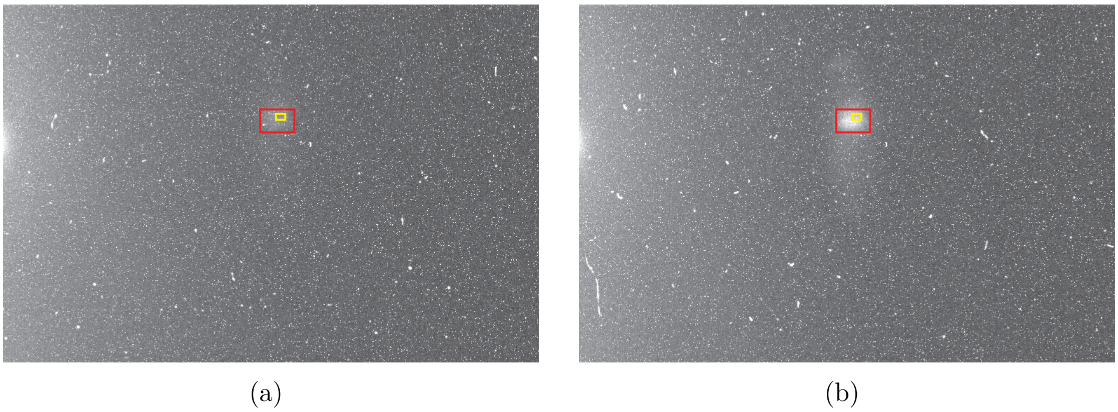
(a) (b)

Figure 5.19: Final pictures with an exposure time of 3600 s and 1 W of incoming light in picture (a) and 2.5 W respectively in picture (b).

In picture 5.19a we can measure an average ADU number of $\overline{ADU} = 35$ per pixel in the red marked area. The illuminated area covers 41×43 pixels. This leads to a total flux of $n_{ph} \approx 1285.5 \pm 4.2\,\frac{\mathrm{ph}}{\mathrm{s}}$. This corresponds to an attenuation of

$$\begin{aligned} \mathrm{OD} &= \frac{n_{ph}}{n_{verdi}} \\ &\approx \frac{1285}{2.68 \cdot 10^{18}} \\ &\approx 4.8 \cdot 10^{-16} \qquad . \end{aligned} \tag{5.4}$$

In Figure 5.19b there is an average ADU number of $\overline{ADU} = 91$ ADUs per pixel in the red marked area. This corresponds to $n_{ph} \approx 3342.3 \pm 6.8\,\frac{\mathrm{ph}}{\mathrm{s}}$ over the same area as in Figure 5.19a. With 2.5 W of incoming laser power, we can calculate an attenuation of

$$\mathrm{OD} \approx \frac{3342}{6.69 \cdot 10^{18}} \approx 4.9 \cdot 10^{-16} \qquad . \tag{5.5}$$

This kind of calculation considered all photons which are detected in the chosen area around the maximum intensity on the CCD surface. Since we want to use a fiber instead of a camera this can be seen as a upper limit because we calculated with a larger area than that of the fiber surface. This also means that the regenerated beam should be focused on a tight spot to ensure a high coupling efficiency into the fiber. As visible in Figure 5.18a the probe light is mostly very sharply focused on the camera. The disturbing fluorescence light is not focused as well as the probe beam because it is not directed. If we imagine a fiber input coupler instead of the CCD surface, this input coupler will guide only the focused light into the TES. Most of the fluorescence light will not couple into the fiber because only a small fraction that actually hits the focusing lens at the right angle will get into the fiber. This is another strong geometrical attenuation process for down converted photons. Under these circumstances we can develop a more realistic scenario. For this we consider only the pixel number which was actually hit by the probe beam. That area was specified by evaluating picture 5.18a in which the beam was tightly focused. We calculate the average ADU in the exact same area. This was done for the two pictures of Figure 5.19. For 5.19a with 1 W input power we can calculate an average ADU of $\overline{ADU} = 19$ ADUs per pixel. This leads to a total number of $n_{ph} \approx 21.3 \pm 0.5\,\frac{\mathrm{ph}}{\mathrm{s}}$ in the 9×6 pixel area of the probe light. With these findings we can calculate an attenuation of

$$\mathrm{OD} \approx \frac{21}{2.68 \cdot 10^{18}} \approx 7.9 \cdot 10^{-18} \qquad . \tag{5.6}$$

For Figure 5.19b with 2.5 W input power the average ADU number is $\overline{ADU} = 39$. This leads to $n_{ph} \approx 43.8 \pm 0.9\,\frac{\mathrm{ph}}{\mathrm{s}}$ in the area of the probe beam. We can calculate analogously to Figure 5.19a

$$\mathrm{OD} \approx \frac{44}{6.69 \cdot 10^{18}} \approx 6.6 \cdot 10^{-18} \qquad . \tag{5.7}$$

The laser power of the probe laser was measured with a S121C power meter from Thorlabs [106]. Behind the tube and in front of the attenuation box a power of 400 ± 20 µW was measured. In front of the CCD surface and behind all attenuation components (dichroic mirrors, prisms and absorbing filters) the probe beam power was measured to be 343 ± 18 µW. This leads to a transmission value for 1064 nm of the attenuation box of ≈85%.

We can also make another estimation for the attenuation of the green light in case of an even better focus. Let's assume that we would be able to focus the probe beam onto one pixel. As described before evaluating Figure 5.19, the coupling of the fluorescence light will not change in this case. Therefore we can make a final calculation for only one pixel. Figure 5.20 shows this estimation for 1 W input power.

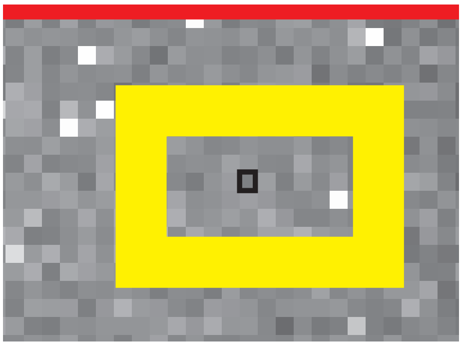

Figure 5.20: Cutout of picture 5.19a for the one pixel estimation. The pixel is framed black.

As mentioned above for Figure 5.19a, we calculate with $\overline{ADU} = 19$ ADU for the pixel this leads to $n_{ph} \approx 0.39 \pm 0.07\,\frac{\mathrm{ph}}{\mathrm{s}}$ for this pixel and an attenuation of

$$\mathrm{OD} \approx \frac{0.4}{2.68 \cdot 10^{18}} \approx 1.5 \cdot 10^{-19} \qquad . \tag{5.8}$$

However, because we were not able to focus the probe beam onto one pixel, this value cannot be recognized as the final result and will not be considered in the next section.

5.5 Results

The measurements which are shown in Figure 5.19b represent the final results of the attenuation experiment. With the described setup it is possible to attenuate a green input power by more than 17 orders of magnitude. At the same time the attenuation unit is highly transmissive for infrared photons with a transmission coefficient of ≈85%. The value which has been calculated with equation (5.7) is the highest factor of attenuation which could be achieved with the existing devices. This value is still higher than the design goal of the ALPS-II experiment ($\approx 10^{-19}$, see also section 5.2.1). However the current state of the TES detector shows a dark count rate of $1 \cdot 10^{-4} \frac{\mathrm{ph}}{\mathrm{s}}$. This means that the attenuation of the presented setup would be sufficient for the first runs with the TES detector. A comparable setup which provides a wavelength depended light attenuation in the required scope is not currently known to our collaboration.

5.6 Conclusion

The shown results of this attenuation experiment are the first steps towards the direction of accurately distinguishing between 532 nm and 1064 nm photons. The attenuation factor can be calculated more precisely by the methods which are used in the analysis of the ALPS-I experiment [1]. For this thesis it was more important to design, build and test a working setup which shows the possibility of reaching the required attenuation of the control light of the regeneration cavity. To prove that this setup can also attenuate the green input power by 20 to 21 orders of magnitude, one has to increase either the input power of the green laser beam or decrease the dark count rate of the detector. Replacing the detector (for example with a PIXIS camera or a TES) can lead to a higher sensitivity. Since the used SBIG camera has such a high dark count rate it was impossible to measure an attenuation below 10^{-18} with the used laser power. The following tables shows the different possible setups aiming to increase the sensitivity of the attenuation experiment and the detectable attenuation.

Table 5.1 shows a list of different combinations of light sources and detectors to test the attenuation of the setup presented in this chapter. These are only setups which make use of devices that are already existing in our lab. Suggestion number two which includes the PIXIS camera as the detector is now realizable since the PIXIS is now available. These measurement and interpretation of tests with the PIXIS camera can be carried out analogous to the procedure that was presented here. Suggestion number three includes the TES. This measurements should be different compared to the tests with the CCD device and needs some

Attenuation experiment			
#	Source	Detector	Detectable attenuation
1	Verdi P= 1 W $n_{ph} \approx 10^{18}$	SBIG $Q_e \approx 1-2\%$ DC=1 $\frac{\text{ph}}{\text{s}}$	10^{-18}
2	Verdi P= 1 W $n_{ph} \approx 10^{18}$	PIXIS $Q_e = 1,21\%$ DC=$1 \cdot 10^{-3}\frac{\text{ph}}{\text{s}}$	10^{-21}
3	Verdi P= 1 W $n_{ph} \approx 10^{18}$	TES $Q_e \approx 60\%$ DC=$1 \cdot 10^{-4}\frac{\text{ph}}{\text{s}}$	10^{-22}
4	Green Cavity $P_i = 1$ W PB=60 $n_{ph} \approx 10^{20}$	PIXIS $Q_e = 1,21\%$ DC=$1 \cdot 10^{-3}\frac{\text{ph}}{\text{s}}$	10^{-23}

Table 5.1: Possible combinations of source and detector to increase the sensitivity of the attenuation experiment

considerations concerning the coupling of the test beam and the converted light into the fiber which is connected to the TES[4]. Suggestion number four implies a low finesse (f≈ 180) cavity for 532 nm photons as the source. The optical setup of such a cavity is described in [1] and [3]. The low finesse is to simplify the stabilization of the cavity and to make it possible to use the end-mirrors CB2A and REM of the regeneration cavity of the ALPS-II setup. As a detector one could use the PIXIS which is far more uncomplicated to handle than the TES in its current status. The suggestion number four can verify the highest attenuation if one considers the number of photons which are circulating in the cavity. This suggestion is interesting because with such a setup we were able to investigate possible effects from the circulating green photon filed in the RC on the surface or substrates of the CBS2A mirrors (see Figure 4.4). In such a cavity we have a higher number of circulating photons but the number of photons which are transmitted from it is almost the same as in the laser entering it. The suggestions 2-4 which are presented in table 5.1 are indeed all improvements compared suggestion number 1 which was presented in this chapter.

Only suggestion number three can reach a sufficient level of attenuation as shown in table 5.2. Building a cavity like it is suggested in number four would be interesting for probing the properties of the end mirrors. In that case the increased of the number of photons of the source as it is shown in table 5.1 is only valid if we

---

[4] The function of the TES and the coupling fiber are explained in more detail in [29].

compare this with the number of green photons which are circulating in the RC of ALPS-II. In that case we have to calculate the attenuation with 8,3 mW green power instead of 150 µW.

ALPS-II comparability			
#	Source	Detector	Required attenuation
1	KTP P= 150 µW $n_{ph} \approx 4 \cdot 10^{14}$	TES $Q_e \approx 60\%$ DC=$1 \cdot 10^{-6} \frac{\mathrm{ph}}{\mathrm{s}}$	$2,5 \cdot 10^{-21}$
2	KTP P= 150 µW $n_{ph} \approx 4 \cdot 10^{14}$	TES $Q_e \approx 60\%$ DC=$1 \cdot 10^{-6} \frac{\mathrm{ph}}{\mathrm{s}}$	$2,5 \cdot 10^{-21}$
3	KTP P= 150 µW $n_{ph} \approx 4 \cdot 10^{14}$	TES $Q_e \approx 60\%$ DC=$1 \cdot 10^{-6} \frac{\mathrm{ph}}{\mathrm{s}}$	$2,5 \cdot 10^{-21}$
4	RC for green $P_i = 150$ µW PB=60 $n_{ph} \approx 2 \cdot 10^{16}$	TES $Q_e \approx 60\%$ DC=$1 \cdot 10^{-6} \frac{\mathrm{ph}}{\mathrm{s}}$	$4 \cdot 10^{-23}$

Table 5.2: Compared sensitivities in ALPS-II of the setup suggestions discussed above and shown in table 5.1.

Table 5.2 shows which configuration of the ALPS-II experiment the suggestions from table 5.1 are comparable. With the first three configurations consider the green photon beam outside of the RC which implies 150 µW of green light and the TES as detector. For these three cases only point three is reliable because the feasible attenuation which can be shown in the attenuation experiment is one order of magnitude higher than required. Point four in table 5.2 shows the situation of a possible attenuation experiment which is comparable to the situation of ALPS-II which will be built with a low-finesse cavity for 532 nm photons to increase the photon number from the source as suggested in table 5.1. The number of circulating photons in the RC is also higher and with the TES an attenuation of 10^{23} would be needed.

Instead of building another attenuation experiment with a different detector or a different light source an alternative presents itself. It would be possible to work with the attenuation box presented in this chapter first. After the completion of ALPS-IIa in Hamburg we can easily build the presented setup for the attenuation and test its reliability with a working regeneration cavity by using the PIXIS camera or the TES.

Chapter 6

Summary and outlook

In this chapter I will summarize my thesis and my work at the ALPS collaboration. A detailed and separated conclusion of the experimental parts of my work including suggestions for the further investigations can be found in sections 4.5 and 5.6. My work can be separated into three parts.

- **The relocation of the ALPS experiment**
  A first step was the relocation into the new laboratories and the preparation of these for optical experiments. This part of my responsibility was mentioned on several occasions in this thesis. Currently the new laboratories are prepared for the final setup of the ALPS-IIa experiment and the infrastructure work in the labs is successfully finished.
- **ALPS-IIa production cavity**
  The realization and characterization of the production cavity, as the first part of the ALPS-IIa experiment, was achieved during this thesis. It is shown that a robust lock of this cavity on time scales of hours is possible. The anticipated power build up of this cavity could not be reached during my thesis and requires further investigations. The achieved power buildup factor of ≈ 170 and the fact of the robust lock gave the opportunity to investigate vibration noise sources and cross-couplings to the production cavity in the new laboratories. Losses due to the quality of the mirrors need to be investigated further.
- **Attenuation of the green light**
  Defining a possible detection disturbance caused by the 532 nm control light

> of the regeneration cavity was the other main part of this thesis. A setup was suggested and realized. It is able to attenuate the green light while it is highly transmissive for infrared light. Possible down conversion effects due to different sources in optical components were investigated. It was ensured that these effects are not higher than the current dark count rate of the ALPS-II detector provided that the assumptions of chapter 5 are correct. This could be demonstrated by coupling the transmitted probe beam from the attenuation system into a fiber which is coupled to the SBIG or another CCD detector. The reached attenuation of $\approx 10^{-17}$ is sufficient for the current dark count rate of the TES.

The mentioned achievements of this thesis make it possible to take the final step towards the realization of the ALPS-IIa experiment. The completion of the regeneration cavity in Hamburg should take priority as the next step. In the parallel the production cavity should be modified by replacing the currently round, flat end mirror with a now available rectangular substrate. This is important for the realization of a stable common optical axis between the two cavities. For this purpose we will need a new central breadboard. The light-tightness of the regeneration area above the central breadboard should get special attention. This includes the connection of the shutter box to the central breadboard, the connection ports of the shutter box to the regeneration tube, the connection to the detector, the entrance of the green control beam and the shutter placed on the common optical axis of the cavities.

For the entrance port of the green control beam I designed and build a dichroic unit to prevent the infrared light from entering the regeneration area. The light-tightness of this unit has to be confirmed after realizing a light-tight shutter box. Apart from this main step, I suggest further investigation of the currently low finesse of the production cavity. Building a short cavity could give valuable informations about the quality of the ALPS-II mirrors as mentioned in section 4.5.

Concerning the attenuation experiment, I suggest testing of the setup presented in this thesis once the ALPS-IIa setup is completed. To invest additional efforts into new experiments, as mentioned in section 5.6, is not advised. The presented setup is easy to rebuild and its individual components are also easy to change. These features make it possible to adapt the setup to the requirements of the ALPS-II experiment in its final phase.

The construction of a stable production cavity and the realization of the green light attenuation unit were important steps regarding the feasibility of the ALPS-II concept. The achieved results allow to enter the final phase of the ALPS-IIa experiment.

Appendix A

Transmission curves

In this short appendix the transmissivity curves of different materials are given which were either used in the experiments or were important for the decisions regarding the choice of materials.

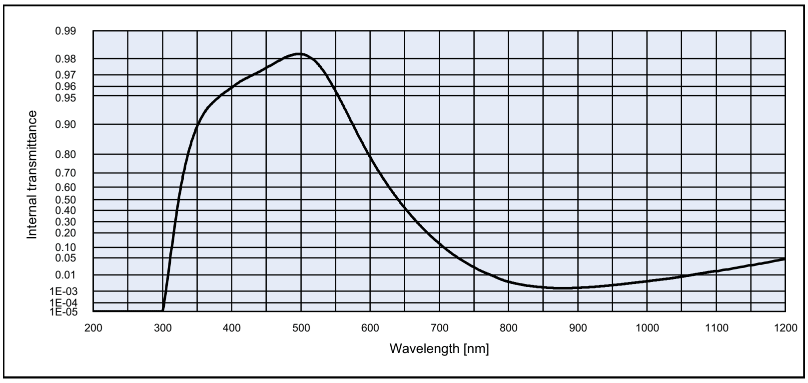

(a) BG40

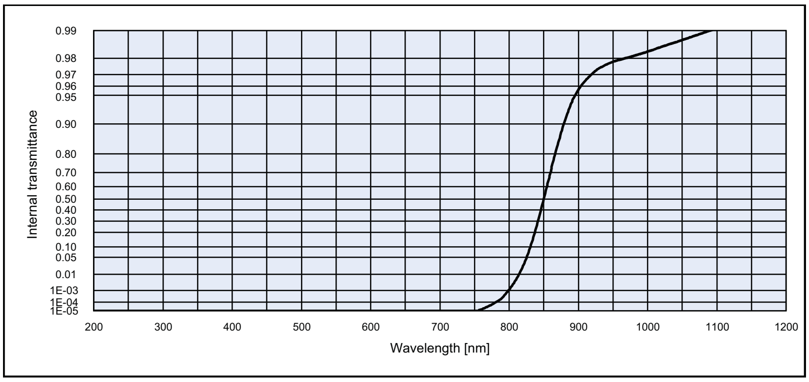

(b) RG850

Figure A.1: Shown is the transmission depending on the light wavelength for BG40 and RG850 filters.

Figure A.1 shows the transmission curves of the absorbing filters BG40 and RG850. These filters were the basic components for the first attempts of the building an attenuation setup.

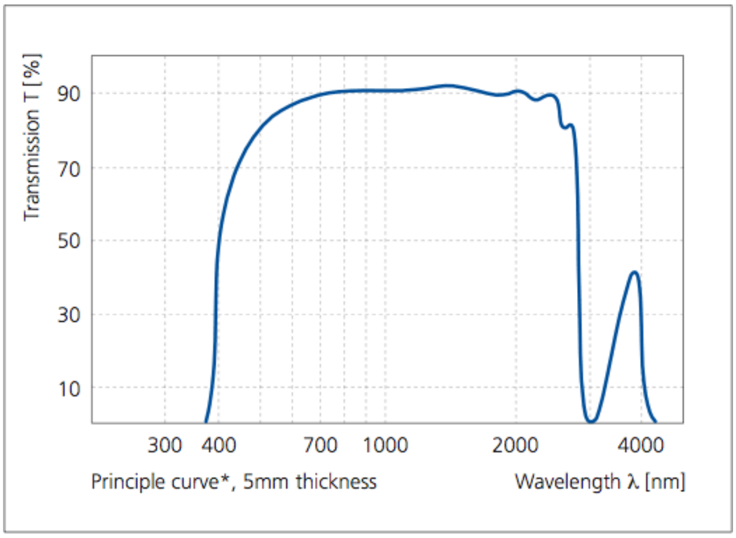

Figure A.2: The transmissivity of a 5 mm thick zerodur plate.

Figure A.2 shows the transmissivity of zerodur . As can be seen, this material is almost transparent for infrared photons. Thus is not an option for the ALPS-II experiment to use zerodur as the CB.

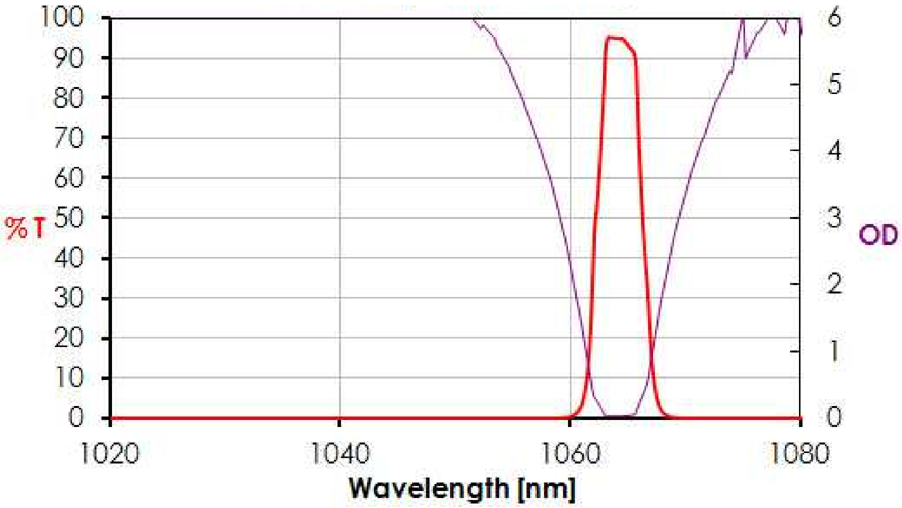

Figure A.3: The red line is the transmissivity of the narrow band absorption filter (LL01-1064).

Figure A.3 shows the transmissivity of the narrow band absorption filter from Semrock which is used to place it in front of the detector as the last attenuation component.

Acronyms

AEI	Albert-Einstein-Institute	16
ADU	analog to digital units	95
ALP	axion-like particle	8
AOM	acousto-optic modulator	61
CB	central breadboard	52
CCD	silicon-based charge-coupled device	63
CMB	cosmic microwave background	9
CTE	thermal expansion coefficient	64
DE	detection efficiency	15
DESY	Deutsches Elektronen Synchrotron	2
DWS	differential wavefront sensing	58
EOM	Electro-Optical Modulator	47
FPI	Fabry-Perot interferometer	28
FSR	Free Spectral Range	30
FWHM	Full width half maximum	33
HERA	Hadron-Electron Ring Accelerator	14
HG	Hermitian Gaussian	24
HR	highly reflective	62
HV	High Voltage	48
IBS	ion-beam sputtering	51
isc	intersystem crossing	90
KTP	Kaliumtitanylphosphat	60
LG	Laguerre Gaussian	25
LHC	Large Hadron Collider	2

LO	local oscillator	47
LSW	light-shining-through a wall	2
MOPA	Master-Oscillator-Power-Amplifier	47
ND:YAG	neodymium yttrium aluminum garnet	98
NPRO	non-planar ring oscillator	48
PB	power build-up	35
PC	Production Cavity	14
PDH	Pound-Drever-Hall	42
PI	proportional-integral	48
PZT	piezo-electric transducer	58
QCD	quantum chromo dynamics	6
QE	quantum efficiency	15
QPD	quadrant photodiode	58
RC	regeneration cavity	14
ROC	Radius of curvature	27
SHG	second harmonic generation	38
SFG	sum-frequency generation	92
SM	standard model	1
SNR	signal-to-noise ratio	48
SPDC	Spontaneous parametric down-conversion	92
TEM	Transverse Electric and Magnetic	24
TES	transition edge sensor	15
TPE	two photon emission	93
UGF	unity gain frequency	73
WISP	weakly interacting slim particle	2

BIBLIOGRAPHY

[1] Klaus Ehret, Maik Frede, Samvel Ghazaryan, Matthias Hildebrandt, Ernst-Axel Knabbe, Axel Lindner, Jenny List, Tobias Meier, et al.
New alps results on hidden-sector lightweights.
Physics Letters B, 689(4):149–155, 2010.

[2] Klaus Ehret, Maik Frede, Samvel Ghazaryan, Matthias Hildebrandt, Axel Knabbe, Ernst-Axel Lindner, Jenny List, Tobias Meier, et al.
Resonant laser power build-up in alps—a “light shining through a wall” experiment.
Nuclear Instruments and Methods in Physics Research Section A: Accelerators, Spectrometers, Detectors and Associated Equipment, 612(1):83–96, 2009.

[3] Tobias Meier.
High-Power CW Green Lasers for Optical Metrology and Their Joint Benefit in Particle Physics Experiments.
PhD thesis, Gottfried Wilhelm Leibniz Universität Hannover, 2011.

[4] Claude Amsler et al.
Review of particle physics.
Physics Letters B, 667(1):1–6, 2008.

[5] Serguei Chatrchyan et al.
Observation of a new boson at a mass of 125 gev with the cms experiment at the lhc.
Physics Letters B, 716(1):30–61, 2012.

[6] Georges Aad et al.
Observation of a new particle in the search for the standard model higgs boson with the atlas detector at the lhc.
Physics Letters B, 716(1):1–29, 2012.

[7] James W Cronin.
Cp symmetry violation-the search for its origin.
1981.

[8] Ikaros I Bigi and A Ichiro Sanda.
CP violation, volume 28.
Cambridge university press, 2009.

[9] RD Peccei and HR Quinn.
Cp conservation in the presence of instantons, 1977.
Phys. Rev. Lett, 38:1440.

[10] Roberto D Peccei.
The strong cp problem and axions.
In Axions, pages 3–17. Springer, 2008.

[11] F. Wilczek.
Problem of strong p and t invariance in the presence of instantons.
Phys. Rev. Lett., 40:279–282, Jan 1978.
DOI: 10.1103/PhysRevLett.40.279.

[12] Javier Redondo and Andreas Ringwald.
Light shining through walls.
Contemporary Physics, 52(3):211–236, 2011.

[13] Mark Srednicki.
Axion couplings to matter: (i). cp-conserving parts.
Nuclear Physics B, 260(3–4):689 – 700, 1985.
DOI: http://dx.doi.org/10.1016/0550-3213(85)90054-9.

[14] Paola Arias, Joerg Jaeckel, Javier Redondo, and Andreas Ringwald.
Optimizing light-shining-through-a-wall experiments for axion and other weakly interacting slim particle searches.
Phys. Rev. D, 82:115018, Dec 2010.
DOI: 10.1103/PhysRevD.82.115018.

[15] M. Goodsell and A. Ringwald.
Light hidden-sector u(1)s in string compactifications.
Fortschritte der Physik, 58(7-9):716–720, 2010.
DOI: 10.1002/prop.201000026.

[16] Bob Holdom.
Two u(1)'s and charge shifts.
Physics Letters B, 166(2):196 – 198, 1986.
DOI: http://dx.doi.org/10.1016/0370-2693(86)91377-8.

[17] Holger Gies, Joerg Jaeckel, and Andreas Ringwald.
Polarized light propagating in a magnetic field as a probe for millicharged fermions.
Phys. Rev. Lett., 97:140402, Oct 2006.
DOI: 10.1103/PhysRevLett.97.140402.

[18] Justin Khoury.
Chameleon field theories.

Classical and Quantum Gravity, 30(21):214004, 2013.

[19] Babette Döbrich.
Phenomenolgy of the vacuum in quntum electrodynamics and beyond.
PhD thesis, Friedrich-Schiller-Universität Jena, 2010.

[20] JL Hewett et al.
Fundamental physics at the intensity frontier.
arXiv preprint arXiv:1205.2671, 2012.

[21] Paola Arias, Joerg Jaeckel, Javier Redondo, and Andreas Ringwald.
Wispy cold dark matter.
Journal of Cosmology and Astroparticle Physics, 2012(06):013, 2012.

[22] Edward W Kolb and Michael Stanley Turner.
The early universe.
Front. Phys., Vol. 69,, 1, 1990.

[23] Martin White.
Anisotropies in the cmb.
arXiv preprint astro-ph/9903232, 1999.

[24] C. L. Bennett et al.
The microwave anisotropy probe mission.
The Astrophysical Journal, 583(1):1, 2003.

[25] PAR Ade, N Aghanim, et al.
Planck 2013 results. xvi. cosmological parameters.
arXiv preprint arXiv:1303.5076, 2013.

[26] S. Perlmutter et al.
Measurements of Omega and Lambda from 42 high redshift supernovae.
Astrophys.J., 517:565–586, 1999.
DOI: 10.1086/307221.

[27] Anatoly Klypin, Jon Holtzman, Joel Primack, and Eniko Regos.
Structure formation with cold+ hot dark matter.
arXiv preprint astro-ph/9305011, 1993.

[28] J Navarro and Simon DM White.
The structure of cold dark matter halos.
In SYMPOSIUM-INTERNATIONAL ASTRONOMICAL UNION, volume 171, pages 255–258. KLUWER ACADEMIC PUBLISHERS GROUP, 1996.

[29] Jan Dreyling-Eschweiler.
A superconducting microcalorimeter for low-flux detection of near-infrared single photons.
PhD thesis, Universität Hamburg, 2014.

[30] Philip A Pinto and SE Woosley.
The theory of gamma-ray emergence in supernova 1987a.
Nature, 333(6173):534–537, 1988.

[31] Alexandre Payez, Jean-René Cudell, and Damien Hutsemekers.
Axions and polarisation of quasars.
arXiv preprint arXiv:0805.3946, 2008.

[32] Georg G Raffelt.
Stars as laboratories for fundamental physics: The astrophysics of neutrinos, axions, and other weakly interacting particles.
University of Chicago press, 1996.

[33] Adrian Ayala et al.
An improved bound on axion-photon coupling from globular clusters.
arXiv preprint arXiv:1406.6053, 2014.

[34] Andreas Ringwald.
Exploring the role of axions and other wisps in the dark universe.
Physics of the Dark Universe, 1(1):116–135, 2012.

[35] Manuel Meyer, Dieter Horns, and Martin Raue.
First lower limits on the photon-axion-like particle coupling from very high energy gamma-ray observations.
Physical Review D, 87(3):035027, 2013.

[36] Babette Döbrich.
Alps internal note, 2014.

[37] P. Sikivie.
Experimental tests of the ”invisible” axion.
Phys. Rev. Lett., 51:1415–1417, Oct 1983.
DOI: 10.1103/PhysRevLett.51.1415.

[38] K Zioutas, S Andriamonje, V Arsov, S Aune, D Autiero, FT Avignone, K Barth, A Belov, B Beltrán, H Bräuninger, et al.
First results from the cern axion solar telescope.
Phys. Rev. Lett., 94:121301, Apr 2005.
DOI: 10.1103/PhysRevLett.94.121301.

[39] I Shilon, A Dudarev, H Silva, and HHJ ten Kate.
Conceptual design of a new large superconducting toroid for iaxo, the new international axion observatory.
Applied Superconductivity, IEEE Transactions on, 23(3):4500604–4500604, 2013.

[40] Karl van Bibber and Gianpaolo Carosi.
Status of the admx and admx-hf experiments.
arXiv preprint arXiv:1304.7803, 2013.

[41] A Afanasev et al.
Experimental limit on optical-photon coupling to light neutral scalar bosons.
Physical review letters, 101(12):120401, 2008.

[42] Matthias Schott et al.
First results of the full-scale osqar photon regeneration experiment.
arXiv preprint arXiv:1110.0774, 2011.

[43] R Bähre, B Döbrich, J Dreyling-Eschweiler, S Ghazaryan, R Hodajerdi, D Horns, F Januschek, E A Knabbe, A Lindner, D Notz, A Ringwald, J E von Seggern, R Stromhagen, D Trines, and B Willke.
Any light particle search ii — technical design report.
Journal of Instrumentation, 8(09):T09001, 2013.

[44] Luciano Maiani, R Petronzio, and E Zavattini.
Effects of nearly massless, spin-zero particles on light propagation in a magnetic field.
Physics Letters B, 175(3):359–363, 1986.

[45] Georg Raffelt and Leo Stodolsky.
Mixing of the photon with low-mass particles.
Phys. Rev. D, 37:1237–1249, Mar 1988.
DOI: 10.1103/PhysRevD.37.1237.

[46] Dieter Trines.
Alps ii: Magnets, 2013.

[47] Jan Eike von Seggern.
Constraining Weakly Interacting Slim Particles with a Massive Star and in the Laboratory.
PhD thesis, Universität Hamburg, 2013.

[48] B.E.A. Saleh and M.C. Teich.
Fundamentals of Photonics.
Wiley Series in Pure and Applied Optics. Wiley, 2007.

[49] A. Lipson, S.G. Lipson, and H. Lipson.
Optical Physics.
Cambridge University Press, 2010.

[50] H. KOGELNIK and T. LI.
Laser beams and resonators.
Appl. Opt., 5(10):1550–1567, October 1966.
DOI: 10.1364/AO.5.001550.

[51] A.E. Siegman.
Lasers.
University Science Books, 1986.

[52] O. Svelto.
Principles of Lasers.
Springer, 2010.

[53] Léon Georges Gouy.
Sur une propriété nouvelle des ondes lumineuses.
Gauthier-Villars, 1890.

[54] D. Meschede.
Optics, Light and Lasers: The Practical Approach to Modern Aspects of Photonics and Laser Physics.
Physics textbook. Wiley, 2007.

[55] Ilja N. Bronstein, Konstantin A. Semendjajew, and Gerhard Musiol.
Taschenbuch der Mathematik, m. CD-ROM.
Deutsch (Harri), 2008.

[56] Dana Z. Anderson.
Alignment of resonant optical cavities.
Appl. Opt., 23(17):2944–2949, Sep 1984.
DOI: 10.1364/AO.23.002944.

[57] S. Schiller, C. Lämmerzahl, H. Müller, C. Braxmaier, S. Herrmann, and A. Peters.
Experimental limits for low-frequency space-time fluctuations from ultra-stable optical resonators.
Phys. Rev. D, 69:027504, Jan 2004.
DOI: 10.1103/PhysRevD.69.027504.

[58] H. et al. Lee.
Spiral resonators for on-chip laser frequency stabilization.
Nat. Commun. 4:2468 doi: 10.1038/ncomms3468, 2013.

[59] B. P. et al. Abbott.
Ligo: the laser interferometer gravitational-wave observatory.
Reports on Progress in Physics, 72(7):076901, 2009.

[60] S. A. Diddams et al.
An optical clock based on a single trapped 199hg+ ion.
Science, 293(5531):825–828, 2001.
DOI: 10.1126/science.1061171.

[61] Jan Friebe et al.
Absolute frequency measurement of the magnesium intercombination transition $^1s_0 \rightarrow {}^3p_1$.
Phys. Rev. A, 78:033830, Sep 2008.
DOI: 10.1103/PhysRevA.78.033830.

[62] T. M. Fortier, M. S. Kirchner, F. Quinlan, J. Taylor, J. C. Bergquist, T. Rosenband, N. Lemke, A. Ludlow, Y. Jiang, C. W. Oates, and S. A. Diddams.
Generation of ultrastable microwaves via optical frequency division.
Nature Photonics, 5:425–429, July 2011.
DOI: 10.1038/nphoton.2011.121.

[63] E. Hecht.
Optik.
Oldenbourg, 2005.

[64] George B Arfken, Hans J Weber, and Donald Spector.
Mathematical methods for physicists.
American Journal of Physics, 67(2):165–169, 1999.

[65] Wolfgang Demtröder.
Experimentalphysik 2: elektrizität und optik (springer-lehrbuch)(german edition).
Springer, 2013.

[66] Wolfgang Demtröder.
Laserspektroskopie, volume 4.
Springer, 2011.

[67] Warren Nagourney.
Quantum Electronics for Atomic Physics and Telecommunication.
Oxford University Press, 2014.

[68] Bernd Girod, Rudolf Rabenstein, and Alexander Stenger.
Einführung in die Systemtheorie, volume 4.
Teubner Stuttgart, 1997.

[69] John Bird.
Electrical circuit theory and technology.
Routledge, 2010.

[70] R. V. Pound.
Electronic frequency stabilization of microwave oscillators.
Review of Scientific Instruments, 17(11):490–505, November 1946.
DOI: doi:10.1063/1.1770414.

[71] R.W.P. Drever et al.
Laser phase and frequency stabilization using an optical resonator.
Applied Physics B, 31(2):97–105, 1983.
DOI: 10.1007/BF00702605.

[72] G. C. Bjorklund, M. D. Levenson, W. Lenth, and C. Ortiz.
Frequency modulation (FM) spectroscopy.
Applied Physics B, 32(3):145–152, November 1983.
DOI: 10.1007/BF00688820.

[73] Eric D. Black.
An introduction to pound–drever–hall laser frequency stabilization.
American Journal of Physics, 69(1):79–87, 2001.
DOI: http://dx.doi.org/10.1119/1.1286663.

[74] G.C. Bjorklund, M.D. Levenson, W. Lenth, and C. Ortiz.
Frequency modulation (fm) spectroscopy.
Applied Physics B, 32(3):145–152, 1983.
DOI: 10.1007/BF00688820.

[75] Michael Choma, Marinko Sarunic, Changhuei Yang, and Joseph Izatt.
Sensitivity advantage of swept source and fourier domain optical coherence tomography.
Opt. Express, 11(18):2183–2189, Sep 2003.
DOI: 10.1364/OE.11.002183.

[76] F Hoogeveen and T Ziegenhagen.
Production and detection of light bosons using optical resonators.
Nuclear Physics B, 358(1):3 – 26, 1991.
DOI: http://dx.doi.org/10.1016/0550-3213(91)90528-6.

[77] I. H. MALITSON.
Interspecimen comparison of the refractive index of fused silica.
J. Opt. Soc. Am., 55(10):1205–1208, Oct 1965.
DOI: 10.1364/JOSA.55.001205.

[78] Kazuharu Bamba et al.
Dark energy cosmology: the equivalent description via different theoretical models and cosmography tests.
Astrophysics and Space Science, 342(1):155–228, 2012.
DOI: 10.1007/s10509-012-1181-8.

[79] LASEROPTIK.
Ion Beam Sputtering for high quality mirrors.
Laseroptik GmbH / Horster Straße 20 / D-30826 Garbsen.

[80] P Kwee, C Bogan, K Danzmann, M Frede, H Kim, P King, J Pöld, O Puncken, RL Savage, F Seifert, et al.
Stabilized high-power laser system for the gravitational wave detector advanced ligo.
Optics express, 20(10):10617–10634, 2012.

[81] Ernst-Axel Knabbe.
Alps internal note, 2010.

[82] S Avino et al.
Low-noise adaptive optics for gravitational wave interferometers.
Classical and Quantum Gravity, 23(20):5919, 2006.

[83] Masahiro Toyoda, Kenichi Araki, and Yoshiaki Suzuki.
Measurement of the characteristics of a quadrant avalanche photodiode and its application to a laser tracking system.
Optical Engineering, 41(1):145–149, 2002.

[84] Euan Morrison, Brian J. Meers, David I. Robertson, and Henry Ward.
Experimental demonstration of an automatic alignment system for optical interferometers.
Appl. Opt., 33(22):5037–5040, Aug 1994.
DOI: 10.1364/AO.33.005037.

[85] John G Daly and Damien J Daly.
Structural adhesives for bonding optics to metals: a study of optomechanical stability.
In International Symposium on Optical Science and Technology, pages 177–184. International Society for Optics and Photonics, 2001.

[86] Tobias Meier, Benno Willke, and Karsten Danzmann.
Continuous-wave single-frequency 532 nm laser source emitting 130 w into the fundamental transversal mode.
Opt. Lett., 35(22):3742–3744, Nov 2010.
DOI: 10.1364/OL.35.003742.

[87] E. A. Donley, T. P. Heavner, F. Levi, M. O. Tataw, and S. R. Jefferts.
Double-pass acousto-optic modulator system.
Review of Scientific Instruments, 76(6):–, 2005.
DOI: http://dx.doi.org/10.1063/1.1930095.

[88] Reza Hodajerdi.
Aufbau einer zweidimensionalen magneto-optischen falle mit hohem fluss.
Master's thesis, Institut für Quantenoptik - Leibniz Universität Hannover, 2010.

[89] M. J. Holland and K. Burnett.
Interferometric detection of optical phase shifts at the heisenberg limit.
Phys. Rev. Lett., 71:1355–1358, Aug 1993.
DOI: 10.1103/PhysRevLett.71.1355.

[90] Robin Bähre.
PhD thesis, Gottfried Wilhelm Leibniz Universität Hannover, planed to be published in 2015.

[91] Katrin Dahl, G Heinzel, B Willke, KA Strain, S Goßler, and K Danzmann.
Suspension platform interferometer for the aei 10 m prototype: concept, design and optical layout.
Classical and Quantum Gravity, 29(9):095024, 2012.

[92] Claus Braxmaier, Gerhard Heinzel, et al.
Lisa pathfinder optical interferometry.

In Astronomical Telescopes and Instrumentation, pages 164–173. International Society for Optics and Photonics, 2004.

[93] Otto Lindig and Wolfgang Pannhorst.
Thermal expansion and length stability of zerodur in dependence on temperature and time.
Appl. Opt., 24(20):3330–3334, Oct 1985.
DOI: 10.1364/AO.24.003330.

[94] Robin Bähre Tobias Meier.
Alps internal document, 2010.

[95] F Steier et al.
Construction of the lisa back-side fibre link interferometer prototype.
Classical and Quantum Gravity, 26(17):175016, 2009.

[96] MUEPRO.
PHONOLYT Knopf.

[97] Maik Frede, Benno Willke, et al.
Fundamental mode, single-frequency laser amplifier for gravitational wave detectors.
Opt. Express, 15(2):459–465, Jan 2007.
DOI: 10.1364/OE.15.000459.

[98] I Zawischa, M Brendel, K Danzmann, C Fallnich, M Heurs, S Nagano, V Quetschke, H Welling, and B Willke.
The geo 600 laser system.
Classical and Quantum Gravity, 19(7):1775, 2002.

[99] K Dahl, A Bertolini, Born, et al.
Towards a suspension platform interferometer for the aei 10 m prototype interferometer.
In Journal of Physics: Conference Series, volume 228, page 012027. IOP Publishing, 2010.

[100] Joshua R Smith, LIGO Scientific Collaboration, et al.
The path to the enhanced and advanced ligo gravitational-wave detectors.
Classical and Quantum Gravity, 26(11):114013, 2009.

[101] Thomas J. Kane and Robert L. Byer.
Monolithic, unidirectional single-mode nd:yag ring laser.
Opt. Lett., 10(2):65–67, Feb 1985.
DOI: 10.1364/OL.10.000065.

[102] J.W. Czarske, R. Philipps, and I. Freitag.
Spectral properties of diode-pumped non-planar monolithic nd:yag ring lasers.
Applied Physics B, 61(3):243–248, 1995.
DOI: 10.1007/BF01082042.

[103] Gerhard Heinzel.
Liso program for linear simulation and optimization of analog electronic circuits.

[104] Jolien DE Creighton and Warren G Anderson.
Gravitational-Wave Physics and Astronomy: An Introduction to Theory, Experiment and Data Analysis.
John Wiley & Sons, 2012.

[105] Andreas Freise and Kenneth Strain.
" interferometer techniques for gravitational-wave detection.
Living Rev. Relativity, 13(1), 2010.

[106] Thorlabs Inc.
S121C Support Documentation.
http://www.thorlabs.de/thorcat/18300/S121C-SpecSheet.pdf.

[107] Guralp Systems Limited.
Weak motion broadband seismometer.
http://www.guralp.com/documents/DAS-030-0001.pdf.

[108] Patrick Kwee and Benno Willke.
Automatic laser beam characterization of monolithic nd:yag nonplanar ring lasers.
Appl. Opt., 47(32):6022–6032, Nov 2008.
DOI: 10.1364/AO.47.006022.

[109] Jan Hendrik Pold.
Design, Implementation and Characterization of the Advanced LIGO 200WLaser System.
PhD thesis, GottfriedWilhelm Leibniz Universität Hannover, 2014.

[110] Christopher L. Mueller.
Techniques for Resonant Optical Interferometry with Applications to the Advanced LIGO Gravitational Wave Detectors.
PhD thesis, University of Florida, 2014.

[111] e2v technologies.
CCD47-10 AIMO Back Illuminated Compact Pack High Performance CCD Sensor., 2006.

[112] Semrock.
1064 nm MaxLine® laser clean-up filter Part Number: LL01-1064-12.5.

[113] J.R. Lakowicz.
Principles of Fluorescence Spectroscopy.
Springer, 2007.

[114] Yuichi Kanaoka.

Organische fluoreszenzreagentien für die untersuchung von enzymen und proteinen.
Angewandte Chemie, 89(3):142–152, 1977.
DOI: 10.1002/ange.19770890305.

[115] International Union of Pure and Applied Chemistry.
IUPAC Gold Book.
IUPAC, 2006.

[116] G. G. Stokes.
On the change of refrangibility of light.
Philosophical Transactions of the Royal Society of London, 142:pp. 463–562, 1852.

[117] John B Skillman.
Quantum yield variation across the three pathways of photosynthesis: not yet out of the dark.
J Exp Bot, 59(7):1647–61, 2008.

[118] Nawid Zarrabi.
Hidden Markov Modelle für Einzelmoleküldaten.
PhD thesis, Universität Stuttgart, 2010.

[119] JAMES E. GILL.
Theory and interpretation of fluorescence and phosphorescence.
Photochemistry and Photobiology, 15(1):111–111, 1972.
DOI: 10.1111/j.1751-1097.1972.tb06230.x.

[120] Karl A. Franz, Wolfgang G. Kehr, Alfred Siggel, Jürgen Wieczoreck, and Waldemar Adam.
Luminescent Materials.
Wiley-VCH Verlag GmbH & Co. KGaA, 2000.

[121] D.A. Skoog, F.J. Holler, and S.R. Crouch.
Principles of Instrumental Analysis.
Thomson Brooks/Cole, 2007.

[122] A Luka, R Baghel, and V Chandra.
Decay of phosphorescence and delayed fluorescence of organic materials.
Recent Research in Science and Technology, 4(8), 2012.

[123] J.B. Pors.
Entangling Light in High Dimensions.
Casimir PhD series. 2011.

[124] Z. Y. Ou and L. Mandel.
Violation of bell's inequality and classical probability in a two-photon correlation experiment.
Phys. Rev. Lett., 61:50–53, Jul 1988.

DOI: 10.1103/PhysRevLett.61.50.

[125] S. K. Wong, G. Fournier, P. Mathieu, and P. Pace.
Beam divergence effects on nonlinear frequency mixing.
Journal of Applied Physics, 71(3):1091–1101, 1992.
DOI: http://dx.doi.org/10.1063/1.351272.

[126] L. J. Wang, X. Y. Zou, and L. Mandel.
Induced coherence without induced emission.
Phys. Rev. A, 44:4614–4622, Oct 1991.
DOI: 10.1103/PhysRevA.44.4614.

[127] T. P. Grayson and G. A. Barbosa.
Spatial properties of spontaneous parametric down-conversion and their effect on induced coherence without induced emission.
Phys. Rev. A, 49:2948–2961, Apr 1994.
DOI: 10.1103/PhysRevA.49.2948.

[128] Amir Nevet et al.
Plasmonic nanoantennas for broad-band enhancement of two-photon emission from semiconductors.
Nano Letters, 10(5):1848–1852, 2010.
DOI: 10.1021/nl1005806.

[129] SBIG ASTRONOMICAL INSTRUMENTS.
Operating Manual ST-402.
https://www.sbig.com/.

[130] Truesense Imaging Inc.
KAF-0402 IMAGE SENSOR.
http://www.onsemi.com/pub/Collateral/KAF-0402-D.PDF.

[131] Truesense Imaging Inc.
KAF-3200 IMAGE SENSOR.
http://www.onsemi.com/pub/Collateral/KAF-3200-D.PDF.

[132] Truesense Imaging Inc.
KAF-1001 IMAGE SENSOR.
http://www.onsemi.com/pub/Collateral/KAF-1001-D.PDF.

[133] Truesense Imaging Inc.
CCD image sensors for digital photography.
http://www.onsemi.com/PowerSolutions/parametrics.do?id=101682.

[134] Coherent Inc.
Operator's Manual Verdi Diode-Pumped Laser.
5100 Patrick Henry Drive Santa Clara, CA 95054.

List of Figures

List of Tables

ACKNOWLEDGMENTS

At this point, I want to thank all the people, without whose support I would never be successful with my thesis.

First of all I would like to express my deep gratitude towards Axel Lindner and Benno Willke for allowing me to participate in the ALPS group, as well as for their mentoring and invaluable scientific support during the last four years. Their door was always open for me to come with any kind of problem. I want to thank also Andreas Ringwald and Dieter Horns who make the ALPS collaboration possible, for their constant support to all the PhD students in the group.

I am very grateful to Ernst-Axel Knabbe for his support from my first day at DESY until now. I learned a lot from him, not only about physics but also about life. I am sincerely thankful to Jan Hendrik Põld and Babette Döbrich. Babette's support in the lab during my time was indispensable. Although Jan was a member of ALPS only during the last six months, his support was essential for the final measurements and the proofreading of my thesis. I would also like to thank the other members of the first generation of ALPS PhD students: Robin Bähre, Jan Dreyling-Eschweiler and Jan Eike von Seggern for their support and scientific cooperation. Especially to Jan Dreyling-Eschweiler, I am grateful for his additional support during my stay in Hamburg and also during my knee surgery. I also want to thank the new generation of ALPS PhD students Noëmie Bastidon, Natali Kuzkova and Christoph Weinsheimer for their support and wish them all success in the ALPS experiment.

My time in Hamburg could not be as wonderful as it was without the kind friends from DESY that I made during the past years. I want to thank all my friends from Hamburg and my old friends from Hanover for all the beautiful moments in my life. Without them I wouldn't be where I am now.

Special thanks go to my good friend Timko Dubielzig. Without his proofreading not a single sentence in this thesis would be grammatically correct. In addition, his mental support and friendship during difficult times of my studies leave me indebted to him.

Last but not least, I thank my brothers for being there and for their love which is priceless to me. Just like for my diploma thesis and every other achievement in my life, the deepest and warmest acknowledgment belongs to my mother. She never lost her faith in me and gave me always the needed love and necessary support.